Dynamic fracture in brittle amorphous materials : Dissipation mechanisms and dynamically-induced microcracking in PMMA

Claudia Maribel Guerra Amaro

Claudia Maribel Guerra Amaro. Dynamic fracture in brittle amorphous materials : Dissipation mechanisms and dynamically-induced microcracking in PMMA. Physique [physics]. Ecole Polytechnique X, 2009. Français. NNT : . pastel-00006135

HAL Id: pastel-00006135
https://pastel.hal.science/pastel-00006135

Submitted on 20 Jul 2010

Ecole Polytechnique - Palaiseau

Dynamic fracture in brittle amorphous materials : Dissipation mechanisms and dynamically-induced microcracking in PMMA

THÈSE

présentée et soutenue publiquement le 9 Décembre 2009

pour l'obtention du

Doctorat de l'Ecole Polytechnique

(spécialité physique)

par

Claudia Maribel Guerra Amaro

devant la commission d'examen

Examinateurs :	Moisés Hinojosa Rivera Krishnaswamy Ravi-Chandar Michel Rosso
Rapporteurs :	Mokkhtar Adda-Bedia Sergio Ciliberto
Directeur de thèse :	Davy Dalmas Daniel Bonamy

Service de Physique et Chimie des Surfaces et Interfaces — CEA Saclay

Agradecimientos

La oportunidad de realizar mi tesis doctoral fuera de México ha sido una de las mejores experiencias en mi vida. Durante estos tres años, he aprendido muchas cosas tanto en el ámbito profesional como en mi vida personal. Estos aprendizajes los he adquirido gracias al apoyo y consejos de muchos amigos, los cuales compartieron conmigo algunos momentos durante mis estudios de doctorado. Primeramente, me gustaría agradecer a mis dos jefes Daniel y Davy, con quienes ha sido un gran honor trabajar. Mil gracias, “chefs” por todo su apoyo, por compartir conmigo sus conocimientos y toda su paciencia, las discusiones científicas, consejos y regaños. Gracias por siempre exigirme dar lo mejor de mi misma, un aprendizaje que se quedará conmigo durante toda mi vida. Muchas gracias a mi gran maestro y mentor Moisés, quien me ha impulsado durante toda mi carrera. Sin su apoyo, consejos, aprendizaje y amistad, esta tesis doctoral no se hubiera podido realizar. Mil gracias a Frédéric, quien estuvo a mi lado durante el último año de mi tesis, y que con su amor, consejos, paciencia, discusiones y regaños, me dio la energía y motivación en los momentos más difíciles de la tesis… gracias, amor, por todos estos momentos y los que vienen también. Gracias a todas las demás personas que son o fueron parte del “Groupe de Systèmes Complexes & Fracture”, Elisabeth mi mamá científica, Cindy mi hermana, Gaël, Cédric, Tatiana, Laurent y los dos postdocs Fabrice y Julien quienes fueron mis maestros, me apoyaron con todos los experimentos, la interpretación de resultados, la escritura de artículos, resúmenes, presentaciones y consejos. Mil gracias por todos estos momentos y por brindarme su amistad.

Quiero también agradecer a toda la gente que forma parte del Service de Physique et Chimie de Surfaces et Interfaces, a mi hermosa Catherine, quien me apoyó con todos los trámites administrativos, se preocupó siempre por saber cómo estaba y fue con quien pasé mucho tiempo discutiendo a cerca de mis proyectos. Mil gracias, Catherine. Quiero agradecer a todos los tesistas y equipo de trabajo del SPSCI, Odile, Amandine, Stephane, Ludovic, Sylvan, Parwana, Cyril, Jérôme, Cristophe, François, J. B, Fabien, Carol, Nripan, Vadym y Camille, con quienes compartí comidas, fiestas, el cafecito en donde discutíamos de ciencia, política y chismes, y ¡cómo olvidar el miércoles de discusión científica en el bar d’Orsay! Mil gracias por todos esos momentos que siempre ocuparán un lugar muy especial en mi corazón. Un agradecimiento muy especial a los jefes del SPSCI Serge y Luc, quienes siempre me brindaron su apoyo y estuvieron muy al pendiente de mi tesis. Mil gracias a los químicos Pascal y Mathieu, quienes siempre me apoyaron con mis experimentos. Gran parte de los resultados es gracias a ustedes y su excelente trabajo. Gracias al equipo de Jaques, por darse el tiempo de orientarme con toda la parte electrónica. Quiero agradecer también a Christophe de la DEN quien nos ayudó con la calibración del captor de fuerza. Mil gracias a Alexis y Georges de l’ENS por prestarme el perfilómetro óptico y apoyarme con todo lo que necesité durante mi estancia en su laboratorio.

Una tesis no se hace sólo con trabajo científico, sino también emocional. Mil gracias a Maya, “ma petite”, quien comparte conmigo todos los momentos de mi vida. Gracias a Nebo, Claire, Vladimir, Bianca, Greethel (alias la jarocha) y Alfredo, que son todos grandes amigos que viven o vieron un tiempo en Francia. Mil gracias a Irma, mi mejor amiga quien es casi como mi hermana, por estar conmigo gran parte de mi tesis a pesar de que viviera en Alemania. Gracias, preciosa, por estar siempre conmigo apoyándome, escuchándome, aconsejándome… ¡y de fiesta, fiesta! Mil gracias a la familia Lechenault: Catherine, Jean, Julien, Christophe, Peggy, mammy

Colette, mammy Nellyy, pappy Jean-Baptiste quienes compartieron conmigo las costumbres en Francia, me mostraron lugares, comidas y vinos increíbles. Gracias por estar al pendiente de mi tesis y compartir conmigo esos grandes momentos tan especiales que siempre estarán en mi corazón.

Mil gracias a mi madre hermosa quien es mi ejemplo a seguir y quien me da toda la inspiración y apoyo para que pueda realizar todos los proyectos de mi vida. Ella es quien me dio la vida y quien continúa siendo el combustible que le da energía a mi ser para seguir adelante… ¡mil gracias, "mum"! Mil gracias a mi papá José Luis por siempre apoyarme, estar orgulloso de mí, ayudarme a seguir avanzando y ser el brazo derecho de mi madre en todos los momentos de nuestras vidas. El estar fuera de casa, el tener la tenacidad para seguir adelante, caer y seguir avanzando a pesar de los obstáculos que se presentan siempre en la vida, es un trabajo en equipo. Gracias a mi familia, especialmente a mis "mamás": mi abuelita (mi "bolish"), mis tías Adriana, Idalia y Elsa, quienes siempre me apoyaron de manera incondicional. Aún y cuando nos separaban 10,000 km., su presencia siempre estuvo conmigo. Gracias a mis niños por quienes siempre he tratado dar lo mejor de mí José Luis (mi gordo), Fanny, Dante, Vale, Mariana, Emilio, Walter. Gracias a la gran familia BW por todo el apoyo y motivación que me mostraron durante la escritura de la tesis, mil gracias Mat, Fanch, Julie, Ju, Céline, Sara, Emilie, Benjamin, Natasha, Manel, Sb, Jo, Vlad. Mil gracias a todos mis amigos que desde mi tierra natal Monterrey, Nuevo León, México, siguieron mis pasos, festejaron logros conmigo y me alentaron a seguir adelante cuando las cosas no eran como lo esperaba. Mil gracias Laura, Denise, Idalia, Sara, Elvira, José Luis, Lucy, Mike, Oswaldo, Chiapas, Panch, Julian, Marco, Nogales.

Un agradecimiento muy especial a la Universidad Autónoma de Nuevo León, institución donde realicé mis estudios de prepa, licenciatura y maestría. Gracias, Dr. Ortiz e Ing. Báez por el apoyo incondicional que tuve por parte de mi casa de estudios. Mil gracias a Lupita Mejía y Lupita Martínez, quienes me apoyaron con todos los trámites administrativos. Chicas, aunque estuvieron a 10,000 km resolvieron todos los problemas como si estuvieran aquí, mil gracias.

Mil gracias a Edgar, con quien compartí conocimientos, discusiones científicas y proyectos. Gracias a Fabrice y Audray de l'Ecole Doctorale Polytechnique por el gran apoyo y consejos para todos los trámites administrativos durante mi tesis doctoral.

Un agradecimiento muy especial a todos los miembros de mi jurado de tesis Dr. Moisés Hinojosa Rivera, Dr. Krishnaswamy Ravi-Chandar, Dr. Michel Rosso, Dr. Mokkhtar Adda-Bedia y Dr. Sergio Ciliberto por leer el manuscrito, por hacerme correcciones y sobre todo reservar un lugar en sus apretadas agendas de trabajo para estar el día de la defensa de tesis. Gracias por compartir conmigo sus conocimientos, ellos me han dejado a un gran aprendizaje.

Contents

Introduction

Why things break? Understanding and modeling the mechanisms that result in material failure is of technological importance. The answer to these questions has then been the motivation of many groups of research. Since the pioneering work of Griffith, crack propagation has been shown to be basic mechanism responsible for material failure. Over the last century and since the pioneering work of Mott, a coherent theoretical framework, the so-called Linear Elastic Fracture Mechanics has developed and, within elastodynamics continuum theory, it provides a quantitative description of the motion of a crack front in linear elastic material. This framework describes fairly well experimental observations at low velocities. However, some questions remain to be answered at high velocities: First, it is predicted that the maximum velocity at which a crack can propagate is the so called Rayleigh wave velocity, c_R, while experimental observations report a maximum crack velocity in brittle disordered materials ranging between $0.6 - 0.7 \times c_R$. Second, the theory predicts smooth crack paths at continuum scales, in apparent contradiction with fractography experiments that report rough fracture surfaces at high velocities.

To shed light on these apparent discrepancies has been the focus of my PhD work. We have designed an experimental setup that has allowed us to probe the dissipation expand mechanisms and the dynamics of crack propagation in a model brittle amorphous material, PMMA, over a wide range of velocities, at both macroscopic and microscopic scale.

This manuscript is divided into 4 chapters: In chapter 1, we start with an examination of the theories derived from continuum elastodynamics to describe the conditions for crack propagation and the selection of crack velocity in a perfectly brittle material. We then review briefly the experiments performed in dynamic fracture over the last decades to examine the limits/applicability of these theories and underline the open questions.

Chapter 2 is devoted to the presentation of our experimental setup. We choose to make crack propagate in PMMA through a so-called wedge splitting geometry. This geometry has allowed us to generate stable dynamic crack propagation over a wide range of velocities. Instantaneous crack velocity was measured through a method inspired from the potential drop method, and the stress field at the tip of the propagating crack was estimated through a combination of finite element computations.

The fracture energy, i.e. the energy dissipated as the crack front propagated over a unit surface was then measured experimentally in PMMA for various conditions using this experimental set-up. The analysis of this quantity is provided in chapter 3. Its evolution as a function of the crack velocity exhibits an abrupt 3-fold increase at a well-defined critical velocity of $v_a \simeq 0.19 \times c_R$. This critical velocity is much smaller than the critical velocities reported in the literature at higher values (about $0.4 \times c_R$) that correspond to the onset of micro-branching instabilities, i.e. the onset beyond which the crack front splits into a multi-crack state. Fractography analysis reveals that this critical velocity v_a corresponds also to the appearance of conic marks on the fracture surfaces. These conics marks are the signature of damage spreading through microcracks nucleating ahead of the propagating crack front.

The dynamics of damage spreading is then studied at the microscopic scale in chapter 4. In particular, it is shown how one can reconstruct the dynamics of main crack propagation, microcrack nucleation and microcrack growth, from the conic marks observed on the fracture surfaces. These reconstructions are used to analyse the statistics of microcracking events and to relate both the process zone and the macroscopic velocity to the microcrack dynamics.

Chapter 1

An overview about fracture theories, experiments and analyses.

1.1 Onset of fracture: Linear elastic fracture mechanics theory

What is fracture? The simplest answer would be "the process of breaking" or "the condition of being broken". Another way to define fracture is a response of a body to a stress (or strain) applied externally or generated internally by differential changes within the solid caused by temperature gradients, shrinkage, and/or chemical changes. The fracture process involves the nucleation and propagation of a crack. The distinction between nucleation and propagation is not always clear. Often, large cracks result from the coalescence of multiple small cracks. In this chapter, we will not focus on nucleation, but only on the existing criteria that predict when, and at which velocity, a single crack propagates.

In order to understand why things break, we begin this chapter with an exploration of the models proposed in the fracture mechanics field. This field is concerned with the quantitative description of the mechanical state of a deformable body containing a crack. More specifically this field concentrates on characterizing and measuring the resistance of materials to crack growth. Mathematical models are frequently used to describe mechanical states of a particular system. These models are typically built on an idealized description of: (i) the geometrical configuration of the deformable body;

(ii) an empirical relationship between internal stress and deformation; and (iii) the relevant balance laws of physics dealing with mechanical quantities.

The field of fracture mechanics was initiated by Kolosov with his the 1909 PhD thesis [1]. He created basic mathematical tools which he in turn used in the study of the growth of preexisting macroscopic cracks. Some years later, in 1913, Inglis [2], also solved a basic crack problem. Following Inglis' publication, Hopkinson suggested that the nonlinear phenomena near the crack tip should be taken into account. This was indirectly done by Griffith [3, 4] in 1920, through energy considerations and the use of the concept of surface energy, γ_s. His experiments with thin glass rods prompted Weibull [5] to establish a statistical theory of fracture. In 1952, Orowan [6] extended the Griffith's approach to all cases of small scale yielding (in which plastic flow is confined to small region near the crack edge) by inclusion of all dissipative energy, essentially surface energy and plastic work. Then in 1957, new concepts were introduced by Irwin [1, 7]: (i) the stress intensity factor K and (ii) the energy release rate G. In the following subsection these successive developments are explained in more detail.

1.1.1 LEFM: the evolution of fracture mechanics by Inglis's, Griffith's and Irwing's ideas

In an ideal linear elastic material, the relations between the stress components, σ_{ij}, and the strain components, ϵ_{ij}, are given by *Hooke's law*. In the first approximation, the material can be sketched as a network of spring of length a (inter-atomic bond) and stiffness E (Young modulus). Let us now apply a normal stress, σ, uniformly distributed over two opposite sides, as shown in Fig. 1.1. An elongation of the distance between atoms δa, which are normally separated by a can be expressed as follows:

$$\frac{\delta a}{a} = \epsilon = \frac{\sigma}{E} \tag{1.1}$$

where ϵ is the normal tensile strain. Now, suppose that a bond is broken when two connected atoms move apart by $\epsilon_c = 20\%$ (for more details see [8]), i.e. for a elongation $\delta a_c = \frac{a}{5}$. Then, the failure of the material is obtained for the critical stress $\sigma_c = \frac{E}{5}$. This value is orders of magnitude larger than typical strengths, σ_c, measured

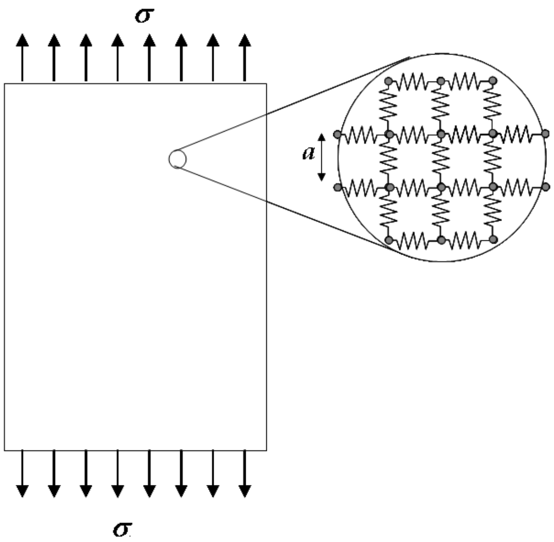

Figure 1.1: An ideal solid submitted to external normal stress,σ, uniformly distributed. This solid is built of inter-atomic bonds described by springs of stiffness, E, and length, a.

experimentally (typical values range between $0.0001E$ and $0.01E$). The difference is accounted for by defects which are not present in this simple model.

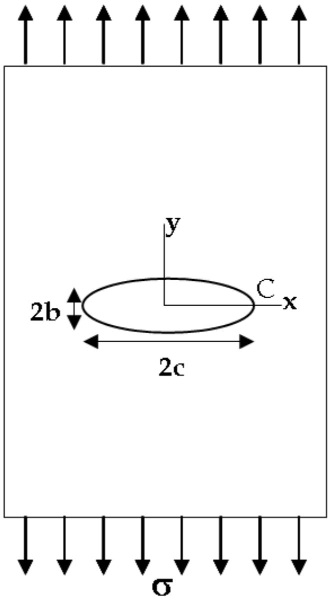

Figure 1.2: Plate containing an elliptical defect of semi-axes b and c, subjected a uniform applied tension σ

Let us then introduce an elliptical defect of semi-axes b and c inside the loaded solid, as is represented in Fig. 1.2. The first to perform this analysis was Inglis [2] in 1913. Several assumptions are made in Inglis analysis: (i) Hooke's law holds everywhere in the plate; (ii) the boundary of the hole is stress free; and (iii) b and c are small in comparison with the plate dimensions. Hence one can demonstrate that the maximum tensile stress acts at the point C where the curvature $\rho_C = \frac{b^2}{c}$ has the minimal value. This stress is given by:

$$\sigma_C = \sigma(1 + 2\left(\frac{c}{b}\right)^{1/2}) \tag{1.2}$$

when $b \ll c$, ρ_C is very small, Eq. 1.2 can be approximated by:

$$\frac{\sigma_C}{\sigma} \simeq 2\left(\frac{c}{\rho_C}\right)^{1/2} \tag{1.3}$$

Inglis's solution illustrates stress concentration at the tip of defects. The stress-concentration can take values orders of magnitude larger than unity for micrometer-size defects with ρ_C set by the inter-atomic spacing. One can also note that the stress concentration depends on the shape of the hole rather than on the size [9, 10].

Predicting whether or not a specimen will break boils down to predicting whether pre-existing defects or micro-cracks will propagate or not. Griffith proposed, in 1920, to define this onset through a thermodynamic balance [3, 4]. Let us consider an elastic body containing a plane-crack of length c subjected to a load applied at the outer boundary (e.g. the situation depicted in figure 1.2 with $b \to 0$). The total energy $U(c)$ of the system can be expressed as the sum of two terms:

$$U = U_M + U_S \tag{1.4}$$

where U_M denotes the mechanical energy stored in the system and U_S is the energy stored in the free surface of the crack. Let us see how U_S, U_M and U are modified when the crack length is slightly increased: $c \to c + dc$. The energy component stored in the crack surfaces, U_S, is directly proportional to the crack length, c, and hence increases. Calling γ_s the surface energy of the material, (i.e. the energy needed to create a surface of unit area), one gets:

$$\frac{dU_S}{dc} = 2\gamma_s \tag{1.5}$$

On the other hand, the mechanical energy U_M stored in the specimen decreases as c increases. One then usually defines the *mechanical energy release rate*, G, as:

$$G = -\frac{dU_M}{dc} \tag{1.6}$$

Then, depending on the values of G and γ_s, two cases can then be distinguished:

- If $G < 2\gamma_s$, U increases as c increases. Hence, the crack then remains stable.
- If $G > 2\gamma_s$, U decreases as c increases. The crack then propagates and yields structural failure.

The so-called Griffith's criterion for fracture onset is then:

$$G \geq 2\gamma_s \tag{1.7}$$

Note that in this thermodynamic balance, energy dissipation resides only in the creation of two additional surfaces as the crack extends. In real materials, other sources of dissipation are likely to occur, e.g. plastic deformation [11], microcracking [12], temperature elevation, among others. In this respect, it was proposed, first by Irwin [7], to replace $2\gamma_s$ by an effective term Γ, called *fracture energy*. Γ encodes all the damage and dissipative processes occurring at the crack tip as the crack progresses over a unit length. The Griffith's criterion for fracture onset can then be recast as:

$$G \geq \Gamma \tag{1.8}$$

1.1.2 Stress field at cracks tip

The application of Griffith's criterion requires the computation and comparison of two quantities: (i) the fracture energy, Γ, and (ii) the mechanical energy release rate, G. On the one hand, what sets the value of Γ in a given material remains far from being understood. However Γ is known to depend crucially on the complex damage and the dissipative processes occurring within a small zone at the crack tip. This zone is frequently referred to as the *fracture process* zone, and it is defined as the region where the material stops behaving as a linear elastic material. There is no firm basic principle allowing the prediction of its size from chemical and microstructural composition. To better understand how its value changes as the crack velocity increases constitutes one of the main goals of this PhD. On the other hand, the second term is given by the stress, strain and displacement fields outside the process zone and can be computed using finite element methods.

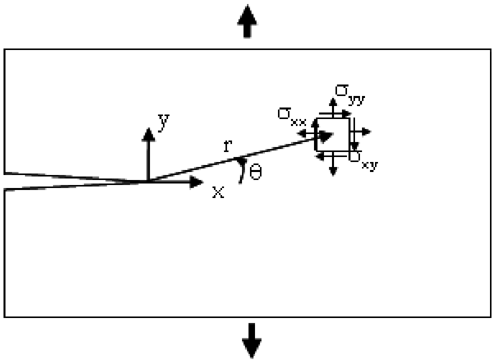

Figure 1.3: Co-ordinate system around crack tip. r and θ are the polar coordinates. Stresses σ_{xx}, σ_{yy} and σ_{xy} act on the faces of the square element.

Consider an infinite plate containing a crack normal to the applied load as is shown in Fig. 1.3. Using this co-ordinate system the stresses close to the crack tip can be written as [7, 6]:

$$\sigma_{ij} \simeq \frac{K(c)}{\sqrt{2\pi r}} f_{ij}(\theta) \tag{1.9}$$

where the functions $f_{ij}(\theta)$ are universal and given by:

$$\begin{aligned} f_{xx}(\theta) &= \cos(\frac{\theta}{2}) \left[1 - \sin(\frac{\theta}{2}) \sin(3\frac{\theta}{2})\right] \\ f_{xy}(\theta) &= \cos(\frac{\theta}{2}) \left[1 + \sin(\frac{\theta}{2}) \cos(3\frac{\theta}{2})\right] \\ f_{yy}(\theta) &= \sin(\frac{\theta}{2}) \cos(\frac{\theta}{2}) \cos(3\frac{\theta}{2}) \end{aligned} \tag{1.10}$$

As pointed out by Irwin [9, 7], the knowledge of the prefactor $K(c)$ in Eq. 1.9 characterizes entirely the stress field in the vicinity of the crack tip. This parameter, called *stress intensity factor*, depends on both the applied load and the specimen geometry. In the case of a sharp elastic crack of length $2c$ embedded in an infinitely wide plate considered by Griffith, $K = \sigma\sqrt{\pi c}$. More generally, K can be expressed as $K = \sigma\sqrt{\pi c} f(\text{geometry})$, where the dimensionless function f can be determined through finite element computations, as in the present work (for more details see section 2.4).

From the crack tip stress field, one can deduce the mechanical energy release rate, G, that intervenes in the Griffith's criterion (Eq. 1.8). This last one is given by:

$$G = \frac{K^2}{E'} \quad \text{plane stress} \tag{1.11}$$

$$G = \frac{K^2}{E'}(1-\nu^2) \quad \text{plane strain} \tag{1.12}$$

1.1.3 Plane stress, plane strain

It should be emphasized that, all the calculations presented up to now are for two-dimensional systems, while realistic structures are three-dimensional. Nevertheless, many situations can be approximated by an equivalent two-dimensional state of stress. The reduction of dimensions can be considered in two cases, (At this point, it is important to set the co-ordinate system. In all the following, x refers to the direction of crack growth, y to the direction of tensile loading, and z to the direction parallel to the crack front) as described below:

- Plane stress: A thin plate is loaded by forces remaining within the plane of the plate and distributed uniformly over the thickness. The stress components associated with the z-direction are zero on both faces of the plate and are assumed to be zero within the plate. As a result, the stress components are functions of x and y, only.

- Plane strain: A thick plate is loaded by forces remaining within the plane of the plate and distributed uniformly over the thickness. The stress in the z direction can be deduced from the stress components in x and y directions. Hence, the plane strain reduces to the determination of stresses in the x and y direction [13].

Subsequent chapters of this thesis will assume plane stress conditions (see. e.g. section 2.4).

1.1.4 Various failure modes

Equation 1.9 gives the stress field near the crack tip when loaded in tension (see fig.1.3). However, it can be generalized to any loading conditions. In this respect, it is useful to distinguish three basic modes of crack loading:

- Mode I: *Opening or tensile mode* which corresponds to normal separation of the crack walls under the action of tensile stress (Fig 1.4 a).
- Mode II: *Sliding mode* which corresponds to longitudinal shearing of the crack walls in a direction normal to the crack front (Fig 1.4 b).
- Mode III: *Tearing mode* which corresponds to lateral shearing parallel to the crack front(Fig 1.4 c).

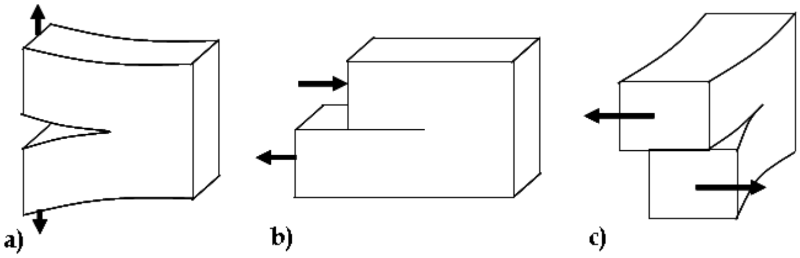

Figure 1.4: Modes of fracture: a) opening, b) sliding and c) tearing.

To each of these three modes, one can associate a stress intensity factor K_I, K_{II} and K_{III}. Mode I, is by far the most relevant to crack propagation in isotropic solids. Brittle cracks have a tendency to seek out an orientation which minimizes the shear/tear loading (see section 1.2.3).

1.2 Dynamically growing cracks: Elastodynamic continuum theory

All fracture surfaces are generated by cracks, that can move extremely fast (over 1000 m/s), or slowly (less than 1 mm/year). The majority of cracks grow rapidly, their velocity or speed is dependent on the loading conditions and material properties. Dynamic processes in a cracked body fall into two basic categories: dynamic crack propagation and dynamic loading of bodies with stationary cracks. Often a mixture of these two kinds of processes appears. For instance when dynamic loading on a body containing a stationary crack causes dynamic crack propagation (or when dynamic crack propagation generates waves) which, after reflection at an outer boundary of the body, impinge on the crack.

In order to understand how cracks grow dynamically let's have a brief exploration of the theories proposed in the elastodynamics continuum. A general approach to the dynamic fracture problem was outlined by Mott [10]. His work consists basically in incorporating an inertial term known as kinetic energy, U_K, into the total system energy (see eq. 1.4) for a straight crack. Following the analyses presented by Mott; Dulaney and Brace [14] slightly improved Mott's work. This improvement consisted in a dimensional analysis clarifying basic physical processes (despite being wrong in many details) and consists of writing down an energy balance equation for crack propagation [15]. From the analysis above decribed, it is not possible to deduce the maximum crack tip velocity. Theoretical treatments by Yoffe [16], Broberg [17] and Craggs [18] showed that the nature of the field near the tip of a propagating crack changes with velocity, and Schardin [19] demonstrated that cracks tends to accelerate to a maximum velocity. In this context Stroh [20] correctly argued that the maximum velocity should be the Rayleigh wave speed, the speed at which sound waves travel over a free surface. But then, in the 1970's some doubts arouse about the uniqueness for each instantaneous crack velocity of the singular terms, even if this velocity is (continuously) varying. Detailed investigations performed by Freund and Clifton [21], Nilsson [22], and Achenbach and Bazant [23] confirmed the uniqueness. Later work, explicitly showed how the angular distributions of nonsingular terms are not unique. They depend not only on the instantaneous crack velocity, but also on the crack edge acceleration demonstrated by Rosakis [24, 25].

Now after the brief introduction about some of the theories proposed in elastodynamics, we will focus on the expressions that are used to deduce the dynamic properties in our experiments.

1.2.1 Stress field singularity for a propagating crack

We now focus on the elastodynamic equations used to interpret our experimental data. As for the situations with static cracks presented in section 1.1.3, the stress field, σ_{ij}, is singular in the vicinity of a moving crack tip and can be written as:

$$\sigma_{ij} \simeq \frac{K_d(c,v)}{\sqrt{2\pi r}} f_{ij}(\theta,v) \tag{1.13}$$

where c is the crack length, v is the crack velocity, $K_d(c,v)$ is the *dynamic stress intensity factor*, and $f_{ij}(\theta,v)$ are universal functions given by:

$$\begin{align}
f_{xx}(\theta,v) &= \frac{1}{R}\left((1+\alpha_s^2)(1+2\alpha_d^2-\alpha_s^2)\frac{\cos\theta_d/2}{\sqrt{\gamma_d}} - 4\alpha_s\alpha_d\frac{\cos\theta_s/2}{\sqrt{\gamma_s}}\right) \notag\\
f_{xy}(\theta,v) &= \frac{2\alpha_d(1+\alpha_s^2)}{R}\left(\frac{sin\frac{1}{2}\theta_d}{\sqrt{\gamma_d}} - \frac{sin\frac{1}{2}\theta_s}{\sqrt{\gamma_s}}\right) \tag{1.14}\\
f_{yy}(\theta,v) &= -\frac{1}{R}\left((1+\alpha_s^2)^2\frac{\cos\theta_d/2}{\sqrt{\gamma_d}} - 4\alpha_s\alpha_d\frac{\cos\theta_s/2}{\sqrt{\gamma_s}}\right) \notag\\
& \tag{1.15}
\end{align}$$

where the parameters α_s, α_d, θ_s, θ_d, γ_s, and γ_d are related to v, θ, the transverse waves speed (c_s) and the dilatational wave speed (c_d) through:

$$\alpha_s = \sqrt{1-(v/c_s)^2}, \quad \alpha_d = \sqrt{1-(v/c_d)^2}, \quad R = 4\alpha_s\alpha_d - (1+\alpha_s^2)^2, \tag{1.16}$$

$$\tan\theta_d = \alpha_d\tan\theta, \quad \tan\theta_s = \alpha_s\tan\theta, \tag{1.17}$$

$$\gamma_d = \sqrt{1-(v\sin\theta/c_d)^2}, \quad \gamma_s = \sqrt{1-(v\sin\theta/c_s)^2} \tag{1.18}$$

R refers to the Rayleigh function:

$$R = 4\alpha_s\alpha_d - (1+\alpha_s^2)^2 \tag{1.19}$$

It is worth to mention at this point that the Rayleigh speed, c_R, is defined as the first root of this function. This velocity sets then the limiting speed for crack propagation since R vanishes for $v \rightarrow c_R$ and hence, $\sigma_{ij} \rightarrow \infty$ for $v \rightarrow c_R$.

It is also interesting to note that the dynamic stress intensity factor, $K_d(c, v)$, is related to the static effective one $K(c)$ computed for the same crack length c, in the same geometry, and with the same loading condition, but for an immobile crack $(v = 0)$. The relation is as follows

$$K_d(c, v) = k(v)K(c) \quad \text{with} \quad k(v) \simeq \frac{1 - v/c_R}{\sqrt{1 - v/c_d}} \tag{1.20}$$

where $k(v)$ is the function of crack speed, and it depends on the material properties through the elastic waves speed. However it is independent of the loading conditions of the specimen. This will be used after in this PhD to estimate the dynamic stress intensity factor for the quasi-static finite element analysis.

1.2.2 Equation of motion

The form taken by the stress field at the crack tip (Eq. 1.13) allows us to evaluate the mechanical energy flux at the crack tip. Under small scale yielding conditions (i.e. all of the complex non-linear processes are embodied in a small zone at the crack tip), one can assume that the equation of motion is given by balancing this energy flux with the fracture energy, Γ [26, 21, 27], this yields:

$$A(v)\frac{K_d(c, v)^2}{E} = \Gamma \quad \text{with} \quad A(v) = \frac{v^2 \alpha_D}{(1 - \nu)c_S^2 R} \tag{1.21}$$

The function $A(v)$ is a universal function, in the sense that it does not depend on the details of the applied loading or the configuration of the specimen. In this work, calculations of Γ are made by computing $K(c)$ for quasi-static conditions via finite element analysis. Recasting this equation of motion and making use of equation 1.20, this yields [21, 28]:

$$\Gamma = \left(1 - \frac{v}{c_R}\right)\frac{K^2(c)}{E} \tag{1.22}$$

1.2.3 Path equation

Finally, to complete the continuum theory of crack growth, one has to add a path criterion. This is provided by the Principle of Local Symmetry (PLS) of Goldstein and Salganik [29] which states that a moving crack progresses along a direction so as to remain in pure tension. In 2D systems, the crack is loaded by a combination of mode I and II only, and PLS implies that the direction of crack propagation is chosen so that $K_{II} = 0$. In 3D systems, the crack loading can also contain a mode III component. In order to cancel K_{III} and to propagate in pure mode I, the crack front would need to twist abruptly around the direction of propagation, which would yield unphysical discontinuities in the crack path. In this situation, the front is commonly observed to split into many pieces and to form ”lances” [30].

1.2.4 Predictions

There are two separate lines of inquiry pulling people into dynamic fracture of brittle materials. Both correspond to current puzzles about dynamic fracture:

- The first line is about the dynamics of cracks. Equation 1.13 predicts that a crack maximum velocity in elastic media it is the Rayleigh wave speed, c_R.
- The second line concerns the roughness of post-mortem fracture surfaces. The principle of local symmetry, described above predicts smooth surfaces at continuum scales, *i.e.* at scales over which the mechanical properties of the considered brittle material are homogeneous.

1.3 Experiments in dynamic fracture

Many important experimental researches on dynamic fracture of brittle materials were carried out in parallel with the development of the dynamic fracture mechanics concepts presented in the preceding section. These experiments were often done on glasses or other model brittle materials. These experiments providing qualitative observations and quantitative data have been vital importance on the development of dynamic fracture mechanics. Indeed, a number of crucial observations on the behavior of growing cracks in glass were made in the 1940’s and 1950’s. Despite the time delay, these observations are only partially understood and described from a theoretical point of view.

In addition to the importance of the experimental research, the significance of the experimental techniques developed all along should be recognized. One such leap was the development of the full-field optical methods, observation and special techniques of high speed photography. These developments have helped researchers greatly in the understandings of crack front dynamics.

Historically, much attention has focused on the maximum attainable crack velocity. The theoretical analysis presented in the previous section suggests that this velocity should coincide with the Rayleigh wave speed, c_R, for mode I cracks. However, experimental results point stubbornly to substantially lower velocities, at most $0.6 - 0.7 \times c_R$ [31, 1, 15, 32, 28]. It was also proposed that this maximum velocity (made dimensionless by dividing by c_R) might not be a material property [33, 34]. A divergence of energy flux flowing into the process region predicted as the crack velocity approaches the limit has been observed. Some researchers have observed an energy flux up to 50 times larger than that observed at slow crack velocity [35]. However, experiments carried out at small scale demonstrate that a unique relationship between this energy flux and the crack velocity does not exist, in contrast with theoretical predictions (see e.g. [1] for a review). Fractography experiments show that the increase in energy flux is accompanied by an increase of the fracture surface roughness [36, 33, 31, 37, 38, 39, 40, 41, 28]. This last one seems to depend on both the dynamic stress intensity factor, $K_d(c, v)$, and the crack velocity, v.

In the following we will describe in detail experimental techniques and methods and analytical methods which have permitted measurements of propagating cracks, observations of the patterns and roughness of the resulting fracture surfaces, and measurements of the acoustic emissions emitted by the propagating cracks. Discrepancies between the experimental observations and the theoretical predictions will be emphasized.

1.3.1 Limiting speed

Measuring crack velocities in a laboratory frame work is a challenging task. Four methods are commonly employed in experimental mechanics (see e.g. [32] for a review):

- High speed cameras are used enable to observe in real time the dynamics crack propagation in transparent materials [42, 40]. Nowadays, temporal and spatial resolution down to 1 μs and 100 μm, receptivity can easily be achieved. Moreover, the recorded images can be used to determine the crack fields parameters through photoelasticity [43], caustics [40, 44], or DIC [45, 46]. The main drawback of such methods resides in they high price.

- Wallner lines can be used to determine the crack speed quite accurately [9, 47]. These corrugations, observed on post-mortem fracture surfaces, result from the interaction between propagating crack fronts and shear waves radiated from the fracture [47]. From the location of the wave sources and the knowledge of the speed of transverse waves, one can indeed deduce both the direction of crack propagation and the crack speed along these Wallner lines [48, 9]. This technique for crack speed measurements can be improved by modulated crack surfaces by a continuous mode II perturbation of the crack with a shear wave at a frequency of about $f = 1$ MHz. This gives rise to the technique called stress wave fractography (see [9, 49] for a review). The main drawback of this technique resides in the its spatial resolution; which is set by the typical wavelength of the Wallner lines, about 1 mm in PMMA [50].

- Potential drop methods consist in depositing a thin conductive layer at the surface of the specimen [31, 51, 52, 53]. As the crack propagates, it cuts through the layer and increases the resistance. This increase is monitored at high speed (up to few tens of MHz) and the time evolution of the crack length is then deduced. The main difficulty in this method is that the layer resistance is not proportional to the crack length, but increases slowly at the beginning and diverges as the crack breaks completely the layer. Moreover, the relation between crack length and the resistance is extremely dependent of local variations of the film thickness. However, spatial resolution down to 200 μm were obtained using this technique [52].

- Electrical resistance grid technique consist in depositing a number of electrical wires (typically around 10-20) along the crack paths [54, 55]. Those are successively broken as the crack propagates, and the obtained electrical signal allows the estimation of the crack length and hence the crack speed. The estimated crack speed can be very high. However, as before, the electrical signal is usually not proportional to the crack length which prevents the placement of a large number of wires.

A large number of velocity measurements have been done using one or several of these techniques. Quite surprisingly, measurements suggest that in amorphous materials, the maximum velocity is significantly smaller than the Rayleigh wave speed predicted by fracture mechanics theory. As it is shown in table 1.1, the limiting crack velocity is only a fraction of c_R and lies within the range $\sim 0.4 - 0.7 \times c_R$.

Table 1.1: Limiting crack velocity for noncrystalline materials. From K. Ravi-Chandar [32]

Material	Author	limiting crack velocity, v/c_R
Glass	Bowden et al,	0.51
	Edgerton and Bartow	0.47
	Schardin and Struth	0.52
	Anthony et al,	0.66
	Sharon and Fineberg	0.55
PMMA	Cotterell	0.58
	Paxon and Lucas	0.62
	Dulaney and Brace	0.62
	Sharon and Fineberg	0.6
	Boudet and Ciliberto	0.7
Homalite-100	Beebe	0.33
	Kobayashi and Mall	0.37
	Dally	0.38
	Ravi-Chandar and Knauss	0.45
	Haunch and Marder	0.37

The origin of the limiting velocity less than c_R yielded many studies. Schardin [19] suggested that the limiting crack velocity could be considered as a new physical constant, and perhaps, it is related to other physical parameters that govern the fracture process. Cotterell [56] proposed that the maximum crack velocity depends mostly on the material properties. Then, Ravi-Chandar and Knauss [34] suggested that fracture is accompanied by a significant process zone in which nucleation, growth and coalescence of microcracks occur. This process zone is more important as crack velocity is large, which yields a rate and state-dependent fracture energy, Γ. Boudet and Ciliberto [57] showed that the value of the relevant Rayleigh wave speed can depend on the crack velocity: In most amorphous materials, the Young modulus depends on the solicitation rate. And the high-frequency acoustic waves emitted by the crack propagation can interact with the crack after reflection on the boundaries of the specimen. Boudet and Ciliberto proposed that this interaction should be incorporated into any description of crack motion. Finally, more recently Fineberg et al [58] observed that cracks running faster than $0.36 \times c_R$ in PMMA exhibited rapid oscillations in the crack velocity, triggered primarily by small microbranches issued from the main crack. They suggested that this dynamic path instability is the reason for the observed limiting speed.

1.3.2 Evidence of large-scale roughness at high velocities

In all the experiments concerning dynamic crack propagation, the morphology of *post-mortem* fracture surfaces can provide interesting information. As was described in previous section 1.2.2; the principle of local symmetry predicts that a moving crack progresses along a direction so has to remain in pure tension (mode I). This predicts smooth fracture surfaces at macroscopic scales. However quantitative fractography reports the existence of three zones with different roughness successively called *mirror*, *mist* and *hackle* surfaces.

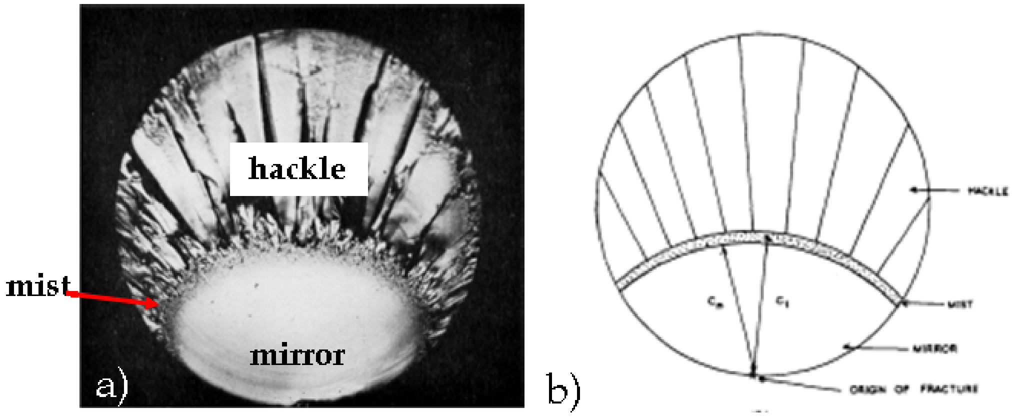

Figure 1.5: a) Mirror, mist and hackle zones on the fracture surface of a glass rod broken in simple tension (×20) b) Schematic representation of the fracture zones. From Johnson and Holloway [37].

These terms were introduced by Johnson and Holloway [37] and can be understood as followed:

- the mirror zone corresponds to smooth surfaces with no roughness apparent to the nacked eye.

- the mist zone surrounds the mirror region and exhibits a slight roughness that start to be apparent.
- the hackle zone coincides with relatively large irregularly oriented facets.

Figure 1.5 shows a microscope image with these three zones observed on the fracture surface of a glass rode broken in tension and its schematic representation.

A large number of experiments have been done to find a relationship between mirror, mist and hackle regions with both the fracture energy, Γ, and the crack velocity, v. Mecholsky et al, [39] deduce Γ from the radii of the initial flaw and the mirror region on silicate and non silicate glasses. Their calculations are in agreement with the results of double-cantilever-beam measurements. Ravi-Chandar and Knauss [34], using high-speed photomicrograph, observed the dynamic growth mechanisms in the mirror, mist and hackle zones in Homalite-100. They found the following evolutions for the crack front: (i)in the mirror zone, the crack front exhibits a thumb-nail shape, reminiscent of quasi-static crack propagation; (ii) in the mist region, several small cracks propagate simultaneously and the ensemble crack front is nearly straight; (iii) in the hackle zone, crack growth occurs by the same physical process than in the mist zone, except that the size scale of the microfracturing increases. They also showed that the stress intensity factor, K, increases, as the crack front changes from mirror to hackle regions. With respect to the surface roughness, experiments carried out in Homalite-100[34], Araldite, thermosetting epoxy [9] and various transparent plastics including PMMA [33] showed that the roughness varies almost continuously along the crack path and increases with K. These results are presented in Fig. 1.6

In the literature one can find other processes that cause observed patterns on dynamic fracture surfaces in a large number of brittle materials, called *conic marks*. These markings were observed in silicate glasses [61], polystyrene [62], cellulose acetates, steel and stainless steel [63, 64, 65], polystyrene [9], solithane [66], polymethylmethacrylate [55, 67, 66, 68] and spherulitic nylon [69], this last material being a semi-crystalline polymer. Figure 1.7 depicts several examples of surface markings. The high-stress field around a growing crack causes micro-cracking in the material ahead of the crack. These individual cracks grow and eventually link up with the main front. The volume of material under σ increases as K increases and with this, the damage zone also increases in size.

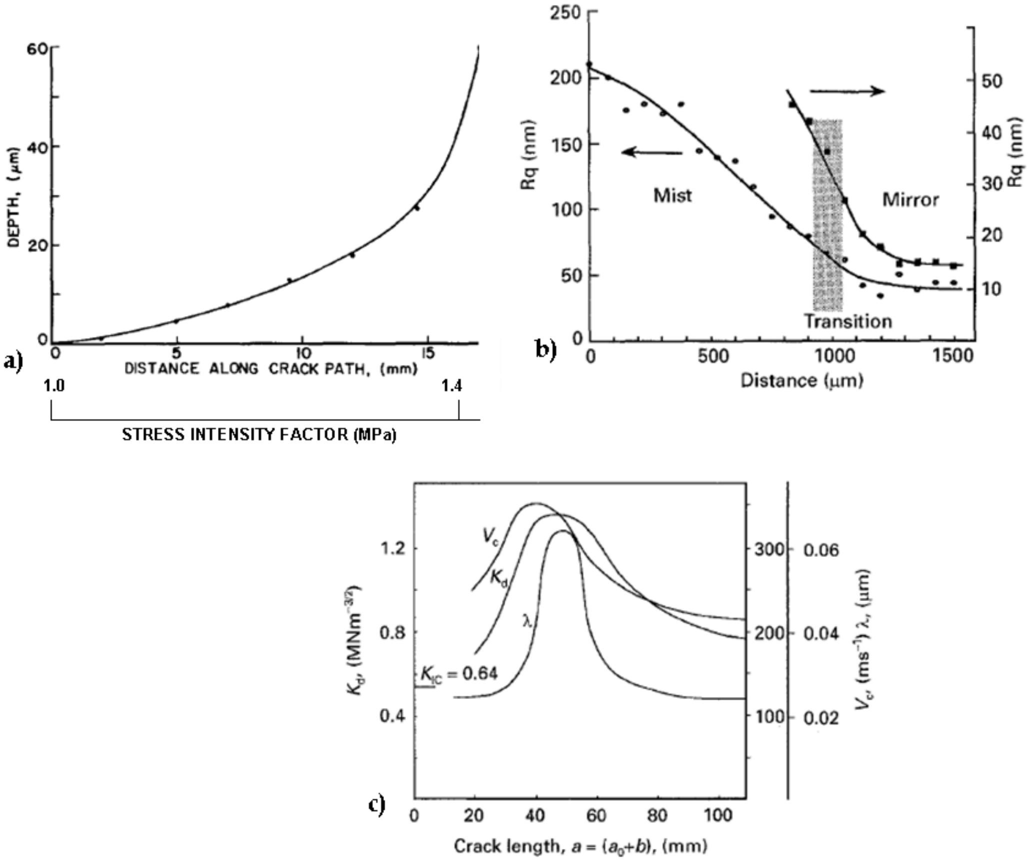

Figure 1.6: a)Graph showing the maximum depth of the fracture surface as a function of crack position and also K (MPa), from Ravi-Chandar and Knauss [34] b) Variation of roughness, R_q, across mirror transition determined by atomic force microscope (AFM), c)Dynamic stress intensity factor, K_d ($MNm^{3/2}$), crack velocity, V_c (ms^{-1}), and surface roughness, λ (μm) as a function of the crack length (mm) b) and c) are from D. Hull [59, 60].

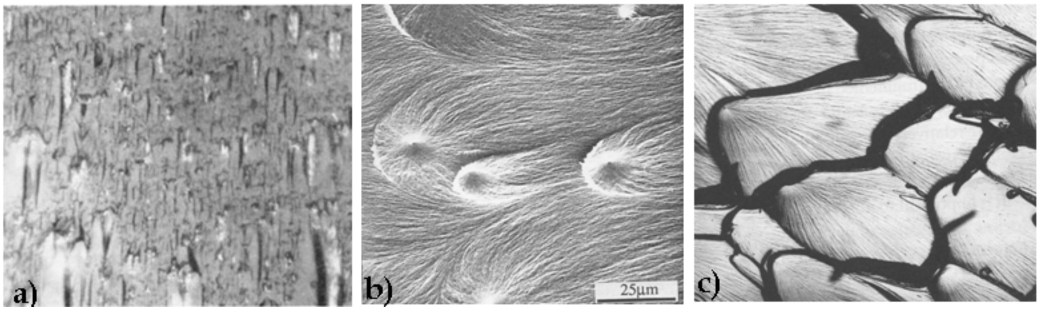

Figure 1.7: Conic marks observed on dynamic fracture surfaces of a)glass from [70] b) polystyrene and polyurethane, from [9]

.

The origin of conic marks was originally postulated by Smekal [61] in 1953. His model consisted in the enhanced stress field of a primary crack inhomogeneity or defect triggered by the initiation of a secondary microcrack ahead of it. The secondary crack may not be in the same plane as the primary front, and when these two fronts intersect in space and time, the ligament separating the two cracks breaks up leaving a conic marking on the fracture surface. The conic marking thus indicates a boundary level difference, marking the common space-time interaction of the two fracture fronts. The focus of the conic corresponds to the origin of the second fracture front. Yang and Ravi-Chandar [66] analysed the contour of a large surface images to then fit these markings with a second order equation to determinate shape(eccentricity) and the distance to the focus. They considered a planar crack front approaching a microcrack nucleus with a velocity v_c, when the distance between the crack front and nucleus is d_n the microcrack begins to grow radially and symmetrically at a velocity v_{cl}. d_n is the critical nucleation distance and is presumably dictated by the inherent characteristic of the material and the stress field. Then, they assumed that a second nucleus is at a spacing, s, from the first nucleus. The spacing s will in generally follow some statistical distribution, perhaps dictated by the local stress field and material microstructure. When the distance between the growing front of the first microcrack and the second nucleus is equal to d_n, the second nucleus starts to grow with a velocity v_{c2} (see schema in Fig. 1.8). For simplicity, assume that the velocities of the main crack and microcraks are identical and equal to v. Then the equation describing conic markings on the fracture surface is given by [32]:

$$\frac{(2x_1 + s - d_n)^2}{(s - d_n)^2} - \frac{4x_2^2}{(2s - d_n)d_n} = 1 \tag{1.23}$$

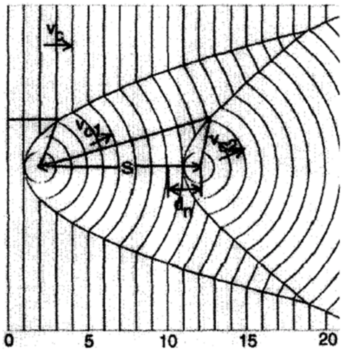

Figure 1.8: Geometrical model of formation of conic marks due to nucleation and growth of microcracks, courtesy of [32]

.

The statistic of the surface markings has been widely studied [55, 67, 66, 68]. These observations caused a controversy in the scientific community because some investigators proposed that the shape and density are dependent of the stress intensity factor and/or crack velocity [55, 66] and some others pointed out that they depend of the molecular weight in the case of polymers [67]. The observations of conic marks on the dynamic crack surfaces might indicate the onset of the mist zone with an increasing K, but further investigations are needed to clarify this suggestion.

The next question that one may have in mind is: what is the exact origin of the hackle zone is there another structured observed on dynamic fracture surfaces? As described above, surrounding the mist zone, a very rough region appears, the so-called hackle zone, as shown in Fig.1.5. In the hackle region, K seems to be much higher than in the mist region. Then, observations made by Johnson and Holloway [37] demonstrated the existence of macroscopic cracks which branch away from the main crack. This pattern has been observed subsequently in polystyrene[60] and Homalite-100 [40].

What is the mechanism at the origin of this pattern? A wide number of experiments were carried out to understand the origin of the micro and macro-branching. Here follows a brief summary of the observations about micro-branching:

- Ravi-Chandar and Knauss [40], Yang and Ravi-Chandar [66] proposed that micro-branching is the result of the nucleation, growth and coalescence of micro-cracks which appear on the process zone due to an increase in the stress intensity factor, K.

- ○ Hull [60] suggested that micro-branching is the result of a multiplicity of individual crack-tilting events involving the creation of mixed mode I/III stress fields and a highly complex array of crack fronts.
- ○ Fineberg et al, [15, 28] suggested that the origin of micro-branching is a dynamic instability that is triggered at a critical crack velocity.

And now what about the macro-branching? There is a large number of experimental and theoretical work carried out to understand the mechanism of the macro-branching and its relationship with the fracture roughness. Yoffe [16] in 1951 attempted to explain branching from an analysis of the problem of a crack of constant length that translates with a constant velocity in an unbounded medium. She found that the maximum stress acted normal to the lines and make an angle of 60 with the direction of crack propagation when the crack velocity exceeds 60% of the shear wave speed. Therefore, she suggested that this might cause the crack to branch whenever the crack velocity exceeded that value [34]. However, there is a discrepancy with [71, 72, 73, 74, 34] the predictions of Yoffe. Indeed, in the experiments the maximum branching angle that has actually been observed was limited, experimentally, by diffraction. In the case of micro-branching, the largest angle observed by Sharon et al, [75] in PMMA was reported to be 30 at a $3\mu m$ distance from the bifurcation point. On the other hand, the values of the "branching angle" for macroscopic branching that are reported in the literature are measured at distances typically of the order of $100 - 300\mu m$ from the branching onset [15]. The mechanism giving way to the macro-branching origin is still under discussion. Some workers believe that this process is due to the excess of fracture energy and a kind of transformation of the micro-branching [59, 60, 37, 39]. Experimental observations in PMMA show that, during crack propagation, several instabilities controlled by the local velocity, $v(c)$, appear at a critical velocity $v_c \sim 0.32 - 0.36 \times c_R$. They are characterized by the onset of velocity oscillations, a continuous high frequency sound emission of $f \sim 150kHz$ and surface roughness increases as $v(c)$ is increasing. When $v(c) \approx 0.45 \times c_R$ the crack branches in several different paths instability [31, 76, 15]. Another point of view was proposed by Ravi-Chandar and Knauss [34]. In their experiments they measured the dynamic stress intensity factor K_d during crack propagation. They observed that K_d

increases from 0.45 MPa$\sqrt{\text{m}}$ to 1.2 MPa$\sqrt{\text{m}}$ during the propagation at constant velocity. Then, when $K_d > 1.2$ MPa$\sqrt{\text{m}}$ the crack branched into three distinct parts with an angle of 65 for one crack, and the two others of 70, then instantaneously the K_d of the main crack dropped significantly to a value close to the initiation toughness K_c. From these observations they pointed out that when the crack reaches a critical stage identified macroscopically by K_d, it splits into two or more branches. They suggested that the mechanism for crack growth and branching is multiple-microcracking.

1.3.3 Acoustic emission

Dynamic crack propagation is accompanied by acoustic emission. Measuring the acoustic emission provides a useful tool to detect and localize the damage processes occurring at small scale prior to the catastrophic failure of a given specimen or structure (for more details see [77]). In this respect, acoustic emission measurements are widely used by seismologists to investigate earthquakes (see [78]). Experimental investigations were carried out on the acoustic emission that accompanied the dynamic crack propagation in glass and PMMA [31, 79]. In these experiments, the acoustic spectra of these two materials were measured for increasing velocities in both materials. The results of these experiments showed that the behavior of the acoustic spectra changed dramatically in both materials at values of $v \approx 0.36 \times c_R \sim v_c$ in PMMA and $v \approx 0.42 \times c_R \sim v_c$ in glass. This change coincide with the onset of micro-branching instability [80]. Above this critical velocity, high intensity peaks are observed in the acoustic emissions. In PMMA, the frequency of these peaks was on the order of the characteristic time scale observed in the velocity oscillations (about $2-3$ μs). In the case of glass the spectrum observed was peaked around $2-3$ MHz[15]. Experiments carried out by Boudet et al [31] in PMMA showed that the maximum sound energy in the fastest crack corresponds to about 1.5 J/m^2 which is roughly 1% of the minimum fracture surface energy, Γ. In these experiments they also observed that the acoustic emissions are weak until the propagating crack reaches a velocity of $v = 120 \pm 10$ m/s. They suggests that the acoustic emission increases when the surface becomes rough, as was previously observed [15, 80].

1.4 Scenarii and relevant experiments

After this brief introduction about the more relevant experiments carried out previously, we summarize and highlight the three scenarios which explained the discrepancies between the elastodynamics continuum theory, and the resulting observations:

- *Damage spreading through microcracking at high velocity.*
  Ravi-Chandar et al., carried out a large number of experiments in polymer plates (Homalite-100, PMMA, solithane, polycarbonate) and glasses of $500 \times 300 \times 4.76 mm^3$ dimensions. They used an electromagnetic loading device to generate stress wave loading on the crack surface. The crack tip stress field is monitored by the method of caustics in conjunction with a high speed camera. From the high speed cinematographs, they measured $K_{ID}(v)$ the dynamic fracture surface toughness and with this the dynamic stress intensity factor $K^d(t, v) = K_{ID}(v)$. High speed cinematographs allow them to obtain the crack extension histories and thus to deduce the crack velocity, $v(c)$. Along this line, Ravi-Chandar observed that initially a crack propagates at the level of the initiation stress intensity factor generating a mirror-like fracture surface. The crack cuts through voids that may be present or which have nucleated due to the crack tip stress field, with some of the voids diverging the crack to propagate along different planes, these are the origin of fracture surface roughening. When $K_d(t, v)$ becomes sufficiently high, the voids grow into microcracks well ahead of arrival of the main crack. This interaction leads to the well-known conic markings on the fracture surface. The idea of a single crack is no longer applicable at the scale of the fracture process zone. The microcracks within the fracture process zone interact with each other and under suitable conditions repel each other; these deviated microcracks then appear as microbranches. The experimental observations realized by Ravi-Chandar suggest that as the dynamic stress intensity factor K_d increases more microcracks will be activated in the fracture process zone. This mechanism of nucleation, growth, and coalescence of microcracks and their interaction with the crack front is responsible for the limiting crack velocity $v(c) \leq 0.6 \times c_R$ and the roughness observed on the fracture surfaces.

- *Interaction of sound with fast crack propagation.*
  Some years later, dynamic fracture experimental observations in PMMA were carried out by Boudet and Ciliberto [31]. Their experimental set-up was con-

sisting of a tensile machine with a sample of dimension $290mm$ in length, either 100 *or* $200mm$ in height, and the thickness varied from 1 *to* 10 mm. The velocity and the position of the moving crack was measured using an improved version of potential drop method (as described in section 1.3.1). The fracture energy was computed according Griffith criterion using $\Gamma = \frac{\pi p^2 l_c}{2E}$ where l_c is the notch length, p is stress applied, and E is the Young's modulus. From their experiments they observed that: *(i)* the dynamic properties of a moving crack do not depend on the sample thickness. They are basically controlled by the steady state velocity as well as local crack velocity $v(l)$, and *(ii)* the surface roughness increases dramatically at a velocity of $v(l) \simeq 0.5 \times c_R$, associated with a strong sound emission and broad band velocity oscillation. Then, the appearance of macro-branching was observed at $v(l) \simeq 0.65 \times c_R$, but this phenomena was only observed in fast cracks with a limiting velocity of $v(l) \simeq 0.75 \times c_R$. In order to understand the interaction of the sound emission with the moving crack, they improved their experimental set-up. The results show that in the case of *viscoelastic* materials as PMMA, the Young's modulus changes with the frequency of the sound emitted. In this scenario, they define two Rayleigh wave speeds, called static Rayleigh wave speed for low frequencies and the dynamic Rayleigh wave speed for high frequencies. Experimentally, they showed that both Rayleigh wave speeds are relevant to describe the crack motion, depending on the presence of a high-frequency acoustic wave. This wave is emitted by the crack and interacts with the crack after the reflection on the boundaries. They proposed to incorporate this interaction into any description of crack motion. Indeed, this interaction generates a constant terminal velocity jump [57].

- *Microbranching instability and the dynamic fracture.*
  Finally, the proposal suggested by Fineberg et al [15, 28]. Their experiments were carried out in PMMA and glass. The experimental setup used is a tensile machine loaded by uniform displacement of the vertical boundaries. The samples are sheets of size $380 \times 440mm^2$ in the x (propagation) and y(loading) directions, and thickness 2 and $3mm$, respectively. The crack velocity was measured by potential drop method (see section 1.3.1 for more details). The energy release rate $G(l) = \frac{K^2}{E}$ was computed numerically for the precise geometry of the plates used to then, deduced Γ from the equation of motion: $\Gamma = G(l)\left(1 - \frac{v}{c_R}\right)$. From these experiments, they observed an instability that occurs above a criti-

cal velocity, $v(l)_c < 0.4 \times c_R$, which leads to the apparent failure of equation of motion. At velocities above v_c, a single straight crack is no longer stable and undergoes a repetitive processes of micro-branching events. This leads to large oscillations in the crack velocity and roughening of the fracture surface, which are well-defined functions of the mean crack velocity. They observed that, even if the PMMA and glass are different materials, the appearance and subsequent evolution of many aspects of the instability are nearly identical. Thus, their proposal was based on the fact that at a critical velocity $v_c \geq 0.6 \times c_R$ the equation of motion is not appropriate to describe a moving crack, because this equation describes the motion of a single-crack state. Furthermore it fails when we attempt to use it to describe the mean velocity of a multi-crack state. The high peaks in the velocity measurements correspond to these single-crack states, because, when several cracks are propagating simultaneously, the available energy is distributed between them, and the front velocity drops.

1.5 Conclusions and Objectives

What can be gleaned from that? Because of stress concentration, crack propagation is the basic mechanism that leads to material failure. Presently, there exists a coherent framework, Linear Elastic Fracture Mechanics, predicting both the onset of crack propagation (Griffith's theory) and the crack velocity above this onset. This theory calls for the definition of a new quantity, the fracture energy, Γ, that encodes all the damage and dissipative processes occurring in a small zone at the crack tip, the so called process-zone. What sets precisely the value of Γ remains only partially understood.

Several discrepancies are evident when the theory predictions are compared to experiments. First, the limiting or maximum crack velocity is observed to be much lower than the Rayleigh wave speed predicted by the theory. Second, large scale roughness are observed at high speeds while continuum theory would predict smooth fracture surfaces. The understanding of these discrepancies yielded many investigations over the last decades. Several scenarii were imagined: (i) it was in particular suggested [32] that damage spreading through microcracking at high velocity provides the relevant additional dissipation mechanism responsible for the abnormal limiting velocity; (ii) it was also proposed [31] that the acoustic waves emitted by the propagating crack front can modify locally the material rheology at the crack tip, and hence the local value of the Rayleigh wave speed, by perturbing at high rate the crack loading; and (iii) it was finally conjectured [81] that the micro-branching instabilities observed at high velocities provides the relevant mechanism responsible for the discrepancy between theory and experiments. Note that the micro-branching onset coincides with an acoustic emission.

All these mechanisms are found to intervene at high enough velocity. This Ph.D. thesis is dedicated to the experimental investigation of dynamic crack growth in a brittle material, Plexiglas, over intermediate ranges of crack velocity, below the onset of micro-branching instability and acoustic emission. The experimental set-up designed to reach this goal is described in chapter 2. We will see, in chapter 3, that the fracture energy exhibits an anomalous increase from its value at crack initiation at a well-defined critical velocity, below the one associated to the onset of micro-branching instability. This transition is associated with the appearance of conics patterns on fracture surfaces. Conic marks, in many materials, are the signature of damage spreading through the nucleation and growth of micro-cracks. In chapter 4, we will see how the dynamics of crack propagation and microcracking can be reconstructed at the microscopic scale (micrometer/microsecond scale) from the analyses of the *post-mortem* fracture surfaces.

.

Chapter 2

Materials, experimental setup and methods.

In this chapter, we present the experimental setup developed during this PhD thesis to investigate dynamic crack propagation in nominally brittle materials. This setup fulfills three main requirements:

- Allows for the growth of a stable *dynamic crack* in a controlled manner.
- To follow in real time (at the microsecond scale) the relevant *macroscopic quantities* in dynamic fracture, namely the instantaneous crack velocity and the instantaneous (quasi-static) stress intensity factor.
- To probe the damage and fracture processes responsible for dynamic crack growth at the micro-scale.

The materials, experimental setup and analysis methods which have been selected and/or developed to reach these objectives are presented hereafter. PMMA was chosen as the archetype of a brittle amorphous material and most of the experiments were conducted using PMMA. Preliminary experiments were performed using soda-lime glass. The properties of these two materials are described in section 2.1. The following 3 sections of this chapter detail each component composing our experimental setup: (i) the various geometries of fracture test designed during this work. (section 2.2); and (ii) the method we developed to measure the crack velocity (section 2.3). Then, section 2.4 presents the finite element simulations used to compute various parameters allowing for the characterization in real-time of the stress field evolution in the vicinity of the dynamic crack. The last part of this chapter, describes the microscopy techniques employed to obtain the fracture surface images for the *post-mortem* analysis.

2.1 Materials

The first step was to find a model experimental material in which dynamic cracks can be generated and propagated in a controlled manner. Glass appears as the archetype of brittle materials and was then naturally our first choice. However, because of the extremely high Young modulus ($3GPa$ and $70GPa$ for the PMMA and soda-lime glass respectively), the typical values of the displacement in a fracture experiment are very small (around $5\mu m$ to $1mm$ behind the crack tip in our typical experiments). This makes the stability of dynamic cracks very dependent on slight misalignments, inaccuracies and asymmetries in the design and machining of the experimental set-up and the various specimens. Therefore, most of the experiments described in the next chapters were conducted in PMMA. Its lower value in Young modulus makes the experiments far less sensitive to the small inaccuracy and misalignments. All the experiments were carried out in ambient conditions. The mechanical properties of both Soda-lime and PMMA are reported in table 2.1, while the methods used to measure these quantities are described below.

2.1.1 Soda-lime glass

Soda-lime glass is a homogeneous, isotropic and brittle material, with unique optical properties. Indeed glass is perfectly homogeneous at length scales much smaller than those of optical wavelength. Moreover, it exhibits a hardness significantly larger than that of steels. The glass transition is observed at the critical temperature $T_g \simeq 700°C$. At ambient temperature, the viscosity is larger than 10^{19} Pa.s. Therefore it can be considered as a perfect elastic brittle solid at ambient temperature.

Density of soda lime is simply measured using the weight and the well defined dimensions of a parallelepiped specimen. It is found to be $\rho = 3.03 \pm 0.1kg/dm^3$. Elastic modulus, E, and Poisson ratio, ν, are evaluated using acoustic techniques: Both dilational and shear pulses of frequency $f = 5$ MHz are sent into a specimen of thickness $20mm$ and the successive echoes are recorded via an oscilloscope (Figure 2.1). From the successive arrival times of the pulse at the transducer, one can deduce the dilational, C_d, and shear, C_s, wave speeds. They are found to be:

$$C_d = 5700 \pm 20m/s \quad C_s = 3400 \pm 10m/s \tag{2.1}$$

From the velocities C_d and C_s, one can deduce the values of the Poisson ratio and the Young modulus [32]:

$$\nu = \frac{C_d}{C_s}, \quad E = \frac{C_s^2}{\rho} \frac{3C_d^2/\rho - 4C_s^2/\rho}{C_d^2/\rho - C_s^2/\rho} \tag{2.2}$$

yielding:

$$\nu = 0.22 \pm 0.01, \quad E = 73 \pm 0.2 \text{ GPa} \tag{2.3}$$

As explained in section 1.2.1, the relevant velocity for fracture is the Rayleigh speed c_R. This velocity is given by the first root of the Rayleigh function (see section 1.2.1):

$$R(c) = 4\alpha_d\alpha_s - (1+\alpha_s^2)^2 \quad \text{with} \quad \alpha_d = (1-c^2/C_d^2)^{\frac{1}{2}} \quad \text{and} \quad \alpha_s = (1-c^2/C_s^2)^{\frac{1}{2}} \tag{2.4}$$

From the values of C_d and C_s given in equation 2.1, one gets in soda-lime glass:

$$c_R = 3120 \pm 10m/s \tag{2.5}$$

2.1.2 Polymethylmethacrylate (PMMA)

PMMA is a linear polymer with a glass transition at $T_g \simeq 100°C$. At ambient temperature, it can be considered as an elastic material. This kind of material is considered as one of the archetype of brittle elastic material and, as such, as been widely investigated in dynamic fracture experiments.

The density of PMMA is measured to be $\rho = 2.8 \pm 0.2$ kg/dm^3. The speed of bulk waves are computed using the same acoustic techniques as those used in

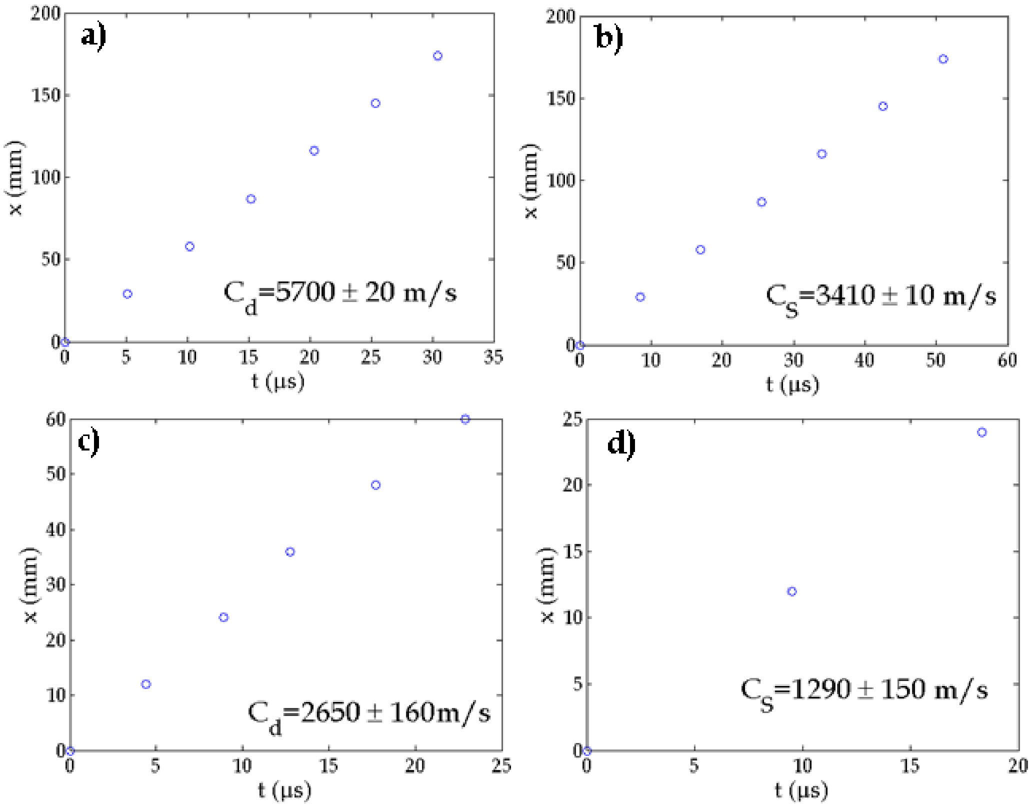

Figure 2.1: Speed of dilational, C_d, and shear waves, C_s: a) and b) Soda-lime glass, c) and d) PMMA.

soda-lime glass (Figure 2.1). They were found to be $C_d = 2650 \pm 160$ m/s and $C_s = 1290 \pm 150$ m/s, respectively. From these values, the Poisson ratio and Young modulus are computed using Eq. 2.2. They are found to be:

$$\nu = 0.33 \pm 0.08, \quad E = 5.4 \pm 0.1 \text{ GPa} \tag{2.6}$$

These values should be noted. The Young modulus is significantly higher (about two times larger) than those usually reported in the literature (see e.g. [32]). To understand this apparent discrepancy, it is important to note that our measurements were performed at a frequency of $f = 5$ MHz. And contrary to Soda-lime, the PMMA rheology is expected *to depend significantly* on f at such high values (see e.g. [57]). The Poisson ratio is expected to remain approximately constant [57]. This value of E is then irrelevant when one seeks to estimate the mechanical energy in a PMMA specimen during its breaking. The relevant one is the one measured at low frequencies, where E becomes independent of f [57, 15, 32].

In order to overcome this difficulty, we refine our estimation of the elastic modulus using a standard mechanical test providing with quasi-static information: we perform a Dynamic Mechanical Analysis (DMA), in collaboration with Unit Mixte at Saint-Gobain Research. DMA works by applying a sinusoidal deformation to a sample of known geometry. The sample is subjected to a controlled stress or controlled strain. For a known stress, the sample will then deform a certain amount. In DMA this is done sinusoidally at various different frequencies (see Figure 2.2). How much it deforms is related to its stiffness. A force motor is used to generate the sinusoidal wave, and this is transmitted to the sample via a drive shaft. Hence, the stress is computed as a function of the deformation. The Young's modulus, is then calculated from the slope of the initial part of a stress-strain curve, and it is found to be $E = 2.8 \pm 0.2$ GPa.

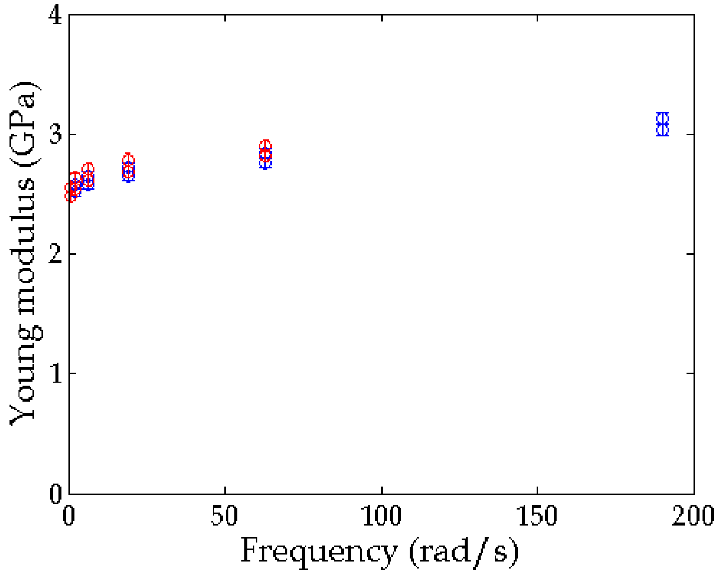

Figure 2.2: Young modulus of PMMA computed from DMA tests at various frequencies. Each color represent a test.

Correct values of Poisson ratio and Young modulus to consider when one is interested in interpreting the fracture experiments described in the next sections is:

$$\nu = 0.3251 \pm 0.076, \quad E = 2.8 \pm 0.2 \text{ GPa} \tag{2.7}$$

The values of the dilational and shear wave speeds can then be deduced through [32]:

$$C_d = \sqrt{\frac{\lambda + 2\mu}{\rho}}, \quad C_s = \sqrt{\frac{\mu}{\rho}} \quad \text{with} \quad \lambda = \frac{\nu E}{(1+\nu)(1+2\nu)}, \quad \mu = \frac{\lambda - 2\lambda\nu}{2\nu} \tag{2.8}$$

yielding:

$$C_d = 2000 \pm 360 \text{ m/s}, \quad C_s = 950 \pm 10 \text{ m/s} \tag{2.9}$$

Furthermore the Rayleigh speed is found to be::

$$c_R = 880 \pm 20 m/s \tag{2.10}$$

Table 2.1: Mechanical properties of soda-lime glass and PMMA used in our fracture experiments

	E(GPa)	ν	Density ρ(kg/dm^3)	C_d (m/s)	C_s (m/s)	c_R (m/s)
Glass	73 ± 0.3	0.22 ± 0.01	3.03 ± 0.1	5700 ± 20	3410 ± 10	3120 ± 10
PMMA	2.8 ± 0.2	0.33 ± 0.08	2.8 ± 0.2	2000 ± 360	950 ± 10	880 ± 20

2.2 Mechanical device

The next step was to design and machine an apparatus (tension/compression) for fracture tests in which we could get: (i) a stable dynamic crack growth (which means velocities ranging between $0.7c_R \sim 0.1c_R$); and (ii) a "single" macroscopic crack front (which means fracture surfaces free of macro-branches).

The apparatus used to carry out the experiments was home made(see Fig. 2.8). One jaw of the machine is fixed while the other moves via a step motor (Oriental motor EMP400 Series) allowing incremental tunable displacements as small as 40 nm. In all the experiments presented herein, the velocity of the moving jaw is set to 40 μm/s. The force is measured , either in tension or compression, up to 20 kN thanks to a S-type Vishay load cell 363 Series. The effective compliance of the loading apparatus was measured by loading in compression a rectangular glass specimen of length $L = 200$ mm, width $W = 50$ mm and thickness $H = 20$ mm. It was found to be $k^{app} = 2.4 \times 10^7$N/m.

2.2.1 Thin strip configuration

The first fracture tests were driven in the so-called *thin strip configuration*, i.e. by applying a constant displacement to the parallel boundaries of a thin rectangular specimen (see figure 2.3). This geometry was our first choice since:(i) It allows to drive steady cracks that propagate a constant velocity and constant mechanical energy release rate G over a significant portion of the specimen as it is; (ii) G can be simply estimated and related to E, ν and the width extension δ of the specimen at fracture onset : $G = \frac{E\delta^2}{2w(1-\nu^2)}$; and (iii) lastly because it is a standard mechanical configuration used in many labs to study dynamic fracture experiments (see e.g. [31, 52, 82]). In this geometry, it is expected that the crack propagates at a constant velocity which can be controlled as it only depends upon the geometry (i.e. radius of curvature and length) of the pre-crack or notch which is introduced in the sample.

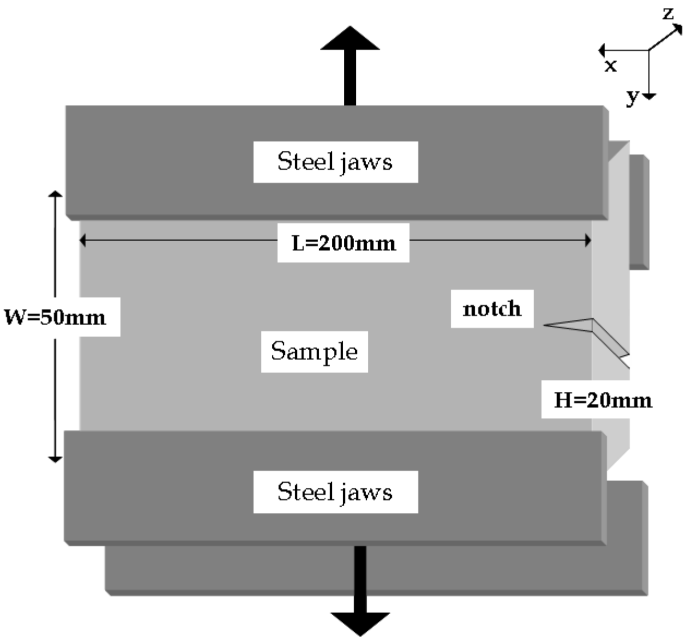

Figure 2.3: Sketch of the so-called thin strip configuration.

Both soda-lime glass and PMMA were broken in strip configurations (see Tab. 2.1

for relevant mechanical properties). The samples have a rectangular shape of length $L = 200$ mm, width $W = 50$ mm and thickness $H = 20$ mm. In all the following, the x-direction, y-direction and z-direction are defined as the direction of propagation (L-direction), direction of the tensile stress at the crack tip (W-direction), and direction of the crack front(H-direction), respectively. The sample is glued with cyanoacrylate adhesive to steel frames (see figure 2.3) that are subsequently clamped to the jaws of the loading machine. Prior to the loading, a small 10 mm-long 'seed' crack is introduced at the edge of the sample, midway between the steel frames. One of the two jaws is then pulled at a constant velocity of 40 μm/s, which imposes a constant width extension. At a given point, a crack propagates dynamically, and the specimen breaks.

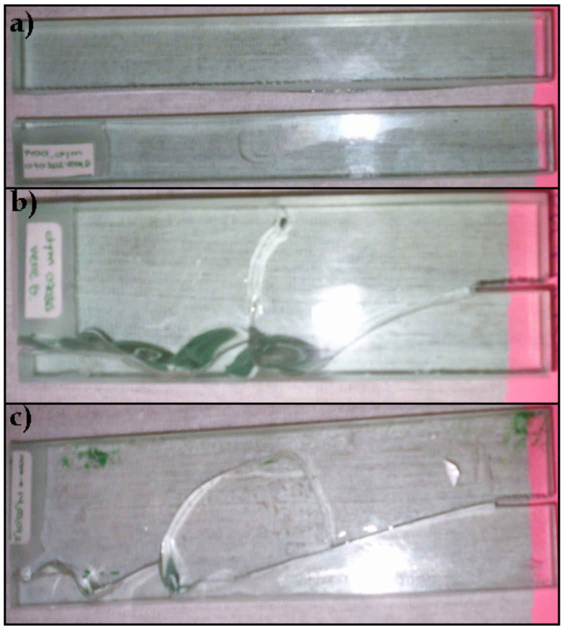

Figure 2.4: Samples broken with the thin strip device.

We carried out a large number of experiments of this kind. Unfortunately, in almost all, the crack path is unstable. Sometimes, it departs rapidly from the symmetry axis and reaches one of the two boundaries (as can be seen on Fig. 2.4b). In some other cases, we observe fragmentation and macro-branching (as shown in figure 2.4c). The only occasion where we obtained stable crack propagation (figure 2.4a) was when a 1 mm-deep groove is dug on the surface to guide the crack along the long edge. But the presence of this guide imposes mixed mode in the loading of the moving crack. This geometry was therefore given up.

2.2.2 Wedge splitting geometry

In order to have a stable crack propagation, we had the idea to break our samples in opening mode (mode I) while imposing a compression parallel to the direction of crack propagation. Within these conditions, if the crack deviates from straightness, its front is loaded under compression, and therefore goes back along the symmetry direction. The geometry which allowed us to reach this objective is the so-called wedge splitting geometry [83, 50, 84]. In this test, a steel wedge is slowly pushed into a seed crack (see figure 2.5). In this geometry, the specimen is compressed along the direction of crack propagation (x-axis) while the crack loading remains in opening mode.

Such fracture tests were performed in both PMMA and Soda-lime glass. A schematic of the sample is shown in figure 2.5. A thin rectangular notch (length of 10 mm, thickness of 2 mm) was cut out of one of the edges of plate of length $L = 140mm$ (x-direction), of wide $W = 120mm$ (y-direction) and thickness $H = 15mm$ (z-direction). A steel triangular wedge is then slowly pushed (velocity of 40 μm) into the notch up to crack initiation.

In this so-called wedge splitting geometry, the release mechanical energy G decreases as the crack length, c, increases, thus, one should expect to have a decreasing velocity as the crack length is increasing. To obtain dynamic failure, we then introduced a hole of tunable diameter from 2 mm to 8mm at the end of the seed crack (see figure 2.6). The hole diameter determines the crack dynamics: The larger the hole is, the higher the stored energy in the sample at the onset of cracking is, and hence, the faster the crack. This hole blunts the seed crack and hence will determinate the amount of mechanical energy stored in the sample is high, the crack starts to propagate at high velocity, and it decreases as the crack length increases.

This geometry allows us to reached most of our objectives since it allows the propagation of a stable dynamic crack with velocities ranging from $0.7 \times c_R$ to $0.5 \times c_R$ in both PMMA and soda lime glass. However, the force is applied on a single point at the notch inducing local plastic deformation and also friction at the contact point between the notch and the specimen. This prevents to estimate properly the mechanical energy release rate, G, in the system. This lead us to improve this geometry.

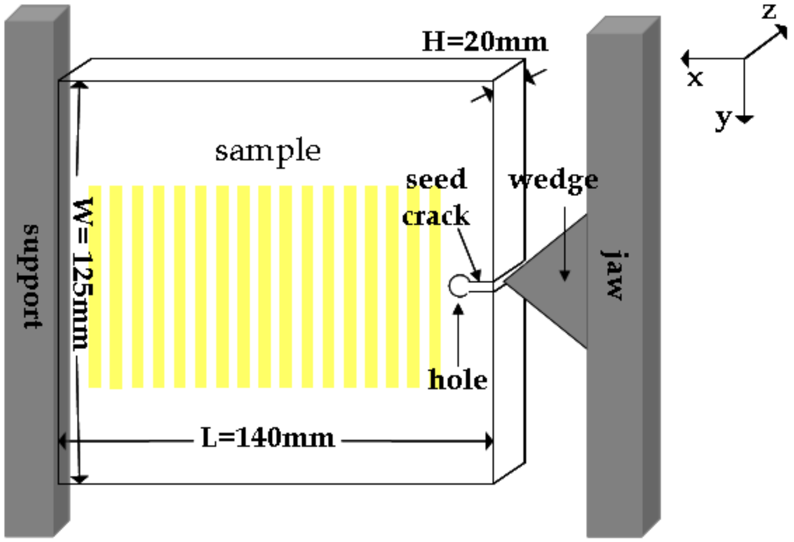

Figure 2.5: Schematic representation of the wedge splitting configuration

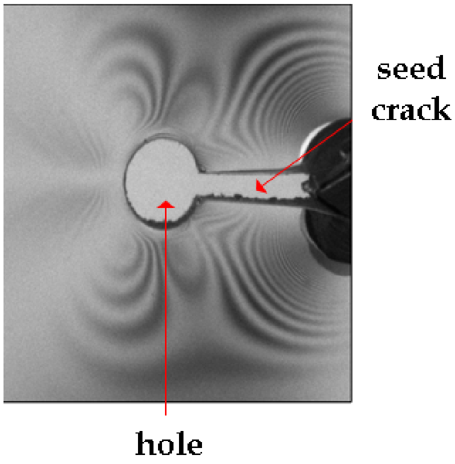

Figure 2.6: Image showing a PMMA notch configuration designed for the wedge splitting experiments. To do this, the sample was placed between two cross-polarizers, which allows to observe the stress distribution around the loaded hole as PMMA is a birefringent material.

2.2.3 Improved wedge splitting geometry

To prevent the appearance of plastic deformations around the notch of the sample, we modify the geometry of our setup and samples so that the force applied by the loading machine is spread over a significant contact area within the specimen (see e.g.[85, 86]). In this context, a rectangular grove is now cut out of one of the specimen edges. Two steel blocks equipped with rollers are then placed on both sides of this mouth (see figure 2.7). The specimen is then loaded by pushing a wedge (semi-angle of 15) at constant velocity 40 μms^{-1} in between these two blocks (see figure 2.7). Then, the force is applied on a very small contact area at the extremity of the notch. This modification allows to spread the loading force over a large contact area and prevents the formation of plastic deformations.

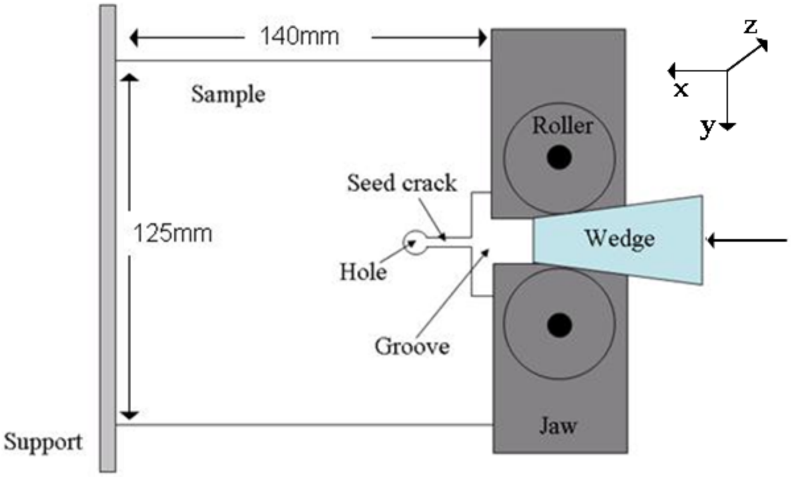

Figure 2.7: Schematic representation of the modified wedge splitting device

To be more precise, the specimen are prepared from 140 × 125 × 15mm^3 parallelepipeds. A rectangular mouth of 25×25mm^2 is cut out of one of the 125mm×15mm edges. An additional rectangular 10 mm-long 2 mm-thick notch is dug deeper in the middle of this mouth. As before, a hole of adjustable diameter ranging from 2 to 8 mm is drilled at the end of the groove to tune the crack dynamics. Figure 2.8 shows a picture of this new configuration.

Only PMMA samples are broken in these series of experiments. The maximum crack velocity is observed at the onset of crack propagation and ranges between $0.7\times c_R$ and $0.5 \times c_R$. Then the velocity decreases as the crack length increases. The crack propagation ends at low velocity, typically around $0.05 \times c_R$.

In all the tests described above, both displacement and force are recorded via a computer with a time-resolution of 1 s, limitation set by a multimeter. The last value

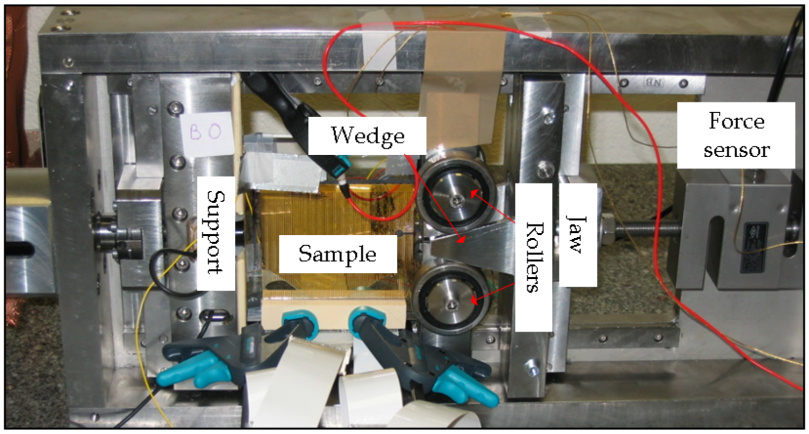

Figure 2.8: Image showing the modified wedge splitting device

of the applied force is registered when the crack starts to propagate. This is the value used in the finite element analyses described in section 2.4.

2.3 Crack velocity measurements

The next goal of the experimental setup was to measure the instantaneous crack velocity. There are 4 methods commonly used in experimental mechanics to obtain the instantaneous crack velocity (see e.g. 1.3.1 for a review).

In our experiments, we used a modified version of the electrical resistance grid technique [54, 31, 55, 52], as is shown in the sample of figure 2.8. A large number of conductive bands are arranged such that an accurancy of 40 μm and 0.1 μs in space and time respectively is obtained. Our setup was developed in two stages.

In the preliminary setup, 25 graphite stripes were printed on the surface. They were painted by hand using a metallic mask as a guide. Their dimensions are ~ 1 mm in width (along the x-direction) and 100 mm of length (along the y-direction). The first strip is located 15 mm away from the tip of the seed crack. The others are positioned parallel to the first one, every 4 mm. The last one is 10 mm away from the back edge. Each strip is connected in series to a resistor $R = 120$ KΩ. This resistor was chosen to be extremely high with respect to that of the strip (about few Ω) so that this last one is negligible. All of these circuits (stripes+R) are then connected in parallel, together with an additional resistor, R. The effective resistance of this circuit is then directly proportional to the number N of stripes that will be cut, i.e. of the crack length. Finally, a small resistance $R_M = 1 \ \ \Omega$ is added in series, the whole electronic circuit is alimented with a voltage source that imposes a constant tension $V_e = 16$ V, and the tension V_M is read at the boundaries of R_M. As the crack front propagates, the conductive graphite strips are cut at successive times, N increases by steps, and V_M increases by steps of sizes $R_M V/R$. The time location of these jumps are detected with an oscilloscope and allows to compute the crack velocity.

In the refined version of this setup, 90 stripes are deposited on the sample surface. This was using polymer masks fabricated by APTETUDE glued on a sample surface. Stripes width and length are 500 μm and 100 mm, respectively. They are separated by gaps of 500 μm. The first strip starts at 500 μm from the seed crack, and the last one is localized at 5 mm before the end. The conductive layers are then deposited on the specimen through the polymer mask at the Laboratoire de Chimie des Surfaces et Interfaces (LCSI) at SPCSI, CEA Saclay. It consists of the superposition of two successive layers: A 2.4 nm-thick chromium layer, and an additional 23 nm- thick gold layer. The chromium improves adhesion between the conductive gold layer and the PMMA or Soda-lime substrate. The accuracy of the stripe thickness was measured to be 40 μm.

The 90 conductive stripes are connected in series to 90 resistors of 30 KΩ each. The advantage to using gold and chromium instead of graphite is that their resistence is very low (less than 1 Ω). In order to have a better resolution and less noise to capture the entire length of the crack with high spatial resolution, four channels of the oscilloscope are cascaded, each with different offset, so that each channel is triggered as the previous one gets out of its range. Figure 2.9a and b shows the measured signal. As $V_M = V(\frac{R_{mes}}{R})N$ varies with the crack length measuring the raw voltage signal provides us with the crack length, c, as a function of time (see figure 2.9 c). From this signal we compute the crack velocity as a function of c, as shown in figure 2.9 d.

This technique allows us to follow the crack progression along 90 points separated by a distance of $1mm$, with spatial and temporal accuracy of 40 μm and 0.1 μs respectively.

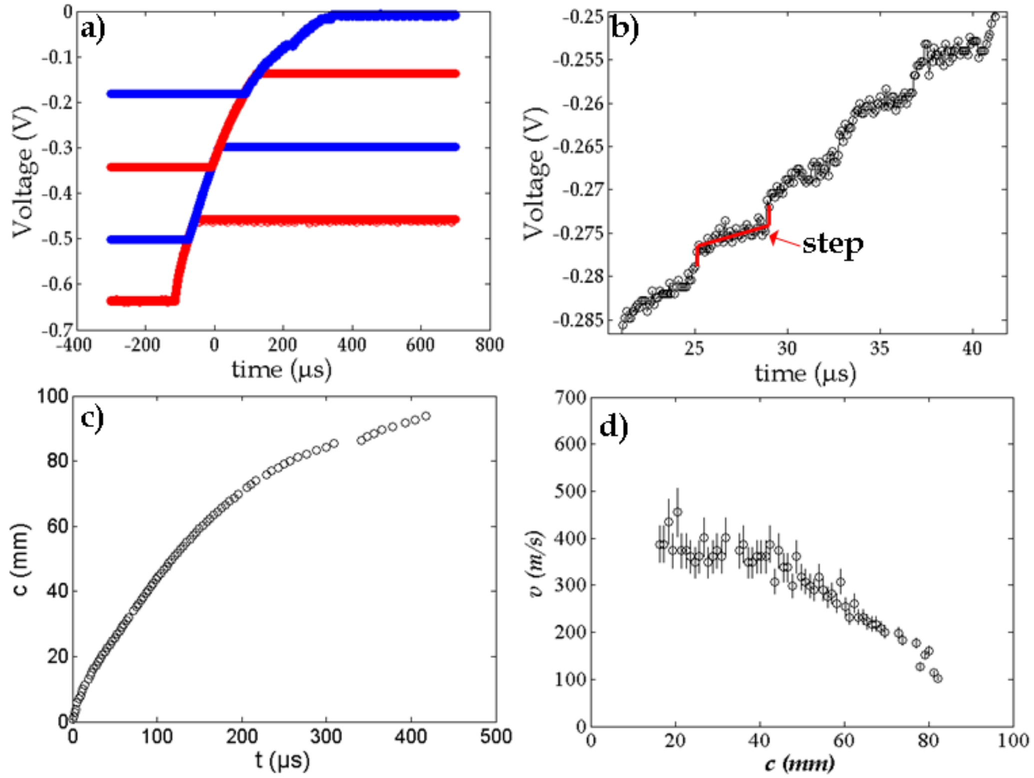

Figure 2.9: Images showing the methodology used to compute the results obtained from the modified potential drop method during our fracture tests a) Voltage (V_M) as a function of time (t) from the signal registered with the oscilloscope. b) Zoom on the oscilloscope signal, we can clearly see the steps corresponding to successive cuts of conductive lines as the crack front advances. c) Crack front position as a function of time and d) crack velocity calculated at 90 crack positions.

2.4 Finite element method

Fracture experiments span typically over a few hundreds of microseconds. This time scale is far too short to follow in real-time the time evolution of the loading force or the jaw displacement. Hence, finite element analysis is used to estimate the evolution of the mechanical parameters during crack progression. It was verified experimentally that over a time scale of a few hundreds of microseconds, the load cell did not respond to the changes related to crack propagation. This is due to the time required for sound waves to travel back and forth between the crack tip and the load cell within the PMMA sample and the steel loading apparatus. As a result, the jaws displacements will be assumed to be constant during the crack propagation. For finite element calculations this translates into constant displacement boundary conditions.

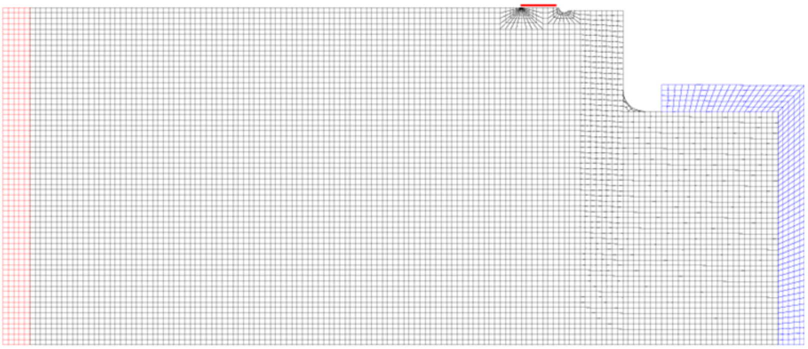

Figure 2.10: Typical meshing used for finite element calculations, in order to access the stress/strain fields in the experiments. Red: polymeric layer. Black: sample. Blue: rectangular mouth. Red line: cracked line.

Figure 2.10 represents the meshing of the complete system, including the sample (black), a polymeric layer between the sample and the loading apparatus (red) and mouth (blue). The average mesh size is 1 mm and reduces logarithmically down to 10 nm at the crack tip, in order to resolve in space the crack tip opening. Only half of the system is required for symmetry reasons. For each sample, the equilibrium position of the wedge yielding the measured applied load at the onset of crack propagation was determined using a plane stress static finite element code (Castem 2007). During crack propagation, the point of the mouth corresponding to the roller axis is allowed to move along the wedge side, i.e. at the wedge angle of 15.

The quasi-static stress intensity factor is then determined, for each crack length

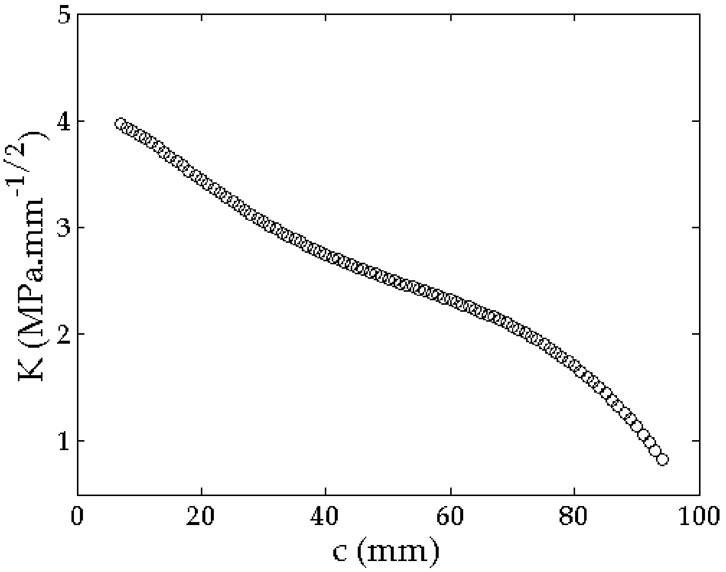

Figure 2.11: Static stress intensity factor, K, as a function of the crack length, c.

c using the J-integral method [87]. A typical result is shown in figure 2.11. Such calculations are performed for increasing crack length, c, between the hole and the end of the sample. Note that the first and last 5 mm were not accessible because of the size of the transition zone of the meshing around the crack tip.

As was explained in section 1.2.1, these values of the quasi-static crack tip stress field allows, using the equation of motion, and along with the velocity measurements, to deduce the dynamic fracture energy.

2.5 Topography measurements of fracture surfaces

Finally, in addition to previous measurements, we investigated *post mortem* morphology of the fracture surfaces and correlated it with other quantities. Indeed, *post mortem* fracture surfaces preserve information of the local interactions between the crack front and material defects and, as such, reflect the various damage processes occurring at the microscale. In this section we will describe in detail the two microscopes that were used for these analysis.

2.5.1 Optical microscope

.

A Leica DM2500 microscope was used to image the fracture surface. Most of the images were taken with a ×5 objective, with polarized light at 135 between the two layers of polarizers. The resulting images are 1.4×1 mm^2 in size, with a pixel size of 677 nm. In order to gather statistics for the *post mortem* analyses, 150 images all the long were taken from all the dynamic fracture surfaces. Figure 2.12 shows a few representative images.

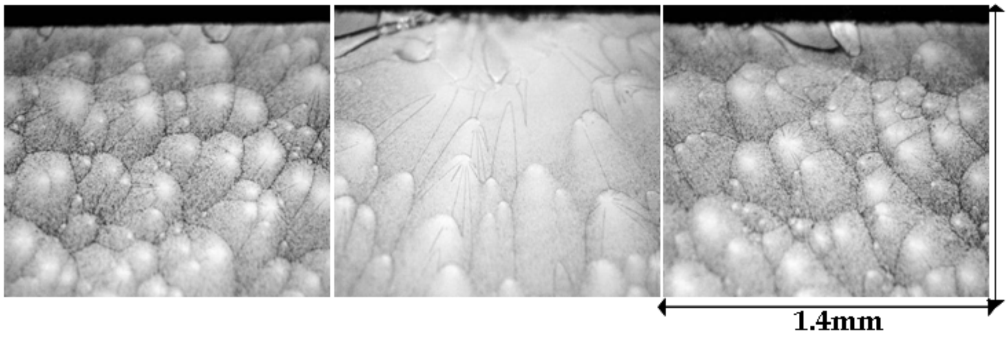

Figure 2.12: Microscope images ×5 objective taken from the dynamic fracture surfaces.

These images provide us large amounts of information of the dynamic fracture surfaces, but only in 2 dimensions. For this reason, we imaged the fracture surfaces with an optical profiler which allows one to gather information in $3D$.

2.5.2 Optical profiler

.

Three dimensional images were obtained via an optical profilometer (produced by FOGALE Nanotech). This work was done in collaboration with the group of Systmes Biologiques Intgrs located in the Laboratoire de Physique Statistique at Ecole Normale Superieur de Paris. The images were taken with a ×5 objective, giving a physical resolution of 1.86 um per pixel in-plane and 0.1 nm out-of-plane. The image size is 1.4 mm × 1 mm. Figure 2.13 shows an image (a) and a profile

(b) taken with this profilometer on a typical zone of a dynamic fracture surface in PMMA.

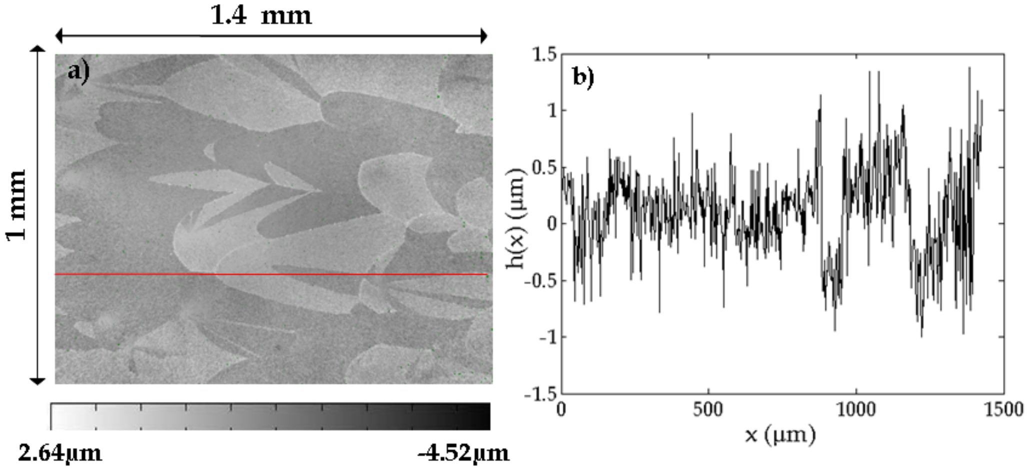

Figure 2.13: a) Example of an optical profilometer image taken from the fracture surface of PMMA, b) Profile taken from the optical profilometer image (red line)

2.6 Conclusion

The experimental setup and associated analysis tools have been presented. We are now able to:

- Propagate a dynamic crack in nominally brittle materials like oxide glass and PMMA in a stable and controlled manner over a wide range of velocities.
- Record in real time by a combination of measurements the instantaneous spatially averaged crack velocity. Subsequently, we can calculate via finite element simulations the (quasi-static) stress intensity factor. These two quantities give an estimation of the instantaneous mechanical energy released as the crack propagates and the stress field singularity in the vicinity of the crack tip.
- Probe the resulting post-mortem fracture surfaces which contains information on the local damage and fracture processes.

In a first step, one will see how the data obtained from this experimental setup can be used to determine a macroscopic equation of motion for cracks (see Eq. 1.22).

In this equation, all the dissipation processes are gathered into a single quantity, the fracture energy, Γ, which will be determined experimentally as described in the next chapter. Chapter 4 details damage processes at the microscopic scale. Hence one can better understand the nature of the dissipation processes.

Chapter 3

Macroscopic study: Nominally brittle to quasi-brittle transition in dynamic fracture

This chapter is dedicated to the study of dynamic crack propagation in brittle amorphous materials at the macroscopic scale. The theoretical reference of this work is Linear Elastic Fracture Mechanics (LEFM). It states that all energetic dissipations can be gathered into a single material-dependent quantity, the fracture energy (Γ). The crack growth velocity, v, is then selected by the balance between the energy flux and the dissipation rate, which leads to (see section 1.2.2):

$$\Gamma \simeq (1 - v/c_R)\,\frac{K(c)^2}{E} \tag{3.1}$$

where c_R and E are the Rayleigh wave speed and the elastic modulus of the material, respectively, and $K(c)$ is the Stress Intensity Factor for a quasi-static crack of length c. K depends only on the applied loading and specimen geometry, and it characterizes entirely the stress field in the vicinity of the crack front.

Large discrepancies between LEFM predictions and experiments have been reported at large velocities (see chapter 1.3 or [15, 32] for reviews). In particular:

- The measured maximum crack speeds lie in the range $0.5 - 0.7 \times c_R$, i.e. far lower than the limiting speed c_R predicted by equation 3.1.

- ∘ Fracture surfaces become rough at high velocities, contrary to the smooth surfaces predicted by PLS.

Careful measurements of the velocity dependence of Γ have recently yielded important insights on the fracture mechanisms within the velocity range $0.2 - 0.9 \times c_R$. In particular, it has been observed that beyond a critical velocity, $v_b \simeq 0.4 \times c_R$ ($v_b \simeq 0.35 \times c_R$ in PMMA (see ref. [81]), the crack front splits into multiple-cracks formed by repetitive, frustrated micro-branching events. The micro-branching instability origin is frequently disputed between theoreticians and experimentalist. However, they reconcile their differences when the velocity is lower than v_b [28].

Despite this reconciliation, a number of puzzling observations remain at smaller velocities. In particular, even for velocities much less than v_b: (i) the measured dynamic fracture energy is generally significantly larger than that at crack initiation [88, 89, 90, 28] and (ii) fracture surfaces roughen over length scales greater than the microstructure scale ("mist" patterns) [9].

In this chapter, we report measurements of Γ in PMMA at crack velocities within the range $0.05 - 0.5 \times c_R$ (section 3.1). Our results show for the first time an abrupt 3-fold increase in Γ at a new critical velocity $v_a \simeq 0.19 \times c_R$. A detailed *post-mortem* analysis of the fracture surface samples reveals that this velocity corresponds exactly to the onset of the appearance of conic marks on the fracture surface (section 3.2). Such conic marks result from damage spreading through the nucleation and the growth of micro-cracks ahead of the propagating crack. The observed transition can thus be associated with this well-identified dissipating fracture mechanism. A simple model relates both the energetic and fractographic measurements (section 3.3). Consequences are subsequently discussed (section 3.4).

3.1 Fracture energy measurements: A new critical velocity

The experimental setup described in the previous chapter is used to drive dynamic cracks in PMMA. The dynamic fracture energy, Γ, is deduced directly from Eq. 3.1. Methods for acquiring input data of equation 3.1 are described in section 2.3 for the velocity and section 2.4 for the quasi-static stress intensity factor. Variations of K

and Γ as a function of the crack length c in a typical experiment are presented in Fig. 3.1.

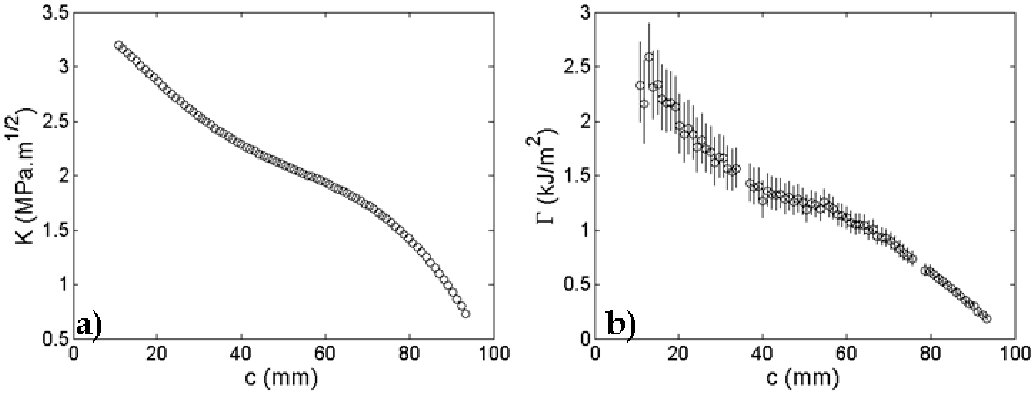

Figure 3.1: a) Quasi-static stress intensity factor $K(c)$ and b) Dynamic fracture energy $\Gamma(c)$ both as a function of the crack length c in a typical experiment.

The variation of Γ as a funtion of v is shown in Fig. 3.2. These results are the same in all our experiments and are weakly dependent on the initial stored mechanical energy, U_0 (tuned by the radius of the hole at the seed-crack, see section 2.2.2). This curve provides evidence for three regimes, separated by two critical velocities. For low crack velocities, Γ, remains on the order of $G_c = K_c^2/E \simeq 0.42 \pm 0.07 J/m^2$, where K_c refers to material toughness and G_c is the critical mechanical energy release rate. Then, as v reaches the first critical value $v_a \simeq 165$ m/s $= 0.19 \times c_R$, fracture energy increases abruptly to approximately 3 times the fracture energy at G_c. Beyond v_a, Γ increases slowly with v up to a second critical value, $v_b = 0.36 \times c_R \simeq 317$ m/s, then Γ again diverges with v. The second critical velocity corresponds to the onset of the micro-branching instability, widely discussed in the literature (see Sec. 1.4 and references [52, 28] for instance). To the very best of our knowledge, the first critical velocity $v_a \simeq 0.19 \times c_R$ is reported herein for the first time.

It is also interesting to note about the abrupt Γ increase around v_a: At this point, slight variations of crack velocity, v, seems to induce significant changes in fracture energy. This provides a direct interpretation for the repeated observation of cracks that span a wide range of fracture energies but propagate at a nearly constant velocity, approximately $0.2 \times c_R$ (see e.g. [32, 91]).

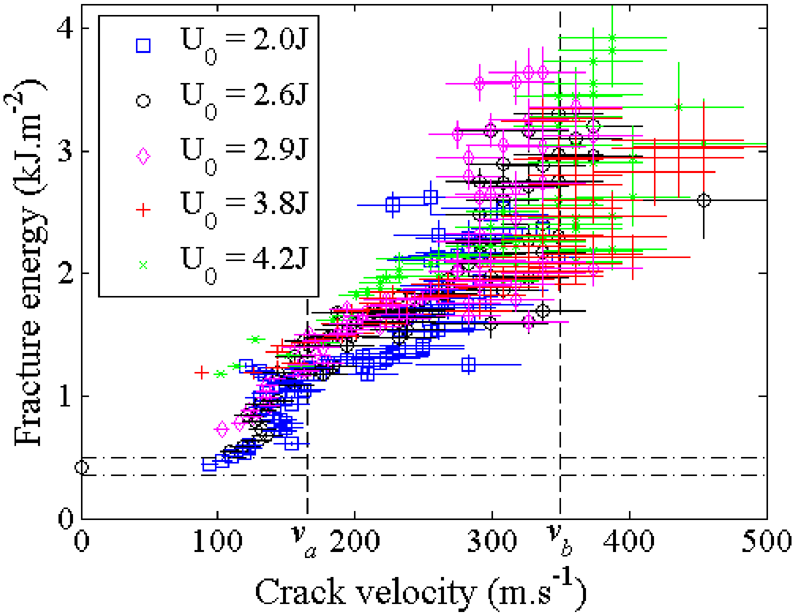

Figure 3.2: Fracture energy, Γ, vs v for various experiments with different stored mechanical energies, U_0, at crack initiation. The two vertical dashed lines correspond to $v_a = 0.19 \times c_R$ and $v_b = 0.4 \times c_R$. The two horizontal dashed lines indicate the confidence interval for the measured fracture energy, K_c^2/E, at crack initiation.

3.2 Fractographic observations

3.2.1 Appearance of conic marks beyond the new critical velocity

To shed light on the local mechanisms responsible for the transition at v_a, we looked at the morphology of the fracture surfaces. Fracture surfaces were observed with the optical microscope presented in chapter 2.5.1. Typical snapshots of *post-mortem* fracture surfaces recorded at velocities lower than v_a, between v_a and v_b, and greater than v_b are presented in Fig 3.3. The side of the specimens were also inspected (see fig. 3.4). Three cases could be distinguished:

- When $v < v_a$, fracture surfaces and specimen sides remain smooth at the optical scale.
- When $v_a < v < v_b$, conic marks can be observed on the fracture surfaces. The specimen sides remain smooth at the scale of observation. .
- When $v_b < v$, conics marks continue to be observed on the fracture surfaces. Patterns reminiscent of micro-branches [81] are also observed on the specimen sides.

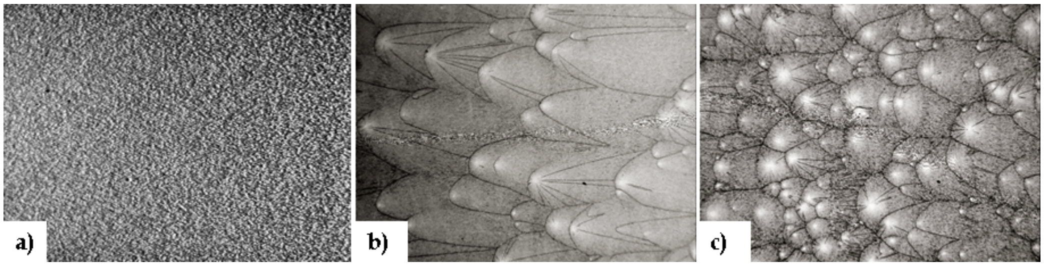

Figure 3.3: Microscope images (1.4×1 mm^2 field of view) of the fracture surfaces, taken at: (a) $v = 110 \pm 10$ m/s; (b) $v = 250 \pm 20$ m/s; (c) $v = 450 \pm 50$ m/s. Crack propagation is from left to right.

These observations confirm that the second critical velocity (v_b) observed in the $\Gamma(v)$ curve, coincides with the onset of micro-branching. They also suggests that the first critical velocity, v_a, should be associated to the onset of conic marks in the fracture surface.

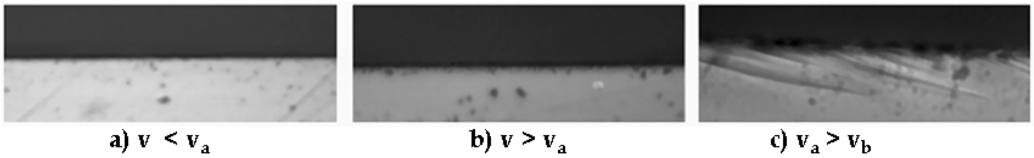

a) $v < v_a$ **b)** $v > v_a$ **c)** $v_a > v_b$

Figure 3.4: Microscope images (0.5×0.7 mm^2 field of view) of the sample side. (a) $v = 120 \pm 20$ m/s, $K^2/E = 1k$ J/m^2; (b) $v = 260 \pm 30$ m/s, $K^2/E = 2k$ J/m^2; (c) $v = 650 \pm 100$ m/s, $K^2/E = 7k$ J/m^2. Crack propagation is from left to right.

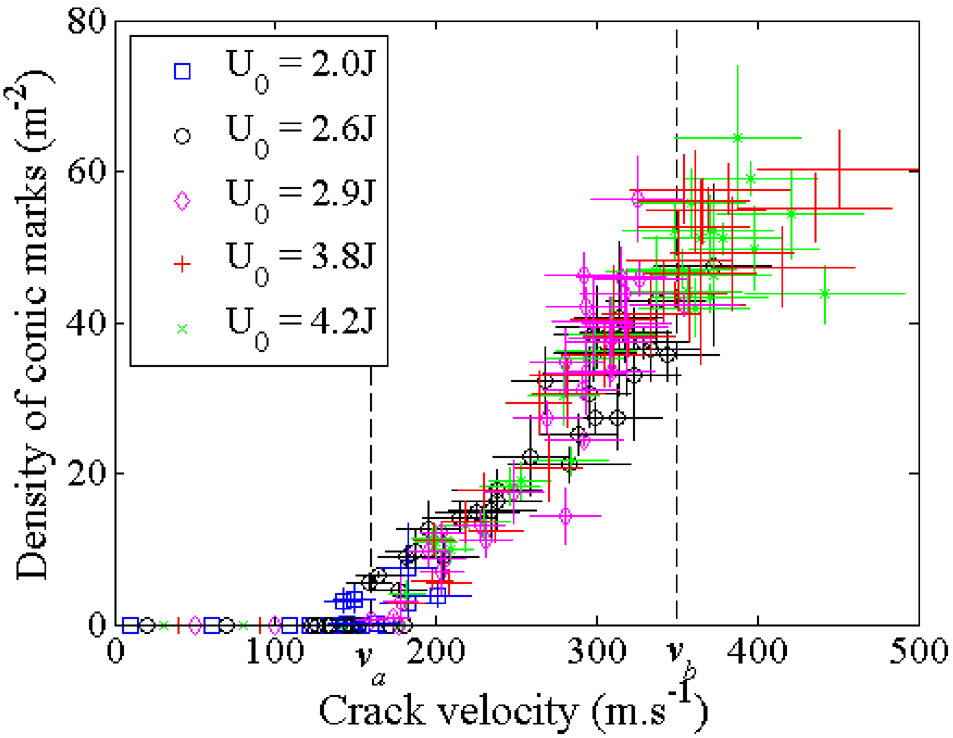

Figure 3.5: Density of conic marks, ρ, as a function of crack velocity for all our five experiments. The image were recorded at ×5 magnification (scan-size: 1.4×1 mm^2, pixel size: 677 nm). The error bars denote the standard deviation on the measurement of ρ for a fixed value of v.

The number per unit area ρ of conic marks is plotted as a function of crack velocity, v, in figure 3.5. The images used to compute this curve were taken with a ×5 magnification (scan-size: 1.4×1 mm^2, pixel size: 677 nm). The various experiments collapse fairly well onto a single master curve. Two regimes can be distinguished:

- Below the critical velocity v_a, no conic marks are observed. It is worth to emphasize that no conic marks were observed, even when one is increasing the magnification up to ×50.
- Above v_a, ρ increases almost linearly with $v - v_a$ (see figure 3.5).

The fact that conic marks become visible on fracture surfaces at the very same critical velocity v_a where Γ exhibits an abrupt increase strongly suggests that both phenomena are associated with the same transition.

3.2.2 Interpretation of the conic marks: Signature of micro-cracking.

The observation of conic marks in PMMA is not new and has been reported e.g. in [67, 92, 91, 93]. Similar conic marks were reported on the post-mortem fracture of many other amorphous brittle materials (see [9, 32] and references therein), including polystyrene [62], silica glasses [61], cellulose acetate [65], Homalite [91] and polycrystalline materials [64] (see figure 3.6).

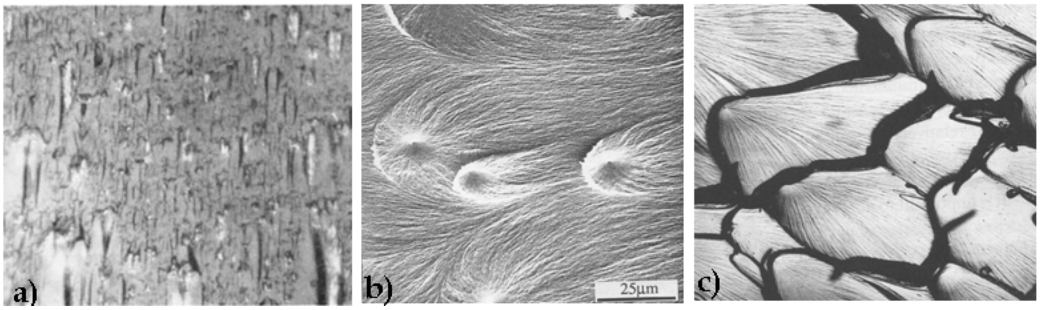

Figure 3.6: Observations of conic marks in various materials. a) glass from [70] b) polystyrene and polyurethane, from [9].

Their formation is thought to arise from inherent toughness fluctuations at the micro-structure scale due to material heterogeneities randomly distributed throughout the material [91, 61]. The enhanced stress field in the vicinity of the main crack front activates some of the low toughness zones (nucleation sites) and triggers the initiation of secondary penny-shaped micro-cracks ahead of the crack front. Each micro-crack grows radially under the stress associated with the main crack along a plane different from it. When two micro-cracks intersect in space and time, the ligament separating them breaks up, leaving a visible conic marking on the *post-mortem* fracture surface.

In this scenario, the focus of a given conic pattern corresponds to the nucleation center of the micro-crack. Furthermore the distance between the conic's focus and apex is set by the distance, d_n, between the triggering main crack front and the nucleation center at the onset of micro-cracking. In regions where micro-cracks are observed, but micro-branches are not, d_n is found to be in the range $10-100\ \mu$m, which is consistent with the above scenario for micro-cracks (see figure 3.7). A nucleation center in the material will initiate a micro-crack when it is submitted to a stress of the order of the intrinsic strength σ^* of the material ($\sigma^* \simeq 500$ MPa in PMMA [94]). Due to the square root stress singularity at the crack tip, the stress level at a distance d_n from the main crack front is $\simeq K/\sqrt{d_n}$. Hence we recover the observed range $d_n \simeq (K/\sigma^*)^2 \simeq 10 - 60\ \mu$m for K in the range $2 - 4$ MPa explored in the experiments (see e.g. figure 3.7).

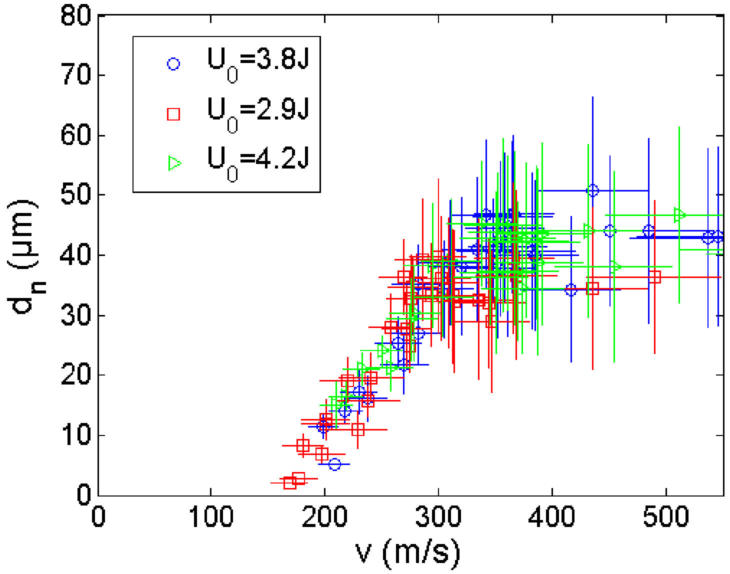

Figure 3.7: Nucleation distance, d_n, as a function of the crack velocity for various fracture experiments. The error-bars denote the standard deviation on the measurement of d_n for a fixed value of v.

3.3 Macroscopic scenario: damage spreading and energy dissipation

We turn now to the interpretation of the variations in the fracture energy, Γ, as a function of the crack velocity, v. In this respect, it is interesting to plot Γ as a function of the dynamic stress intensity factor, $K_d(v)$. This quantity can be related to the static stress intensity factor, K, through this approximation: $K_d(v) = k(v)K$ where $k(v) \simeq (1 - v/c_R)/\sqrt{1 - v/c_D}$ (see section 1.2.1). This curve is plotted in Fig. 3.8.

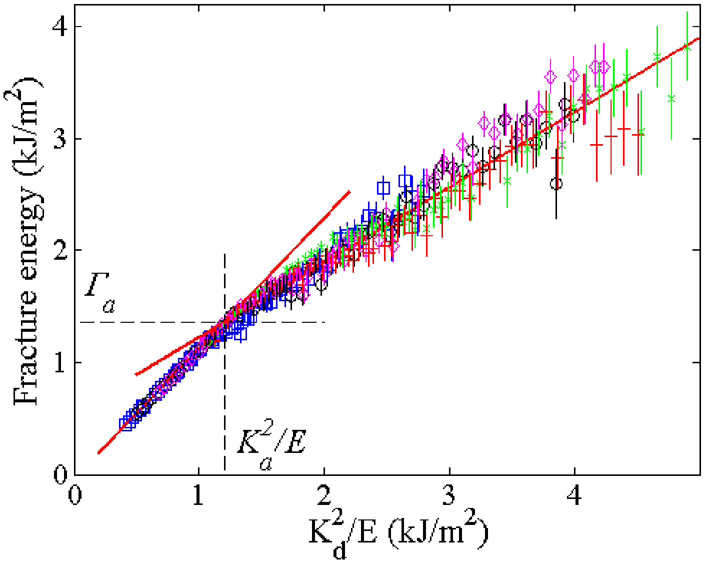

Figure 3.8: Variation of Γ as a function of K_d^2/E. The value K_a corresponds to the value of $K_d(v = v_a)$ at the microcracking onset. The red lines are linear fits using Eqs. 3.4 and 3.8, respectively.

Below the microcracking onset (i.e. for $K_d(v) \leq K_a$) Γ is found to vary linearly with $K_d(v)^2$ (Fig. 3.8). This scaling is to compare to that of the size $R_c(v)$ of the fracture process zone [10]):

$$R_c = \left(\frac{K_d(v)}{a\sigma_Y}\right)^2 \tag{3.2}$$

where σ_Y refers to the yield stress and a is a dimensionless constant which depends on the precise model. In other words, the fact that Γ is proportional to K_d indicates that Γ is proportional to R_c. Hence that the volume dissipation energy, ϵ, within the fracture process zone is constant. Indeed, the volume scanned by the fracture process zone when the crack propagates over an increment δc is $R_c H \delta c$ where H refers to the specimen thickness. The dissipated energy, $\Gamma H \delta c$, is then given by $\gamma_s H \delta c + \epsilon R_c(v) H \delta c$ where γ_s is the standard "Griffith" surface energy. Hence:

$$\Gamma = \gamma_s + \epsilon R_c(v) \tag{3.3}$$

Furthermore, since $\Gamma(v=0) = K_c^2/E$, one finally gets before the microcracking onset (i.e. for $v \leq v_a$). This is a postulate:

$$\Gamma(v) = \alpha \frac{K_d(v)^2}{E} + (1-\alpha)\frac{K_c^2}{E} \quad \text{with} \quad \alpha = \frac{\epsilon E}{a\sigma_Y^2} \tag{3.4}$$

A linear fit to the data gives $\alpha = 1.17 \pm 0.05$ and $K_c^2/E = 0.3 \pm 0.2$ kJ.m^{-2} (see Fig. 3.8). The latter value is compatible with the measurements of the fracture energy at crack initiation.

By combining this last equation with the motion equation (Eq. 3.1), one can express Γ as a function of v:

$$\Gamma(v) = \frac{1-\alpha}{1-\alpha\frac{1-v/c_R}{1-v/c_D}}\frac{K_c^2}{E} \tag{3.5}$$

This reproduces very well the regime below the microcracking onset, $v \leq v_a$ (Fig. 3.9). This expression for Γ exhibits a divergence of the dissipated energy for a finite velocity v_a' given by:

$$v_a' = (\alpha-1)c_R c_D/(\alpha c_D - c_R) \simeq 200 \text{ m.s}^{-1} \simeq 0.23 c_R \tag{3.6}$$

This value is slightly larger than v_a. In the absence of micro-cracks, this velocity v_a' would have set the limiting macroscopic crack velocity.

Let us now turn to the dissipation mechanism above the microcracking onset, i.e. for $v \geq v_a$. The existence of a threshold for microcracking appears surprising as it cannot be accounted for in just a stress-driven nucleation mechanism. We believe that

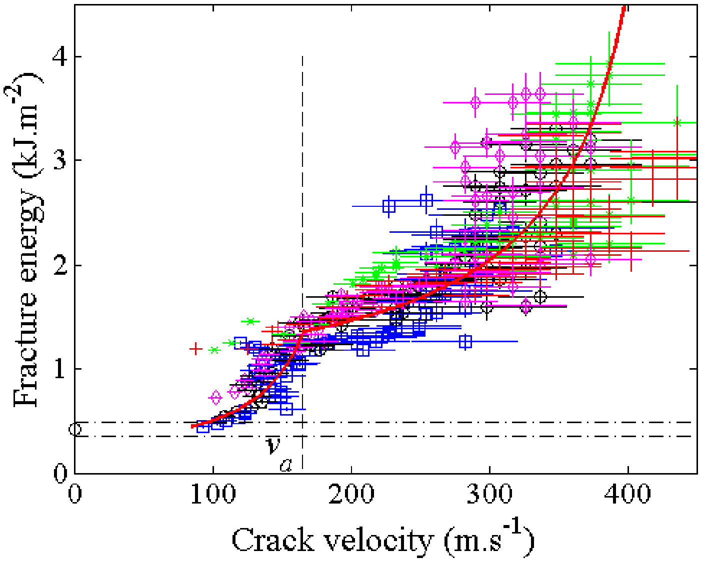

Figure 3.9: Variation of fracture energy, Γ, as a function of the crack velocity, v. Comparison between theory and experiments. The red lines corresponds to Eq. 3.5 below v_a, and Eq. 3.9 above v_a.

the conic marks observed here at the optical scale coincide with microcracks that had time to develop. In standard interpretation [91, 61], the conic eccentricity is given by the ratio between the velocity of the nucleated micro-crack and that of the main crack front. When the microcrack goes slower than the main crack, one expects to observe an ellipse. Hence, the FPZ size should permit the nucleation of micro-cracks at distances far enough from the main crack so that the micro-crack has enough time to reach a sufficient velocity and leave a conic mark visible at the optical scale. In this scenario, one expects to observe elliptic marks at sub-micrometric scales, even for $v \leq v_a$.

To interpret the curve $\Gamma(v)$ within the micro-cracking regime, i.e. for $v_a \leq v$, we invoke the existence of an excluded volume, V, around each micro-crack where stresses are screened and therefore, no further dissipation can occur. As before, it is interesting to plot the surface density of conic marks ρ as a function of K_d (Fig. 3.10). Note that in the micro-cracking regime, the local dynamic stress intensity factor, K_d, is not equal to the macroscopic one anymore, but corresponds to that at the individual micro-crack tips. This local K_d is then estimated by setting the local velocity to v_a and using the quasi-static K at the length c in Eq. 1.20. Each micro-crack can be

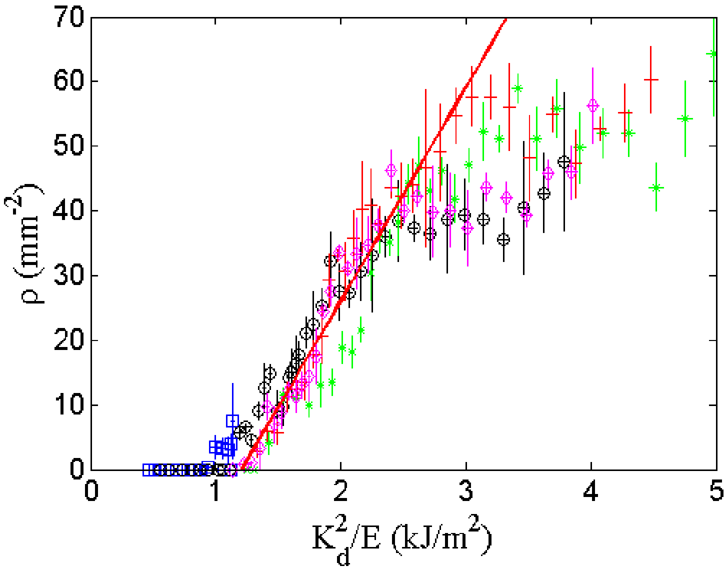

Figure 3.10: Variation of ρ as a function of K_d^2/E. The red line is a linear fit and corresponds to Eq. 3.7.

considered locally as a single crack, the limiting velocity of which has been shown to be $v'_a \gtrsim v_a$. Above v_a, it is natural to assume that all micro-cracks propagate at the same velocity, v_a. Hence, in the micro-cracking regime, $K_d(v) = k(v'_a)K$. Between K_a and K_b, the values of K_d at v_a and v_b respectively, ρ scales as:

$$\rho = \alpha \frac{K_d(v)^2 - K_a^2}{E} \tag{3.7}$$

where a fit to the data gives α =33±3 kJ^{-1}. This square dependency indicates that the number of conic marks is proportional to the FPZ size and suggests that the density of nucleation sites for micro-cracks is constant within the material. In the micro-cracking regime, the energy $\Gamma(v)H\delta c$ dissipated when the crack length increases by δc is $\gamma H\delta c + \epsilon(R_c(v)H\delta c - \rho(v)H\delta cV)$, yielding:

$$\Gamma(v) = \Gamma_a + \chi \frac{K_d(v)^2 - K_a^2}{E} \quad \text{with} \quad \chi = \alpha - \epsilon\beta V \tag{3.8}$$

where Γ_a is the fracture energy obtained at $v = v_a$ using Eq. 3.5. Equation (3.8) predicts a linear dependence of Γ with $K_d(c, v)^2/E$, which is in agreement with the measurements for $K_d^2/E > K_a^2/E$ (Fig. 3.11). A linear fit to the data gives χ=0.67±0.01.

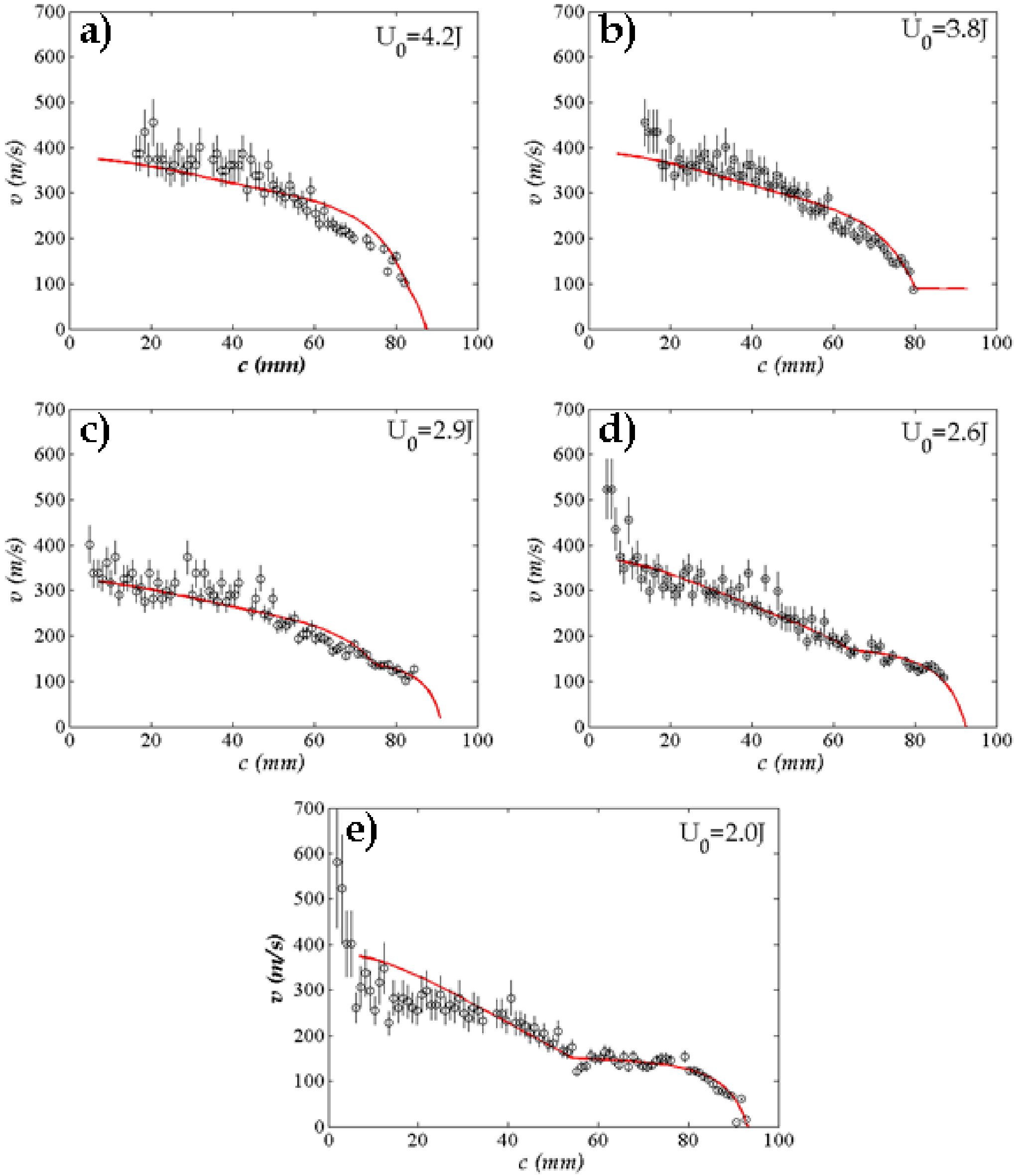

Figure 3.11: Velocity profiles measured experimentally in each of the five performed experiments (points) and predicted theoretically assuming that the fracture energy is given by Eq. 3.5 below v_a, and Eq. 3.9 above v_a.

As before, this last equation can be combined with the motion equation (Eq. 3.1) to express Γ as a function of v:

$$\Gamma(v) = \frac{1 - v/c_R}{1 - k(v_a)^2\chi - v/c_R}\left(\Gamma_a - \chi\frac{K_a^2}{E}\right) \tag{3.9}$$

The corresponding predicted $\Gamma(v)$ reproduces very well the high velocity regime $v \geq v_a$ (Fig. 3.9) and exhibits a divergence of the dissipated energy for v_∞ given by:

$$v_\infty = c_R(1 - \chi k(v_a')^2) \simeq 450 \text{ m.s}^{-1} \simeq 0.52 c_R \tag{3.10}$$

This limiting velocity is very close to the observed maximum crack speed in brittle amorphous materials.

One can finally use the fracture energy variation as a function of velocity (given by Eqs 3.5 and 3.9) and combine it with the finite element estimation of the the profiles $K(c)$ to predict the velocity profiles in the various experiments performed herein. The comparisons between these predictions and the measurements are provided in Fig. 3.11. The agreement is fairly good.

3.4 Conclusion

In this chapter, we have investigated dynamic fracture experiments in Plexiglas (the archetype of brittle amorphous material). The fracture energy was found to exhibit an abrupt change at a well-defined critical velocity, v_a $0.19 \times c_R$, well before the micro-branching instability onset [81]. The nature of the transition was uncovered through fractographic observations. Above v_a, damage spreading through the nucleation and growth of micro-cracks occurs and yields conics patterns visible on the post-mortem fracture surfaces.

A simple scenario has been proposed and succeeds to capture the form taken by the fracture energy below and above v_a. This scenario is based on the fact that energy dissipated per unit volume within the process zone is constant and the existence of a volume around the nucleated micro-cracks where stresses are screened and hence no dissipation occurs. This has allowed a fit of the variation fracture energy with respect to the crack velocity. This fit along with the equation of motion has allowed us to reproduce all the experimental profiles measured. It should be noted that our experiments were performed with decelerating crack propagation. Il will be interesting if this transition still exists with accelerating cracks.

The evidence of such a nominally brittle to quasi-brittle transition in dynamic fracture provides a rigorous energetical definition of the "mirror-mist" transition empirically defined in fractography [9]. This definition completes the observation carried out by Sharon et al [28, 81] which associates the microbranching onset to the hackle transition.

In the next chapter we will investigate in greater detail the damage spreading within the process zone and characterize it to mechanisms at the microscale.

Chapter 4

Microscopic study: deterministic reconstruction and statistical analysis.

In the preceding chapter, we have investigated dynamic crack propagation in PMMA. The fracture energy, Γ, was measured as a function of the crack velocity, v, (Fig. 3.2). This curve exhibits an abrupt 3-folds increase at a well-defined velocity, $v_a \simeq 165$ m/s $\simeq 0.19 \times c_R$, which is significantly less than the microbranching onset, $v_b \simeq 317$ m/s $\simeq 0.35 \times c_R$. Fractography observations revealed three regions (Fig. 3.5):

- When $v < v_a$, the *post mortem* observations show smooth fracture surfaces and specimen sides at the optical scale.
- When $v_a < v < v_b$, one observes conic markings on the fracture surfaces the density of which increases linearly with v. The specimen sides remain smooth.
- When $v > v_b$, micro-branches are observed on the specimen sides. Also conic marks continue to be observed on the fracture surfaces.

These conic marks are thought to be the signature of damage spreading through microcracking ahead of the main crack. From these experimental observations, we proposed a scenario which allows us to relate Γ variations to v and subsequently to the conic marks density assuming: (i) a constant volume energy dissipation within the process zone and (ii) stress screening around the nucleated micro-cracks for $v \geq v_a$. This scenario predicts that the crack velocity diverges at a value $v_\infty \simeq 0.52 \times c_R$, in good agreement with experiments reported in the literature.

In this chapter, we examine the damage spreading ahead of the crack front *at the microscopic scale*. In section 4.1, we will see how one can reconstruct the dynamics of crack propagation and that of microcrack nucleation from the conic patterns observed on *post-mortem* fracture surfaces. The statistics of damage spreading at the micro-scale will be characterized in section 4.2. Finally, in section 4.3, we will see how one can estimate the size of the process zone using this reconstruction.

4.1 Reconstruction of dynamic crack propagation at the microscopic scale.

4.1.1 Assumptions of the model

A simple geometrical model was suggested in the literature [91, 61, 66] to explain the geometry of the conic marks.

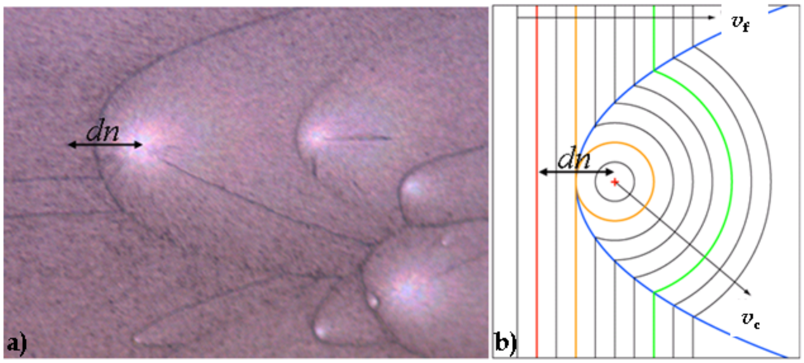

Figure 4.1: a) Microscope image ($\times 10, 0.5 \times 0.7 mm^2$) showing conic marks on the fracture surfaces of PMMA. The quantity d_n denotes the critical distance from which conic marks start to nucleate. This distance is twice the distance between the conics focus and apex. b) Schematic representation of the formation of conic marks due to the interaction between the main crack front, growing at a velocity v_f, and the nucleated microcrack that grows ahead of the main crack front with a velocity v_c.

The idea is to consider a crack front that propagates along a given plane with a velocity v_f. During its propagation, it can encounter inhomogeneities. As the crack front approaches a critical distance, d_n, from one of these inhomogeneities, a secondary micro-crack nucleates at the inhomogeneity. This secondary microcrack grows radially, as a penny shape crack, with a velocity v_c along a plane parallel but at a different height from the primary crack front. The intersection between the main crack front and the secondary microcrack leaves a visible trace (marked by a height difference) on the fracture surfaces. Assuming that both velocities v_f and v_c are equal, this trace takes the form of a conic. The focus of conics coincides with the location of the initial inhomogeneity, and the eccentricity of which depends on d_n (see Figure 4.1). The nucleation distance, d_n, is twice the distance between the conic focus and the conic apex.

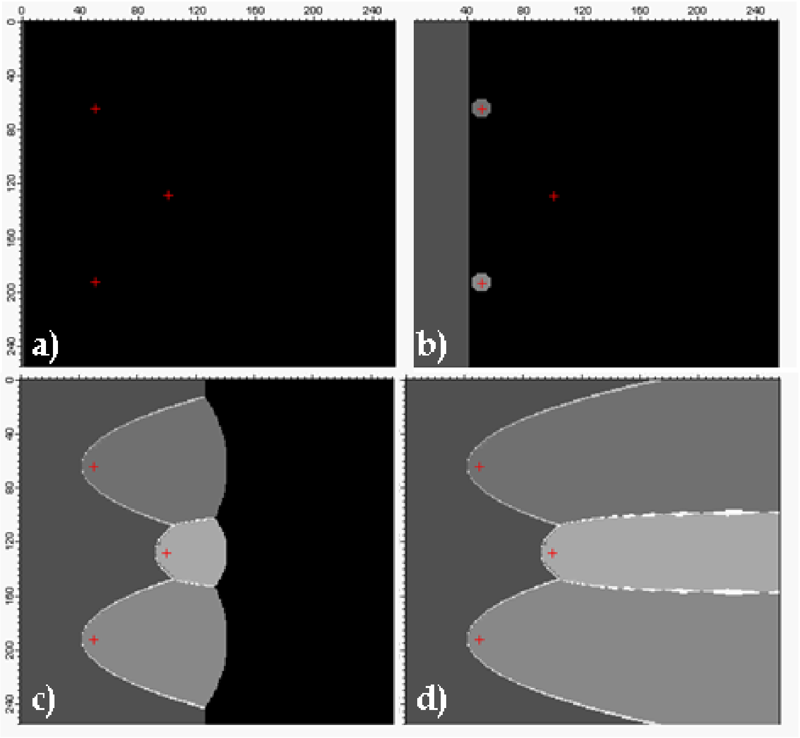

Figure 4.2: Snapshots of the conic marks simulation. a) Snapshot taken before the linear crack front starts to propagate. The three red + represent the nucleation centers of the conic markings. b) When the main crack front is at the critical distance d_n from the nucleation sites, those open and start to grow radially. c) and d) Trace left from the interactions between the main crack front and the growing micro-cracks. This trace is expected to be the one observed on the fracture surface.

In this scenario, the next step consists in developing a model and making a crack front propagate and interact with several inhomogeneities. Figure 4.2a, depicts a model system consisting of three nucleation sites (red crosses) of secondary microcracks placed randomly. Then, a planar primary crack front was propagated from left to right as is shown in Fig. 4.2b. At a given critical distance, d_n, between the nucleation sites and the primary crack front, the secondary microcracks start to grow radially. This scenario can be observed in Fig. 4.2b. The intersections between the penny-shape microcracks and the primary crack front leave conics (Fig 4.2c and d) similar to what is observed on real fracture surfaces. The origin of the color scale in fig. 4.2c and d is the following: When a microcrack is nucleated, the code attributes to it a specific number. When a pixel of the image is reached by a propagating microcrack, its value is switched to the one of this microcrack. Thus, all the pixels activated by the same microcrack share a unique value yielding a zone of given color in the final image. When a pixel is activated *simultaneously* (at the same time step) by two microcracks, it receives a value equal to the sum of the two microcracks. Then, the intersections become visible as the color scale correspond to the value of each pixel.

4.1.2 Reconstruction algorithm

Now we are able to simulate the formation of surface markings from the knowledge of two parameters, namely the position of nucleation sites and the critical nucleation distance d_n. Let us turn our attention to how this compares to the fracture surfaces obtained in the various experiments presented in the preceding chapter. Several areas of the fracture surfaces were observed. For each of them, nine optical profilometer images (see section 2.5.2) were recorded. These images were chosen so that they overlap partially and can then be gathered into a single large image (this ensures adequate statistics in the following analyses). The areas of analyses were chosen at various velocities above the microcracking onset v_a, ranging from 200 m/s to 450 m/s with increments of 50 m/s. The methodology to extract the data is the following: We record the coordinates x, y and z of the focus for each surface conics. Then, we estimate the nucleation distance, d_n, by "guessing", for each conics, what was the primary microcrack (mother microcrack) the progression of which triggers the nucleation of the considered conics (family criterion). The apex of the considered conics is then defined as the intersection between the segment linking the mother focus to the considered focus and the conic marks (see Fig. 4.3). The distance, d_n, is then defined as twice the distance from the apex to the focus. This procedure is used to compute d_n for each mark of the image.

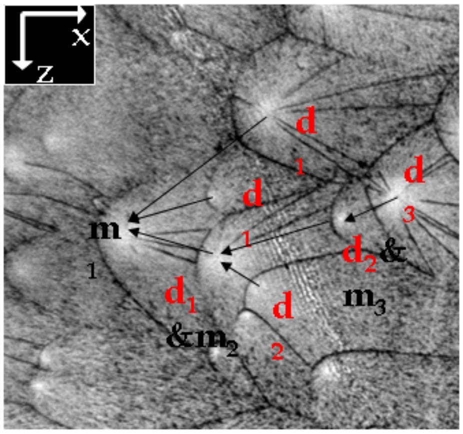

Figure 4.3: Sketch showing the algorithm used to compute the focus and apex of each conics visible on profilometer images.

To perform the reconstruction, we first mark all the nucleation sites (focus) with the coordinates computed from the profilometer images. Secondly a crack front is made to propagate from left to right, at a velocity of 1pixel/timestep. Once the distance between the secondary microcrack nucleation site and the primary crack front reaches d_n (computed from the experimental images), the secondary microcrack grows radially at the same velocity (1pixel/timestep). This assumption of a constant velocity for all (micro-)crack fronts is justified from the discussion in section 3.3 which suggests that at the microscopic scale, the front velocity saturates to a limit velocity v_a' slightly larger than v_a. After each reconstruction, we superpose the profilometer image to the reconstructed one (see images of Fig. 4.5c) to ensure that the data chosen as inputs for the reconstruction were correct. When this is not the case, we modify the family scheme accordingly and repeat the process. This procedure is performed till we get a good superposition between the experimental and the reconstructed images.

Figures 4.4 show some snapshots of the reconstruction at two different velocities. Images on the left side (marked with the letter a) corresponds to a velocity of 250 m/s, and the images on the right side (marked with the letter b) are the snapshots of the reconstruction for a crack with a velocity 450 m/s. Interesting information is observed in these reconstructions. First, one can appreciate that the main crack front is no longer straight, but wiggly (see 4.4 from up to down) even if the initial front is assumed to be straight. For $v = 250$ m/s, the snapshots also show that microcracks nucleate one after the other, each of them coalescing with the main front before the nucleation

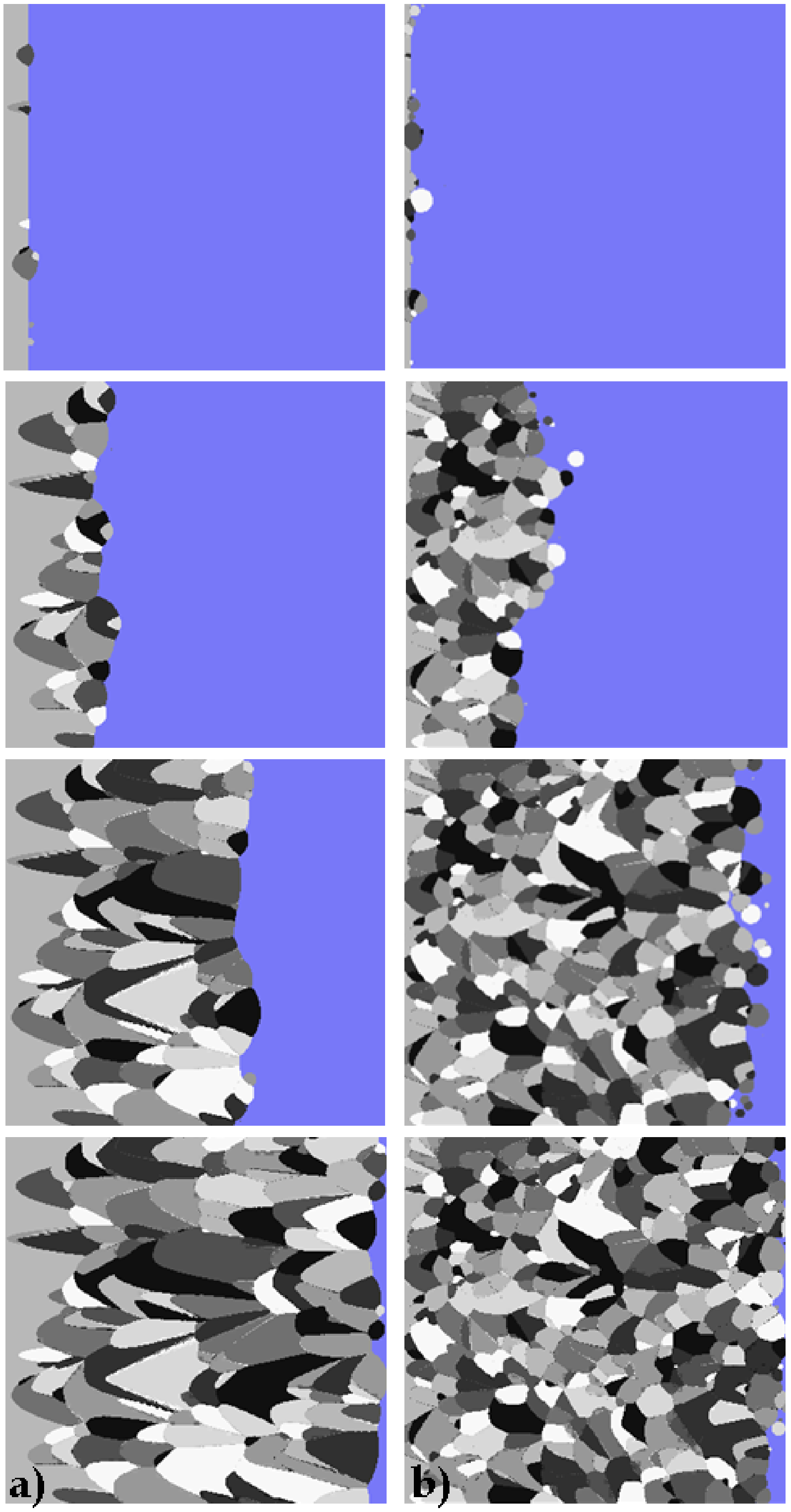

Figure 4.4: Successive snapshots of the crack front propagation and the microcrack nucleation as observed from the reconstructions. The crack propagates from left to right. a) 250 m/s and b) 450 m/s. The data for this reconstruction is taken from optical profilometer images of ×5 resolution, size of 2.5×2.5 mm^2 and 3.5×2.5 mm^2, respectively.

of the following one. At this velocity, the density of conic marks is $\rho \simeq 26$ mm^{-2}, and the conics present a hyperbolic shape of large size. On the other hand, at $v = 450$ m/s, the crack front sees an ensemble of microcracks ahead of it. In this case the density of the surface markings increases to $\rho \simeq 62$ mm^{-2}, more than twice the value observed at 250 m/s. At this velocity, the conic marks change in shape and do not resemble hyperbolas any more. These complex forms result in the coalescence of several microcracks, before they merged with the main front.

Figure 4.5 compares the reconstructions to the experimental surfaces for the various velocities. The profilometer images are on the left, the reconstructed ones are in the center, and the comparison between the two are on the right. These pictures allow us to appreciate the evolution of conic marks as a function of the crack velocity. First of all, we confirm with these results that the conics density increases with v, as was previously presented in Fig.3.5. The conics change also in shape with velocity. At low velocities, they look like hyperbolas. In this velocity range, they result, almost every time, from the interaction between the main crack front and the nucleation of a single microcrack. At higher velocity, they present more complex shapes. This comes from the fact that a single conic mark can be the result of the merging of several microcracks. One can also appreciate the good agreement between our reconstructions and the experimental observations. It is interesting to note at this point, that two quantities only are introduced in these reconstruction, namely the position of nucleation sites and the nucleation distances. In particular, no information about the conic orientation is needed to obtain such a good reconstruction.

Finally, snapshots of the dynamic crack front at the various velocities are shown in Fig. 4.6. In these images, the velocity of both the main crack front and the nucleated microcracks was set to 1 pixel/time-step. The time interval between two successive snapshots is 100 time-steps. The final ”tortuosity” of the front is observed to increase with the velocity. The number of simultaneously nucleated microcracks is also observed to increase with velocity. This last observation confirms earlier observations [15, 59, 60, 32]: as the crack velocity increases, the main crack front splits into an ensemble of secondary microcracks.

Smekal's geometry model [61] has allowed us to reconstruct the dynamics of the crack front and the associated damage spreading from the patterns observed on the post-mortem PMMA fracture surfaces. It is interesting to note that the resolution of these reconstructions are set by the spatial resolution of the images of the fracture

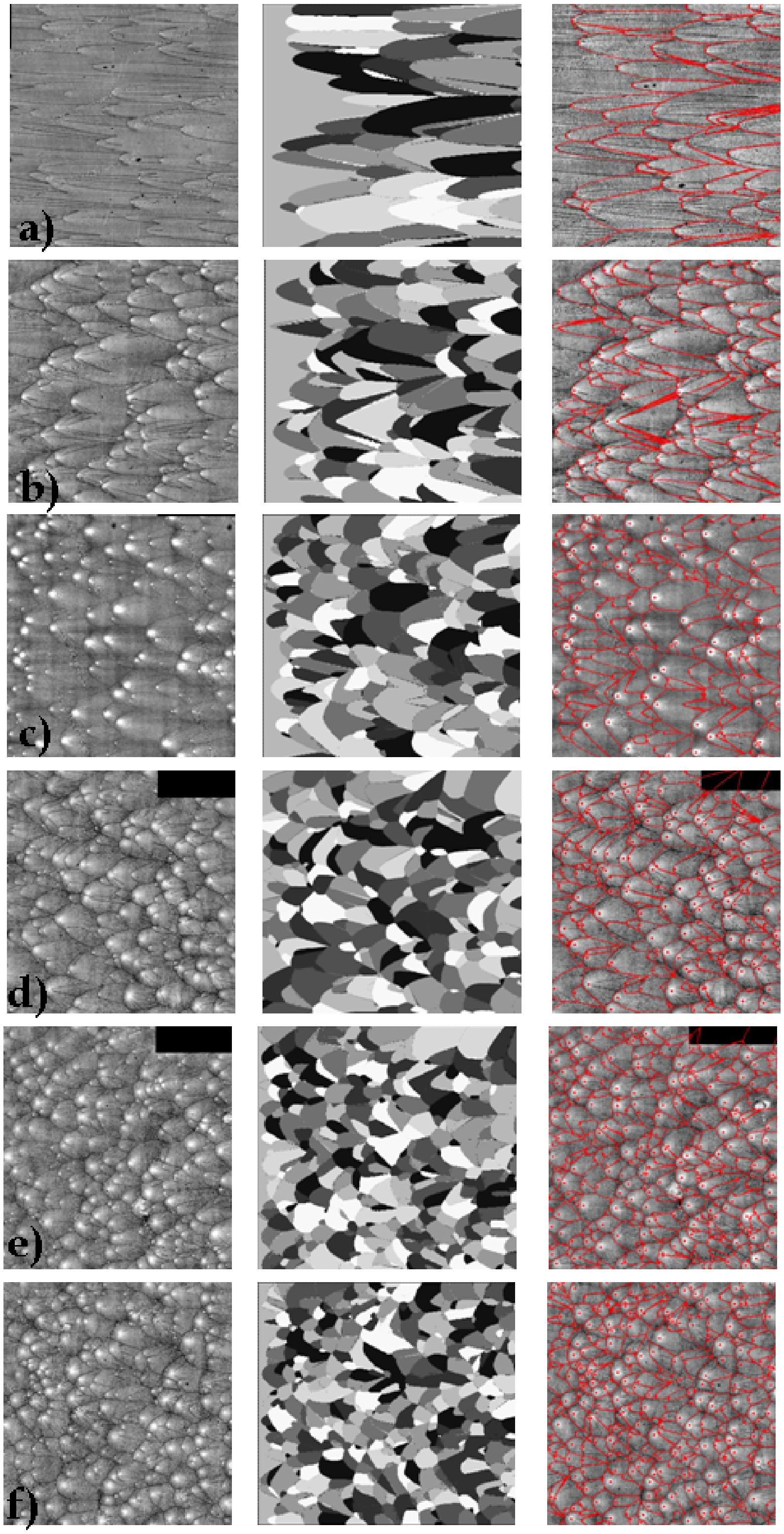

Figure 4.5: Left side: Optical profilometer images taken from the fracture surfaces at velocities of a) 200 m/s, b) 250 m/s, c) 300 m/s, d) 350 m/s, e) 400 m/s and f) 450 m/s. Center: final image reconstruction of surface markings. Right: Superposition of the optical profilometer images vs. the reconstructions (red lines) for each given velocity.

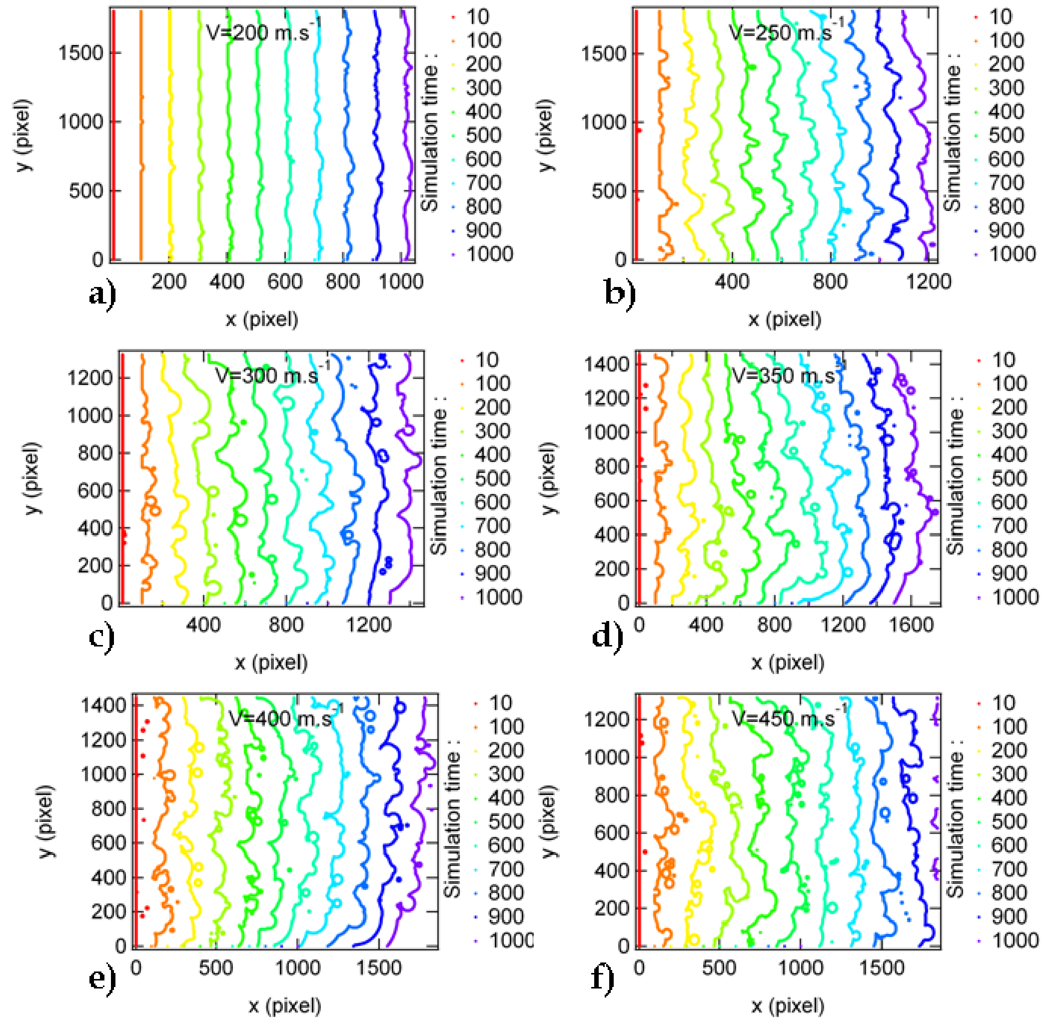

Figure 4.6: Successive snapshots of the crack front at velocities of a) 200 m/s, b) 250 m/s, c) 300 m/s, d) 350 m/s, e) 400 m/s and f) 450 m/s. The velocity of both the main crack front and the nucleated microcracks is set to 1 pixel/time-step. The time interval between two successive snapshots is 100 time-steps.

surfaces, $\simeq 1\ \mu$m.

4.1.3 Statistical analyses of nucleation distances and positions.

The reconstruction algorithm presented before needs the knowledge of two quantities: the position of nucleation sites and the associated nucleation distance, d_n. It is then interesting to characterize their statistics.

To characterize the local density of nucleation sites, Vorono tessellation was carried out. This analysis consists in computing, for each nucleation site (Fig. 4.7a), the associated Vorono polygon (Fig. 4.7b) defined as the polygon that embeds all the points of the area of interest closer to the considered site than to any other. This technic allows us to define a density measure at the smallest accessible scale, that is a single conic mark. The local density,ρ, can then be defined at the microscopic scale as $\rho = 1/A$ where A is the area of the polygon.

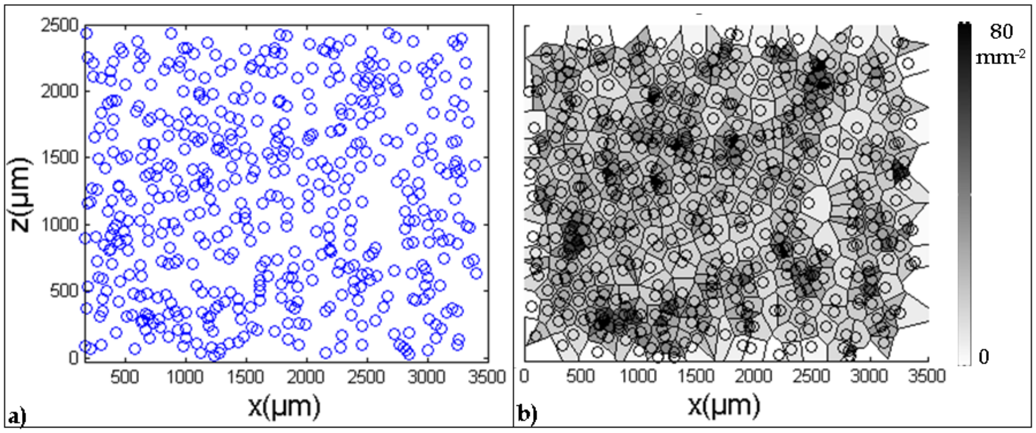

Figure 4.7: a) Position of the nucleation sites computed from one of the profilometer images (250 m/s). b) Associated Vorono tessellation. The color-scale of each Vorono polygon encodes the density according to the color-bar on the right.

The probability distribution function of the local density $P(\rho)$ was computed and plotted in Fig. 4.8 (left column). Note that the lack of statistics (300 conics per image) makes the estimation of P not very reliable. In this respect, we computed the cumulative distribution function $P_>(\rho) = \int_\rho^\infty P(x)dx$ as well (Fig. 4.8, right column). The density distribution is found to be fairly well described by a Gamma function:

$$P(\rho) = \rho^{k-1}\frac{\exp\left(\frac{-\rho}{\theta}\right)^k}{\theta^k\Gamma(k)} \tag{4.1}$$

where $\Gamma(k)$ is the Euler function. This probability function is characterized by two parameters: a scale parameter (k) and a shape parameter (θ). The variation of these parameters as a function of crack velocity is plotted in fig. 4.9. Within the errorbars, the scale parameter is found to be roughly constant. On the other hand, θ increases with v.

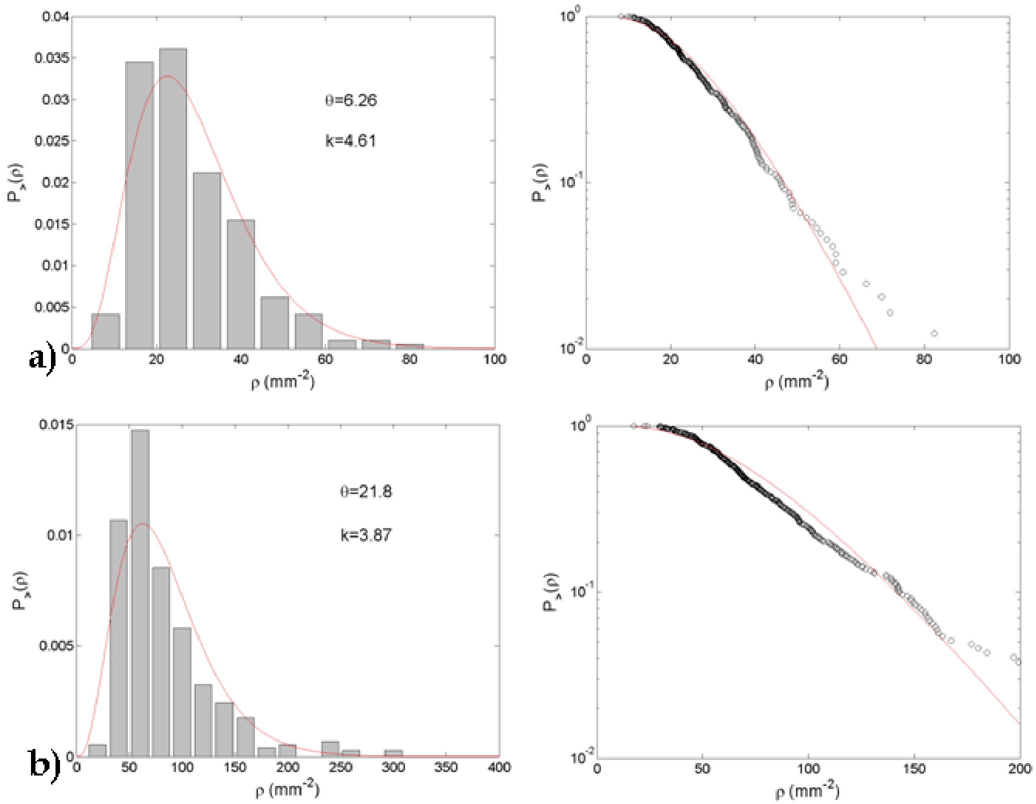

Figure 4.8: Statistical analyses of the local density as computed from Vorono analysis. Left column: probability distribution function. Right column: cumulative distribution function. a) $v = 250$ m/s and b) $v = 450$ m/s.

Finally, we characterized the statistics of the nucleation distance d_n. Figure 4.10 shows the probability distribution function and the cumulative distribution function for two velocities, namely $v = 250$ m/s and $v = 450$ m/s. Up to now, we have not found a fitting function for these distributions.

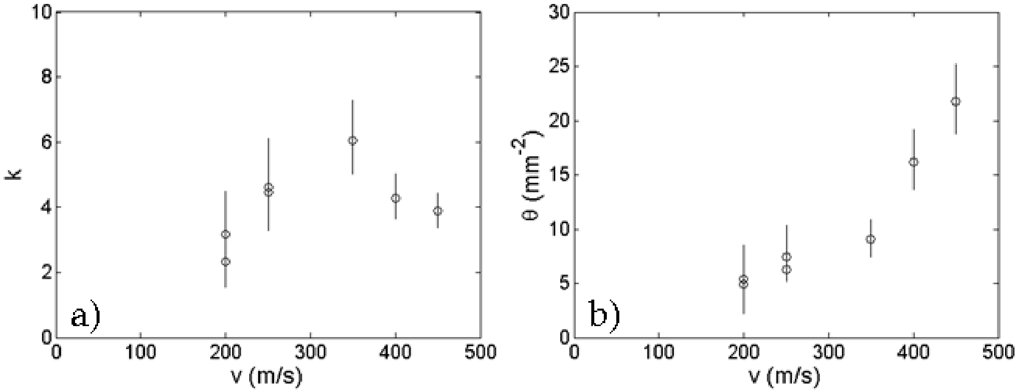

Figure 4.9: Statistic parameters k and θ which characterize the Gamma distribution of the local density of nucleation sites are plotted against crack velocity v. The error bars correspond to a 95% confidence interval.

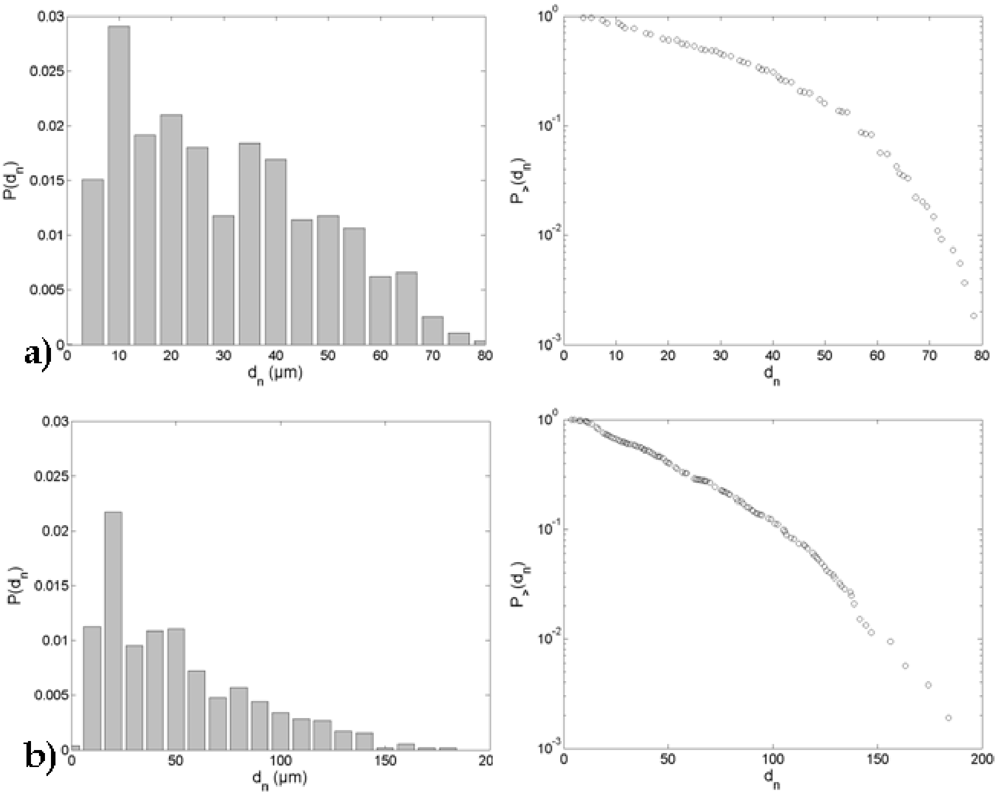

Figure 4.10: Statistical analyses of the nucleation distance. Left column: probability distribution function. Right column: cumulative distribution function. a) $v = 250$ m/s and b) $v = 450$ m/s.

4.2 Statistical analyses of damage at microscopic scale.

The reconstruction presented in section 4.1 allows us to probe damage spreading ahead of the crack front at the microscopic scale. It is then interesting to characterize the statistics of microcrack nucleation.

4.2.1 Time interval between the nucleation of two successive microcracks

In a first step, we analyse the waiting time Δt between two successive nucleation events.

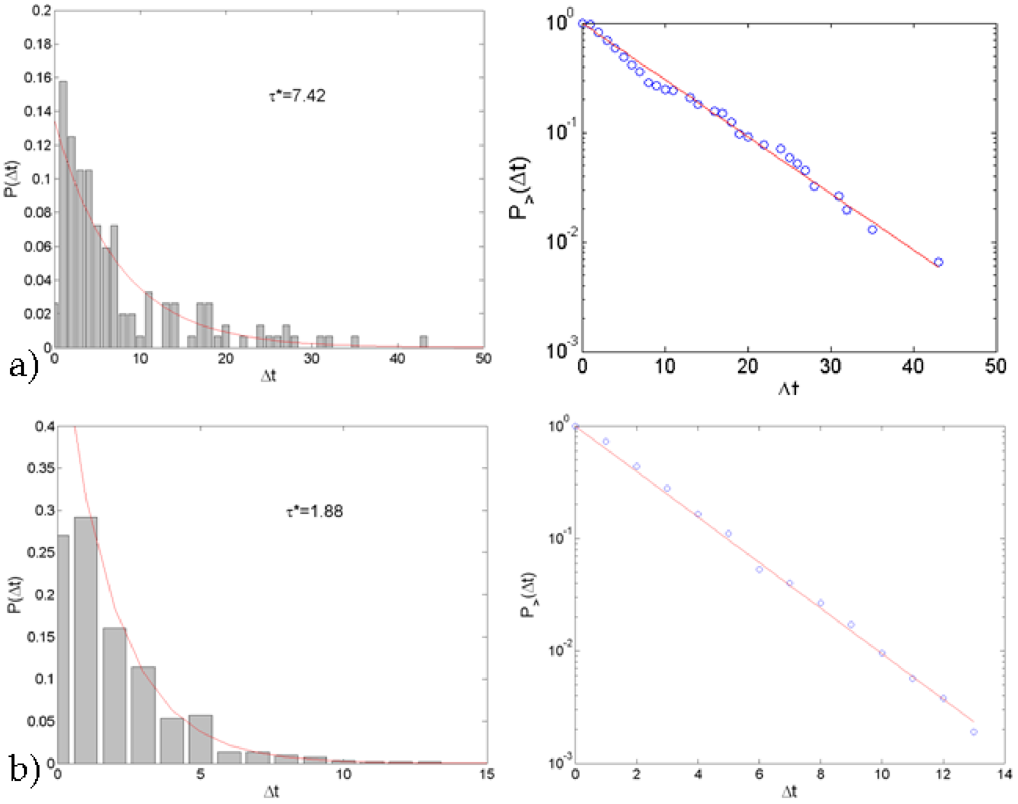

Figure 4.11: Statistical analyses of the interval time of nucleation between two successive microcracks. Left column: probability distribution function. Right column: cumulative distribution function. a) $v = 200$ m/s and b) $v = 450$ m/s.

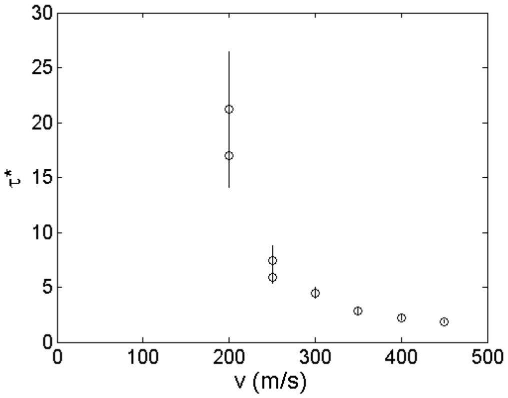

Figure 4.12: Evolution of τ that characterizes the exponential distribution of waiting time between two successive nucleation events as a function of the crack velocity v. The error bars correspond to a 95% confidence interval.

The probability and cumulative distribution functions are plotted in Fig. 4.11 for velocities of 200 m/s and 450 m/s. For all velocities ranging from 200 m/s to 450 m/s, one observes exponential distributions:

$$P(\Delta t) = \frac{1}{\tau^*}\ exp\left[\frac{-\Delta t}{\tau^*}\right] \quad P_>(\Delta t) = \ exp\left[\frac{-\Delta t}{\tau^*}\right] \tag{4.2}$$

where the parameter τ diverges as the velocity decrease down to the microcracking onset v_a (Fig. 4.12). The observation of such an exponential distribution between two successive nucleation events indicates that there is no correlation between two successive events.

4.2.2 Time interval between the nucleation of a microcrack and its daughter

In a second step, we looked at the time interval Δt between the nucleation of a primary microcrack (mother) and that of a secondary one triggered by this primary one (daughter). The probability and cumulative distribution functions are plotted in Fig. 4.13 for 200 m/s and 450 m/s. The resulting distribution is well approximated by a Weibull distribution:

$$P(\Delta t) = \frac{k}{\tau^*}\left(\frac{\Delta t}{\tau^*}\right)^{k-1}\exp\left[\frac{-\Delta t}{\tau^*}\right]^k, \quad P_>(\Delta t) = 1 - \exp\left[\frac{-\Delta t}{\tau^*}\right]^k \tag{4.3}$$

This kind of distribution is characterized by two parameters, a shape parameter (k) and a scale parameter (τ^*). Their evolution as a function of the crack velocity is plotted in Fig. 4.14. It is interesting to note that the shape parameter is constant, $k \simeq 1.4$. On the other hand, the scale parameter diverge when v decreases to the microcracking onset v_a. Such Weibull distribution is often observed when one looks at the strength distribution in heterogeneous materials. The origin of such a distribution in the present case is presently not understood.

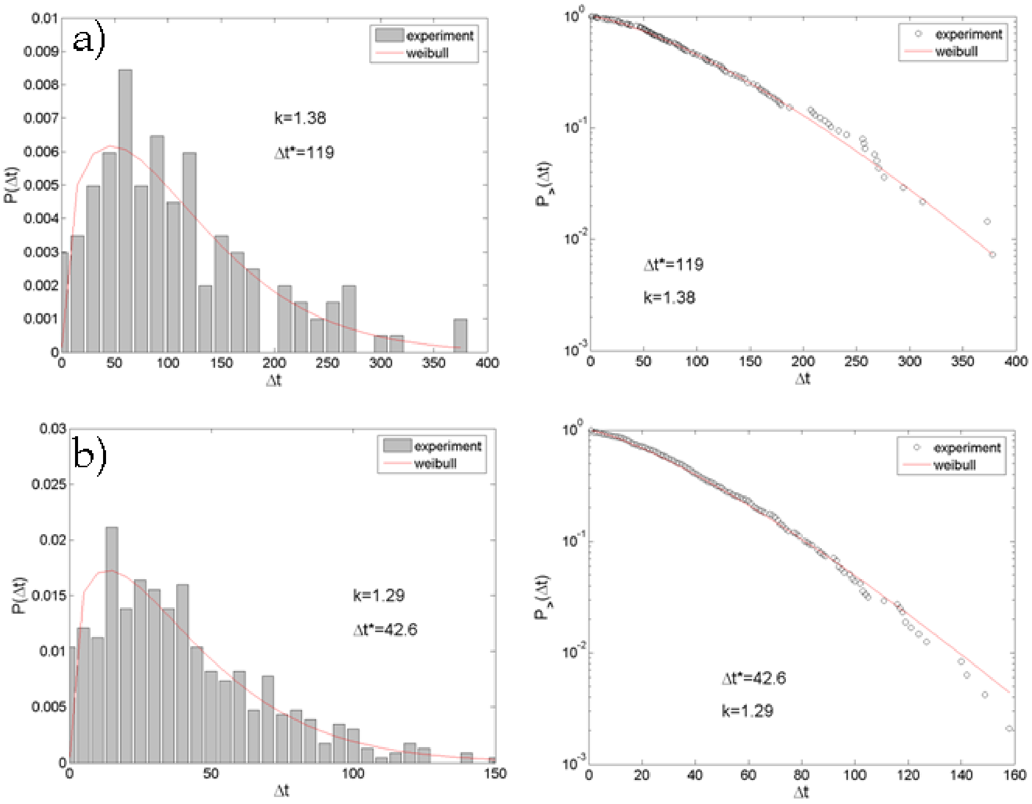

Figure 4.13: Statistical analyses of the interval time of nucleation between two microcracks mother-daughter. Left column: Probability distribution function, right column: Cumulative distribution function. a) $v = 250m/s$ and b) $v = 450m/s$. The time is expressed without units since no time unit are considered in the reconstruction.

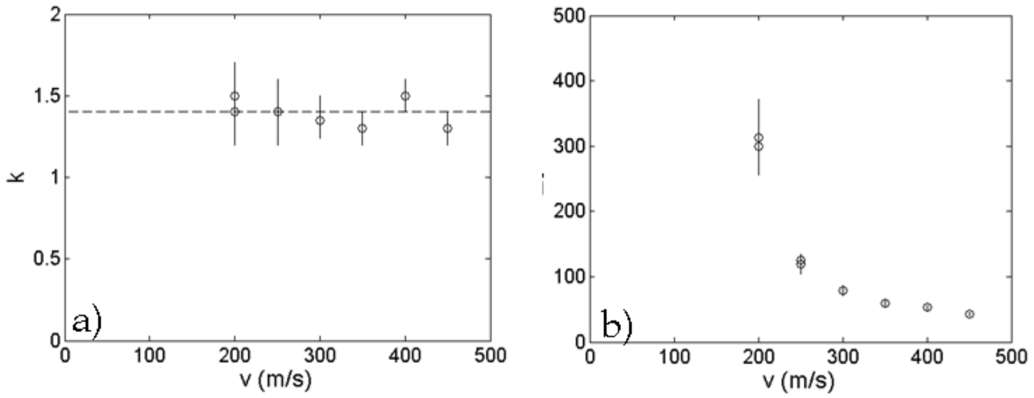

Figure 4.14: Statistic parameters k and τ that characterize the Weibull distribution of the time interval between a primary microcrack and its daughter. Evolution as a function of the crack velocity, v. The time is expressed without units since time is unitless in the reconstruction. The error bars correspond to a 95% confidence interval.

4.2.3 Distances between the nucleation center of a microcrack and its daughter

Finally, to complete the analysis, we now look at the statistics of the position of the nucleation center of a given microcrack with respect to that of its mother. Let us call Δx and Δz the distance between the two along the direction of crack propagation and along the mean crack front, respectively (Fig. 4.15).

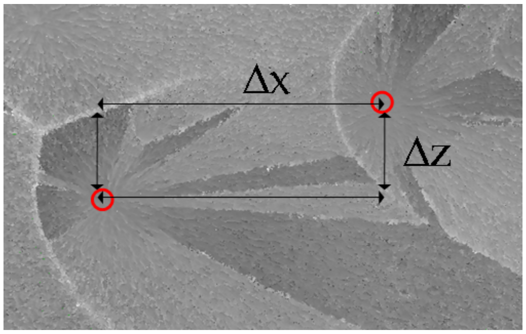

Figure 4.15: Definition of the quantities Δx and Δz that characterize the distance between the nucleation center of a primary microcrack and its daughter.

Figure 4.16 shows the probability density function and the cumulative distribution of both Δx and Δz for two velocities (250 m/s in the left column and 450 m/s in the

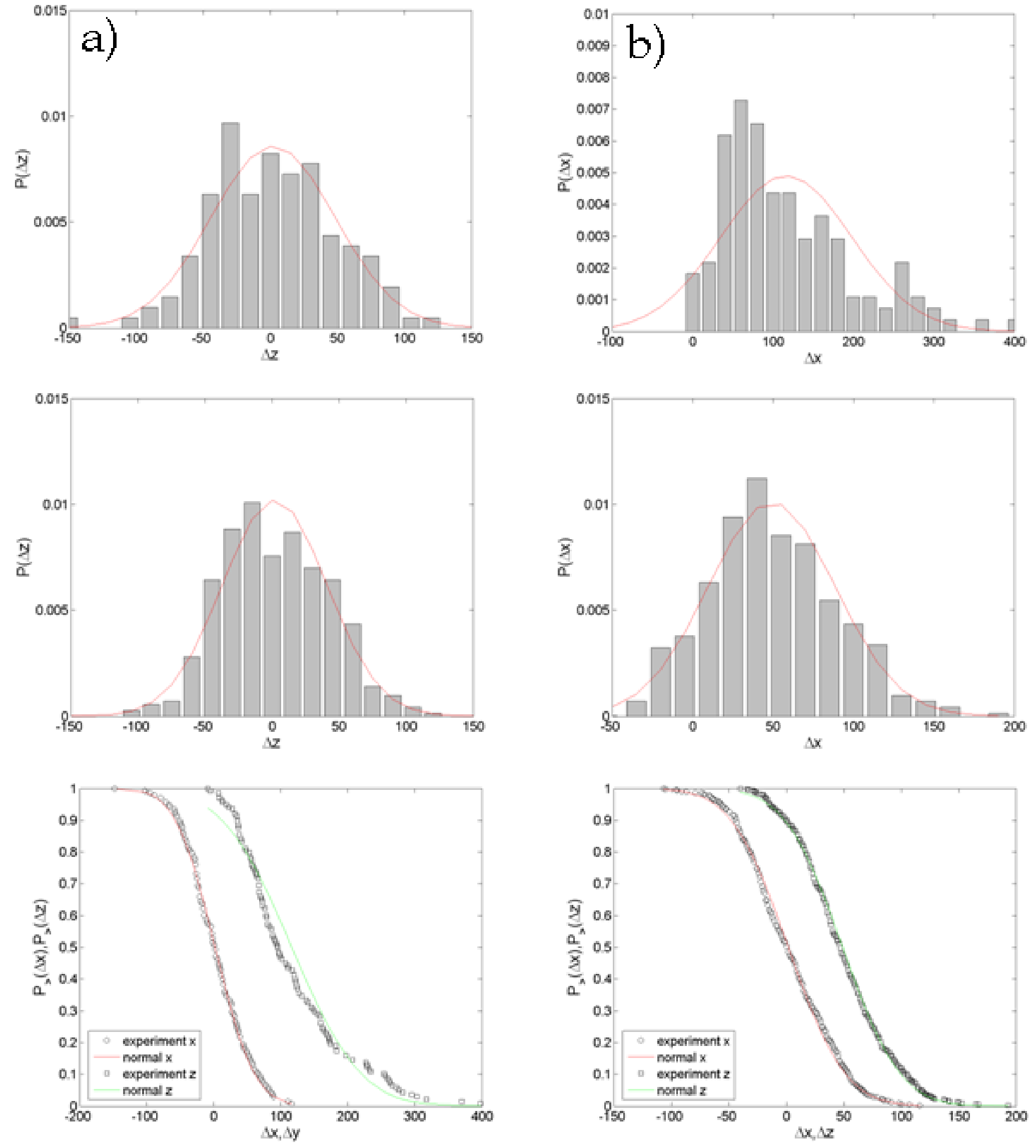

Figure 4.16: Statistical analysis of the distance between the nucleation sites of a primary microcrack and its daughter. Top: probability distribution function in Δx. Middle: probability distribution function in Δz. Bottom: cumulative distribution function for both directions Δx and Δz. a) $v = 250$ m/s and b) $v = 450$ m/s.

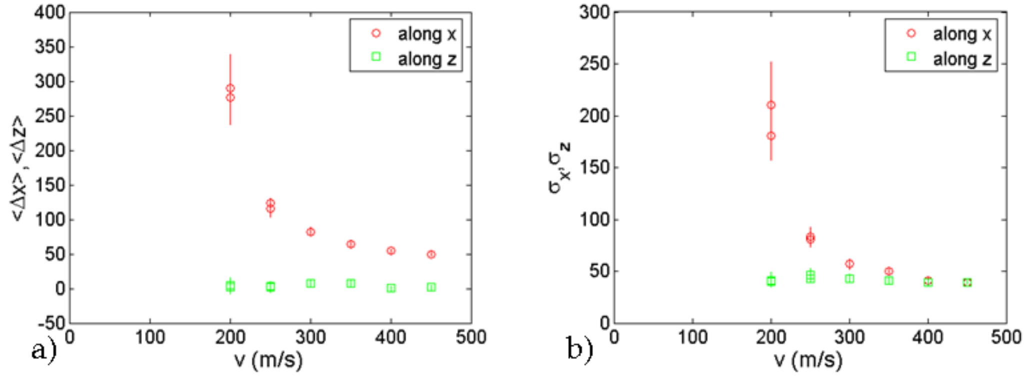

Figure 4.17: Evolution of statistical parameters that characterize the Gaussian distribution of the distances Δx and Δz between a primary microcrack and its daughter. (a) mean values μ_x, μ_z as a function of v. (b) standard deviations σ_x, σ_z as a function of v. The errorbars correspond to a 95% confident interval.

right column). These distributions fit fairly well a Gaussian distribution:

$$P(\Delta x) = \frac{1}{\sqrt{2\pi\sigma_x^2}} \exp\left[\frac{-(\Delta x - \mu_x)^2}{2\sigma_x^2}\right], \quad P(\Delta z) = \frac{1}{\sqrt{2\pi\sigma_z^2}} \exp\left[\frac{-(\Delta z - \mu_z)^2}{2\sigma_x^2}\right] \tag{4.4}$$

To be more precise, the Gaussian distribution fits fairly well the data for Δz over the whole range of velocity, but departs from the Gaussian is observed for Δx as the velocity gets closer to v_a. The mean values μ_x, μ_z and the standard deviations σ_x, σ_z are plotted as a function of the velocity in Fig. 4.17. Along the z direction, the mean value remains null over the whole velocity range, as expected from symmetry. The standard deviation does not depend on v: $\sigma_z \simeq 40\ \mu$m. Along the direction x of crack propagation, both mean value, μ_x, and standard deviation, σ_x, diverge as the velocity decreases down to the threshold value v_a.

4.2.4 Discussion

It is interesting to compare the distribution of silent times and distances between the nucleation of a mother microcrack to a daughter to the ones observed in: (i) earthquakes (see e.g. [95, 96, 78] for reviews); (ii) the acoustic emission which accompanies the failure of brittle heterogeneous materials (see e.g. [97, 78] for reviews); and

(iii) the crackling dynamics observed in the numerical simulations of lattice models so-called Random Fuse Models which sketch a heterogeneous material as a network of fuses with randomly distributed breakdown (see e.g. [98] for a review). In all cases, a power-law distribution is observed for the waiting time and the distances between epicenters. This is very different from what is observed here, for dynamically induced damage spreading in a nominally brittle material: (i) a Weibull distribution for the waiting time and (ii) Gaussian distributions for distances between nucleation centers. This can be understood as follows: In the "common" situations met in earthquakes, random fuse models and fracture experiments with acoustic emission, the power-law distribution is thought to be selected because of the competition between the local disorder in the material microstructure and the long range coupling because of the elastic load redistribution after local breakdown. In the dynamic situations met in our experiments, the front propagates at velocities that stop to be negligible with respect to sound speed and the time delay induced by the dynamic stress transfer limits the range of the elastic coupling after each nucleation event.

4.3 Analyses of the reconstruction: back to the macroscopic scale!

It is now time to use this reconstruction at the microscopic scale to investigate how macroscopic quantities (namely the process zone size and the effective crack length) relate to microcracking at the microscopic scale.

4.3.1 Process zone size

The primary plane crack front is observed to become more and more tortuous as the crack velocity increases (Fig. 4.6). The size of the process zone R_c can then be estimated as the typical width σ of the zone where microcracks are observed. Calling $f(z,t)$ the line that limits the zone beyond which no broken material is observed, the process zone size is given by $R_c(t) =< (f(z,t)- < f(z,t) >)^2 >^{1/2}$ where the average $<>$ is restricted to the center of each snapshot to avoid boundary effects. Then, we average $R_c =< R_c > (t)$ in the steady regime (i.e. for times larger than the time where no straight parts can be observed on the front, and smaller than the time where a first microcrack touches the boundary). The mean process zone size as a function of the crack velocity is shown in Fig. 4.18. These results show that the mean of the process zone size increases with the crack velocity up to $v = 350$ m/s where it saturates. It is interesting to note that this value is fairly close to the microbranching onset ($v_b = 317$ m/s). Whether or not it is a concidence remains to be uncovered.

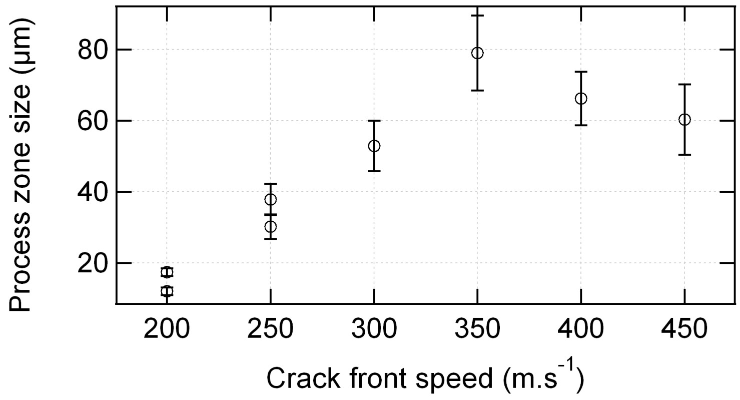

Figure 4.18: Evolution of the process zone size as a function of the crack velocity v.

To estimate the tortuosity of the crack front, we plot in Fig. 4.19a the evolution of the crack front length (normalized by the box thickness), as a function of the normalized time. This normalized length fluctuates with time, than crack velocity is more important. An average value is defined on the steady range. This mean value is found to increase with velocity, as is shown in Fig. 4.19b.

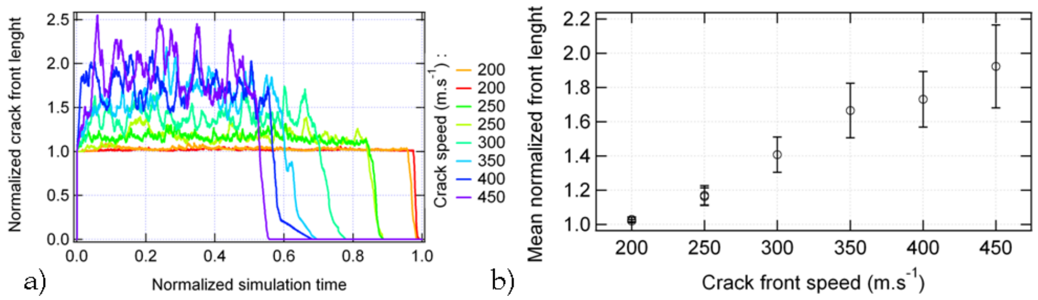

Figure 4.19: a) Time evolution of the normalized crack length for all the velocities. b) Averaged value of the normalized crack length as a function of the crack velocity v. The error bars indicate the standard deviation.

4.3.2 Macroscopic crack velocity vs microscopic front velocity

Finally, it is interesting to look at the dynamics of the main crack front on the microscopic scale. In this respect, figure 4.20 presents the time evolution of two given points of the crack front at two different velocities ($v = 250$ m/s and $v = 450$ m/s). Locally, the front propagation is jerky, with sudden jumps that correspond to the coalescence events with microcracks. These jumps make the crack velocity measured at the continuum scale much larger than the actual velocity of the various fronts at the microscopic scale (set to 1 pixel per time step in the reconstruction).

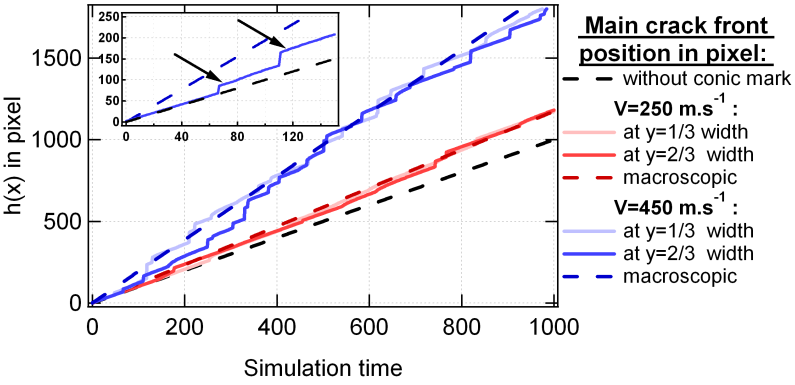

Figure 4.20: Time evolution of two local points of the main crack front as observed in the reconstruction obtained for $v = 250$ m/s and $v = 450$ m/s.

In figure 4.21a, the mean position of the primary crack front is plotted as a function of time for the various velocities. The higher the mean crack velocity, the higher the microcrack density and the higher the number of coalescence events. As a consequence, for a constant microscale front velocity ($v_{wcm} = 1$ pixel/timestep), the macroscopic crack velocity v_{cm} is increased with the v measured experimentally. The ratio between v_{cm} and v_{wcm} is plotted in figure 4.21a.

From the knowledge of this ratio, we can deduce the microscale velocity of the various fronts (primary crack and microcracks nucleated ahead) yielding the fracture surfaces presented in figure 4.5. These values are presented in Table 4.1. It is interesting to note that the resulting velocities are gathering around a value close to 220 m/s, i.e. close to the value $v'_a \simeq 200$ m/s estimated in the preceding chapter (see section 3.3).

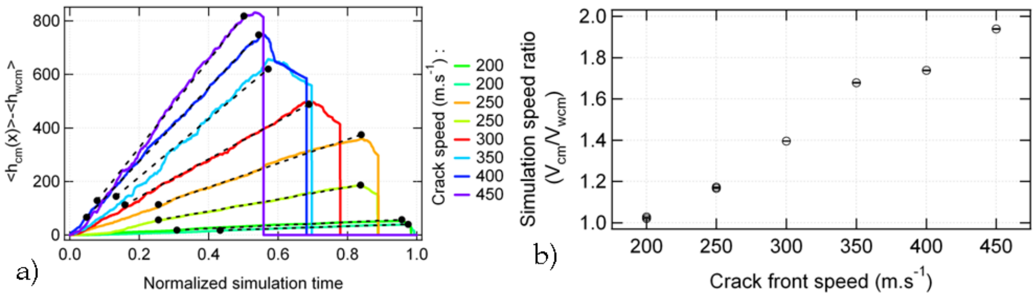

Figure 4.21: a) Time evolution of mean position of the crack front as a function of time for the various velocity, ranging from $v = 200$ m/s to $v = 450$ m/s. b) Ratio between the macroscale velocity V_{cm} and the microscale one V_{wcm}.

Macroscopic crack velocity	200 m/s	250 m/s	300 m/s	350 m/s	400 m/s	450 m/s
Velocity ratio	1.02	1.16	1.41	1.66	1.73	1.92
Microscopic front velocity	196 m/s	215 m/s	213 m/s	213 m/s	231 m/s	234 m/s

Table 4.1: Macroscopic crack velocity and microscopic front velocity.

4.4 Conclusion

In this chapter, we have investigated the dynamics of damage spreading at the microscopic scale. Indeed, a geometrical reconstruction allows us to compute the dynamics of the main crack and the nucleation and growth of microcracks , the remnants of which are conic marks on the post-mortem fracture surfaces. The resolution of the reconstructed dynamics is set by that of the experimental image, ~ 1 μm.

The microcracking statistics has been characterized. The time delay between a primary microcrack and its daughter is found to be distributed according to a Weibull law. The distance between the nucleation center of a primary microcrack and its daughter follows a Gaussian distribution. It is interesting to note that these distributions for damage spreading ahead of a dynamically growing crack are different from what was observed in slow fracture regimes as e.g. in earthquakes. In this latter case, power-laws are observed. The origin of these difference is believed to be in the dynamic stress transfers occurring in the dynamic case.

Finally, these microscale reconstructions has allowed us to compare the effective crack velocity, observed at the macroscopic scale, to the microscale velocity of the microcrack fronts. We showed that the microscale front velocity saturates at a value close to 230 m/s, in agreement to what was suggested in the scenario presented at the end of the preceding chapter.

Conclusion

This experimental study has focused on dynamic crack propagation in brittle materials. Its goal was to shed light on the dissipation mechanisms during dynamic crack growth.

In this respect, we have designed an efficient experimental setup that grows dynamic cracks in PMMA (the archetype of brittle material) in a stable manner. We have adapted the potential drop method to measure precisely the instantaneous crack velocity. Subsequently finite element calculations were steady to estimate the mechanical state in the vicinity of the propagating crack.

With these data, we were able to estimate the fracture energy, and its evolution as a function of crack velocity. This curve reveals an abrupt increase at a well-defined critical velocity, $v_a \simeq 0.19 \times c_R$. This transition was shown to coincide with the appearance of conics patterns on the post-mortem fracture surfaces, which are the signature of damage spreading through the nucleation and growth of microcracks occurring ahead of the crack front. These experimental results allowed us to propose a simple scenario to explain the form taken by the fracture energy below and above v_a, thus capturing the variation of the fracture energy with respect to the crack velocity. Together with the equation of motion, we can reproduce the experimental velocity profiles. This also provides an explanation of the maximum velocity observed in PMMA, and the ”mist” texture of fracture surfaces observed at high velocity. It is interesting to note also that in this scenario, the crack velocity observed at the macroscale is larger than the growth velocities of the microcracks observed at the microscale.

In the second step, we investigated the damage mechanisms at the microscale from the post-mortem fracture surfaces. Using a model proposed initially by Smekal [61] and later developed by Yang and Ravi-Chandar [66], we were able to reconstruct the propagation dynamics of the main crack front and that of the microcrack nucleation and growth. From the reconstructions we study the event statistics as a function of the fracture velocity. It is shown in particular that this statistics is very different from what is observed in slow failure situations, as in earthquakes for instance. These reconstructions have allowed us to compare the effective crack velocity, observed at the macroscopic scale, to the microscale velocity of the microcrack fronts. This analysis allowed to confirm what was conjectured from the macroscopic study and the variation of the fracture energy as a function of velocity below v_a (namely that the microscale velocity saturates at a value close to $0.2c_R$, i.e. much smaller than what is observed at the macroscale).

Now, what comes next? I sincerely think that the next important question to answer concerns the mechanisms that cause the nucleation of these microcracks in PMMA? This question remains debated in the polymer community. It has been proposed that these nucleations are due to preexisting cavities in the material. It has also been proposed that they are the consequence of crazing. To shed light on this question, we have looked at conic focii at atomic scales. Figure 4.22 shows three force atomic microscope images, at various resolutions. In these images, we can clearly see a spherical ball at the center of the conic marks, the size of which is around 200 nm. This is more reminiscent of cavitation processes than from crazing. To understand what is at the origin of these nucleation centers provides an interesting challenge for future studies.

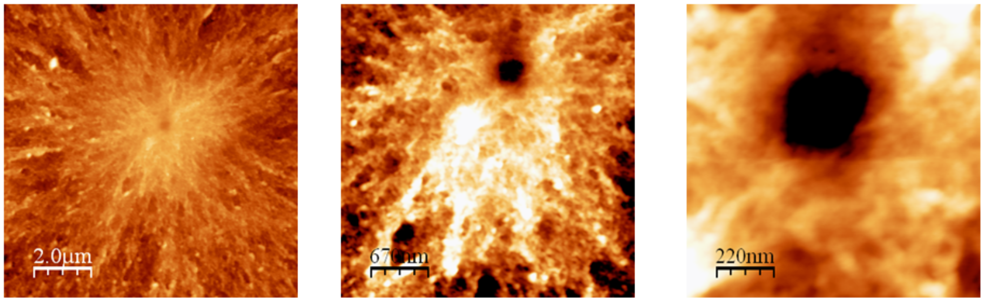

Figure 4.22: Atomic force microscope images showing conic focii a)10 μm^2, b)3.4 μm^2 and a)1.1 μm^2.

Bibliography

[1] K. B. Broberg. *Cracks and Fracture.* Academic Press, 1999.

[2] Inglis. Stresses in a plate due to the presence of cracks and sharp corners. *Trans. Inst. Naval Archit.*, 55:219, 1913.

[3] A. A. Griffith. The phenomena of rupture and flow in solids. *Philosophical Transaction of the Royal Society of London*, A221:163, 1920.

[4] A. A. Griffith and J. Waltamn Jr. The theory of rupture. In C. B. Biezeno and J. M. Burgers, editors, *Proc. First Internat. Congr . Appl. Mech.*, page 55, 1924.

[5] W. Weibull. A statistical theory of the strengh of the materials. *Proc. Roy. Swed. Inst. Eng. Res.*, page 151, 1939.

[6] E. Orowan. Energy criteria of fracture. In *Energy criteria of Fracture*, volume 34, page 157, 1955.

[7] G. R. Irwin. Fracture. In *Handbuch der Physik*, 6, page 551. Berlin: Spinger-Verlag, 1958.

[8] M. Marder and J. Fineberg. How things break. *Physics today*, 49:24–29, 1996.

[9] D. Hull. *Fractography.* Cambridge University Press, 1999.

[10] B. Lawn. *Fracture of brittle solids.* Cambridge University Press, 1993.

[11] D. Francois, A. Pineau, and A. Zaoui. *Comportement mcanique des matriaux, volume II : visco-plasticit, endommagement, mcanique de la rupture, mcanique du contact.* 1993.

[12] L. M. Kandanov. *Introduction to Continium Damage Mechanics.* Martinus Nijhoff Publishers, 1986.

[13] S. Timoshenko and J.N. Goodier. *Theory of elasticity.* Engineering societies monograps, 1951.

[14] E. Dulaney and W. Brace. Velocity behavior of growing crack. *J. Appl. Phys*, 31:2233–2266, 1960.

[15] J. Fineberg and M. Marder. Instability in dynamic fracture. *Phys Rep.*, 313:1–108, 1999.

[16] E. H. Yoffe. The moving griffith crack. *Philosophical Magazine*, 42:739–750, 1951.

[17] K. B. Broberg. On the speed of a brittle crack. *J. Appl. Mech.*, 31:546–547, 1964.

[18] J. W. Craggs. On the propagation of a crack in an elastic-brittle material. *J. Mech. Phys. Solids*, 8:66–75, 1960.

[19] H. Schardin. *Velocity effects in fracture.* Jhon Wiley & Sons, 1959.

[20] A. Stroh. A theory of the fracture metals. *Philos. Mag.*, 6:418–465, 1957.

[21] L. B. Freund. *Dynamic Fracture Mechanics.* Cambridge University Press, 1990.

[22] F. Nilsson. A path-independent integral for transient crack problems. *Int. J. Solids and Structures*, 9:1107–1115, 1973.

[23] J. D. Achenbach and Z. P. Bazant. Elastodynamic near-tip stress and displacement fields for rapid propagating cracks in orthopic media. *J. Appl. Mech.*, 42:183–189, 1975.

[24] A. J. Rosakis, Mason J. J., and G. Ravichandran. The convertion of plastic work to heat around a dynamically propagating crack in metals. *J. Mech. Behaviour Materials*, 4:375–385, 1992.

[25] A. J. Rosakis, C. Liu, and L. B. Freund. A note on the asymptotic stress field of a non-uniformly propagating dynamic crack. *Int. J. Fract.*, 50:R39–R35, 1991.

[26] J. D. Eshelby. The elastic field of a crack extending non-uniformly under general anti-plane loading. *J. of Mech. and Phys. of Solids*, 17:177–199, 1969.

[27] B. V. Kostrov. Unsteady propagation of longitudinal shear crack. *J. Appl. Math. Mech.*, 30:1241–1248, 1966.

[28] E. Sharon and J. Fineberg. Confirming the continuum theory of dynamic brittle fracture for fast cracks. *Nature*, 397:333–335, 1999.

[29] R. V. Goldstein and R. L. Salganik. Brittle fracture of solids with arbitrary cracks. *Int. J. Frac.*, 10:507–523, 1974.

[30] E. Sommer. Formation of fracture lances in glass. *Engineering Fracture Mechanics*, 1:539–546, 1969.

[31] J. F. Boudet, S. Ciliberto, and V. Steinberg. Dynamics of crack propagation in brittle materials. *J. Phys. II France*, 6:1493–15, 1996.

[32] K. Ravi-Chandar. *Dynamic Fracture*. Elsevier Ltd, 2004.

[33] K. Arakawa and K. Takahashi. Relationships between fracture parameters and fracture surface roughness of brittle polymers. *Int. J. Frac.*, 48:103–114, 1991.

[34] K. Ravi-Chandar and W. G. Knauss. An experimental investigation into dynamic fracture-iii on steady-state crack propagation and crack branching. *International Journal of Fracture*, 25:141–154, 1984.

[35] T.L. Paxon and R.A. Lucas. An experimental investigation of the velocity characteristics of a fixed boundary fracture model. In *International Conference on Dynamic Crack Propagation*, 1973.

[36] D.J. Andrews. Stress waves and fracture surfaces. *J. Appl. Phys.*, 30:740–743, 1959.

[37] J. W. Jonhson and D. G. Holloway. On the shape and size of the fracture zones on glass fracture surfaces. *Philos. Mag.*, 14:731–743, 1966.

[38] F. Kerkhof. *Wave fractographic investigations of brittle fracture dynamics*. Noordhoff International Publishing, 1973.

[39] J. J. Mecholsky, J. R. Rice, and S. W. Freiman. *Fractographic Analysis of Ceramics*. Fractography in Failure Analysis ASTM, 1978.

[40] K. Ravi-Chandar and W. G. Knauss. An experimental investigation into dynamic fracture-ii microstructural aspects. *International Journal of Fracture*, 25:65–80, 1984.

[41] K. Ravi-Chandar. *Dynamic fracture of nominally brittle materials*, volume 90. 1998.

[42] K. Ravi-Chandar and W. G. Knauss. Dynamic crack tip stress under stress wave loading - a comparation with theory and experiment. *Int. J. Frac.*, 25:209–222, 1982.

[43] R. V. Mahajan and K. Ravi-Chandar. Exerimental determination of stress intensity factor using caustics and photoelasticity. *Exp. Mech.*, 29:6–11, 1989.

[44] A. J. Rosakis. Analysis of the optical method of caustics for dynamic crack propagation. *Eng. Frac. Mech.*, 13:331–347, 1980.

[45] F. Hild and S. Roux. Measuring stress intensity factor with a camera: Integrated digital image correlation (i-dic). *Comtes Rendus Mecanique*, 334:8–12, 2006.

[46] S. R. McNeil, W. H. Peter, and M.A Sutton. Estimation of stress intensity factor by digital image correlation. *Eng. Frac. Mech.*, 28:101–112, 1987.

[47] H. Wallner. Linenstrukturen an bruchflachen. *Z. Phys.*, 114:368–378, 1939.

[48] J. E. Field. Brittle fracture is an study and application. *Contemporary Physics*, 12:1–31, 1971.

[49] H. C. Richter and F. Kerkhof. Stress wave factography. In *Fractography of glass*. Plenum Press New York, 1994.

[50] D. Bonamy and K. Ravi-Chandar. Dynamic crack response to a localized shear pulse perturbation in brittle amorphous materials: on crack surface roughening. *Int. J. Frac.*, 134:1–22, 2005.

[51] J. Carlsson, L. Dahlberg, and F. Nilsson. Exerimental studies of the unstable phase of crack propagation in metals and polymers. In *Dynamic crack propagation*. Noordhoff International Publishing, Leyden, 1973.

[52] J. Fineberg, S. P. Gross, M. Marder, and H. L. .Swinney. Instability in the propagation of fast cracks. *Phys Rev. B*, pages 5146–5154, 1992.

[53] D. Holland and M. Marder. Ideal brittle fracture of silicon studied with molecular dynamic. *Physical Review Letters*, 80:746–749, 1998.

[54] S. R. Anthony, J. P. Chub, and J. Congleton. The crack branching velocity. *Philos. Mag.*, 22:1201–1216, 1970.

[55] B. Cotterell. Fracture propagation in organic glasses. *The International Journal of Fracture Mechanics*, 2:209–217, 1968.

[56] B. Cotterell. Velocity effects in fracture propagation. *Appl. Mater. Res.*, 4:227–232, 1965.

[57] J. F. Boudet and S. Ciliberto. Interaction of sound with fast crack propagation: An equation of motion for the crack tip. *Physica D*, 142:317–345, 2000.

[58] J. Fineberg. *The Dynamics of Rapidly Moving Tensile Cracks in Brittle Amorphous Material to appear in Dynamic Fracture Mechanics*. World Scientific, 2006.

[59] D. Hull. Influence of stress intensity and crack speed on fracture surface topography: mirror to mist transition. *J. Mater. Sci.*, 31:1829–1841, 1997.

[60] D. Hull. Influence of stress intensity and crack speed on fracture surface topography: mirror to mist to macroscopic bifurcation. *J. Mater. Sci.*, 31:4483–4492, 1997.

[61] E. Smekal. Zum bruchvorgang bei sprodem sotffverhalten unter ein- and mehrachsigen beanspruchungen. *Osterreichische Ingenieur Arch.*, 7:49–70, 1953.

[62] V. R. Regel. *J. Tech. Phys.*, 21:287, 1951.

[63] C. D. Beachmen. The interpretation of electron fractographs. Technical report, U. S. Naval Research Laboratory Report 6360, 1966.

[64] G. R. Irwin and J. A. Kies. Fracturing and fracture dynamics. *Weld. J. N. Y. Res. Suppl.*, 31:95, 1952.

[65] J. A. Kies, A. M. Sullivan, and G. R. Irwin. Interpretation of fracture markings. *J. Appl. Phys.*, 21:716–720, 1950.

[66] B. Yang and K. Ravi-Chandar. On the role of the process zone in dynamic fracture. *Journal of the Mechanics and Physics of Solids*, 44:1955–1976, 1996.

[67] S. B. Newman and I. Wolock. Fracture phenomena and molecular weight in polymethylmethacrylate. *J. Appl. Phys.*, 29:59–52, 1957.

[68] F. Zandman. *Etude de la deformation et de la rupture des matieres plastiques.* PhD thesis, Publications Scientifiques et Techniques du Ministere de l'Air, 1953.

[69] J. Leeuwrik. Kinematic features of the brittle fracture phenomenon. *Rheol. Acta*, 2:10–16, 1962.

[70] D. G. Holloway. The fracture of glass. *Physics Education*, 3:317–322, 1968.

[71] M. Adda-Bedia, R. Arias, M. Ben-Amar, and F. Lund. Dynamic instability of brittle fracture. *Physical Review Letters*, 82:2314–2317, 1999.

[72] M. Adda-Bedia, R. Arias, M. Ben-Amar, and F. Lund. Generalized griffith criterion for dynamic fracture and the stability of crack motion at high velocities. *Phys. Rev. E.*, 60:2366–2376, 1999.

[73] B. R. Baker. Dynamics stresses created by a moving crack. *J. Appl. Mech.*, 29:449–458, 1962.

[74] J. D. Eshelby. *Inelastic behavior of solids.* McGraw-Hill New York, 1970.

[75] E. Sharon and J. Fineberg. Microbranching instability and the dynamic fracture of brittle materials. *Physical Review B*, 54(10):7128–7139, Sep 1996.

[76] J. F. Boudet and S. Ciliberto. Interaction of sound with fast crack propagation. *Physical Review Letters*, 80:341–344, 1998.

[77] I.G. Scott. *Acoustic emission, non destructive testing monographs and t.* Gordon and Breach, New York, 1991.

[78] D. Bonamy. Intermittency and roughening in the failure of brittle heterogenous materials. In revision.

[79] S. Gross, J. Fineberg, M. Marder, W. D. McCormick, and H. L. Swinney. Acoustic emission from rapidly moving crack. *Physical Review Letters*, 71:3162–3165, 1993.

[80] E. Sharon and J. Fineberg. Universal feautures of the microbranching instability in dynamic fracture. *Philos. Mag.*, 78:243–251, 1998.

[81] E. Sharon, S. Gross, and J. Fineberg. Energy dissipation in dynamic fracture. *Physical Review Letters*, 76(12):2117–2120, Mar 1996.

[82] J. A. Hauch, D. Holland, M. P. Marder, and H. L. Swinney. Dynamic fracture in single crystal silicon. *Phys. Rev. Lett.*, 82:3823–3826, 1999.

[83] D. Bonamy and K. Ravi-Chandar. Interaction of shear waves and propagating cracks. *Physical Review Letters*, 91:235502, 2003.

[84] H. N. Linsbauer and E. K. Tschegg. Fracture energy determination of concrete with cube-shaped specimens. *Zement and Beton*, 31:38–40, 1986.

[85] E. Bruhwiler and F. H. Wittmann. The wedge splitting test: A method for performing stable fracture mechanics tests. *Engineering Fracture Mechanics*, 35:117–125, 1990.

[86] G. V. Guinea and J. Elises, M. Planas. Stress intensity factors for wedge-splitting geometry. *Int. J. Frac.*, 81:113–124, 1996.

[87] J. R. Rice. A path independent integral and the approximate analysis of strain concentration by notches and cracks. *Journal of Applied Mechanics*, 35:379–386, 1968.

[88] A. Bertram and J. F. Kalthoff. Fracture energy of propagating cracks in rock. *Materialprufung*, 45:100–104, 2003.

[89] J. F. Kalthoff, S. Winkler, and J. Beinert. Dynamical stress inetnsity factors for arresting cracks in dbc specimens. *Int. J. Frac.*, 12:317, 1976.

[90] A. J. Rosakis, J. Duffy, and L. B. Freund. The determination of dynamic fracture toughness of aisi 4340 steel by the shadow spot method. *J. Mech. Phys. Solids*, 32:443–16, 1984.

[91] K. Ravi-Chandar and B. Yang. On the role of microcracks in the dynamic fracture of brittle materials. *Journal of Physics and Mechanics of Solids*, 45:535–563, 1997.

[92] K. Matsushige, Y. Sakurada, and K. Takahashi. X-ray microanalysis and acoustic emission studies on the formation mechanism of secondary cracks in pmma. *Journal of Material Science*, 19:1548–1555, 1984.

[93] J. S. Sheng and Y. P. Zhao. *International Journal of Fracture*, 98:L9, 1999.

[94] C. A. Buckley, E. P. LAUTENSCHLACER, and J.L. GILBERT. Deformation processing of pmma into high-strength fibers. *J. Appl. Polym.*, 44:1321–1330, 1992.

[95] T. Utsu. Representation and analysis of the earthquake size distribution: A historical review and some new approaches. *Pure and Applied Geophysics.*, 155:509–535, 1999.

[96] Y. Ben-Zion. Collective behaviour of earthquakes and faults: Continium-discrete transitions, progressive evolutionary changes and different dynamic regimes. *Review of Geophysics*, 46:RG4006, 2008.

[97] S. Deschanel, L. Vanel, N. Godin, G. Vigier, and S. Ciliberto. Experimental study of crackling noise: conditions on power law scaling correlated with fracture precursors. *Journal of Statistical Mechanics: Theory and Experiments*, page P01018, 2009.

[98] M. J Alava, P. K. V. V. Nukala, and S. Zapperi. Statistical models of fracture. *Advances in Physics*, 55:349–476, 2006.

Résumé- La propagation de fissures est le mécanisme fondamental responsable de la rupture catastrophique des matériaux fragiles. Celle-ci est décrite traditionnellement par la Mécanique Linéaire Elastique de la Rupture. Or, si ce cadre théorique apparait performant pour décrire des fissures lentes, il échoue largement à haute vitesse. En particulier, il ne permet pas de rendre compte des vitesses de rupture maximales observées expérimentalement, ni de la rugosité des faciès observée à haute vitesse. Pour explorer ces phénomènes, nous avons mis en place un dispositif expérimental qui permet d'étudier les mécanismes de rupture dans un matériau fragile modèle - nous avons opté pour le Plexiglas - sur une large gamme de vitesse, aux petites échelles d'espace et de temps. Ce dispositif nous a permis de mettre en évidence une nouvelle vitesse critique au delà de laquelle, la propagation de la fissure s'accompagne d'endommagements macroscopiques sous forme de nucléation et de croissance de microfissures en avant du front. Un scénario simple permet de prendre en compte cet endommagement pour quantifier la variation de l'énergie dite de fracture, i.e. l'énergie dissipée par le matériau lorsque la fissure se propage d'un incrément de surface, et expliquer la valeur anormalement basse de la vitesse limite de rupture observée dans les matériaux fragiles. Il explique aussi la nature grenue des faciès de rupture observés. Nous avons par ailleurs pu montrer qu'il était possible, à partir des faciès de rupture, de reconstruire de manière déterministe, à l'échelle du micromètre et de la microseconde la dynamique de propagation du front de fissure et le développement d'endommagement associé.

Mots-clés : rupture dynamique, matériaux fragiles, marques coniques.

Abstract- Crack propagation is the fundamental mechanism responsible for catastrophic breakdown of brittle materials, and is usually described by the Linear Elastic theory of fracture. However, this theoretical framework is only relevant to slow crack propagation and fails dramatically at high velocities. In particular, it accounts neither for the experimentally observed maximal crack velocities, nor for the roughness of the post-mortem fracture surfaces obtained in the high velocity regime. In order to investigate these phenomena, we have designed an experimental setup that allows to study the fracture mechanisms in a model brittle material, namely PMMA, over a wide range of velocities at small space and time scales. This apparatus has enabled us to evidence a new critical velocity beyond which crack propagation is accompanied by macroscopic damage through the nucleation and growth of microcracks ahead of the front. A simple scenario allows to take this damage into account in the so-called fracture energy, i.e. the energy dissipated as the crack propagates over a surface increment, and may succeed to explain the abnormally low limiting crack velocity observed in brittle materials. It explains also the "mist" nature of the resulting post mortem fracture surfaces above a given velocity. Moreover, we have shown that it is possible to reconstruct deterministically the dynamics of the crack front and the associated damage spreading, at the micrometer/microsecond scale, from the patterns observed on the post mortem fracture surfaces.

Keywords : dynamic fracture, brittle materials, conic marks .